# High-accuracy Motion Estimation for MEMS Devices with Capacitive Sensors

by

Yi Chen

A dissertation submitted in partial fulfillment
of the requirements for the degree of
Doctor of Philosophy
(Mechanical Engineering)
in the University of Michigan
2018

Doctoral Committee:

Associate Professor Kenn R.Oldham, Chair
Associate Professor Kira Barton
Professor Khalil Najafi
Associate Professor Chinedum Okwudire

Yi Chen

davidsky@umich.edu

ORCID iD: 0000-0003-1429-0451

© Yi Chen 2018

# Dedication

*Dedicated to my family, for their eternal love.*

## Acknowledgements

I would like to take this opportunity to thank many people.

First and foremost, I would like to express my sincere gratitude to my research adviser and mentor, Professor Kenn Oldham. He has always been supportive, inspiring and willing to provide guidance to students and trust them to make their best judgement. It was truly a pleasure to work with Professor Oldham, and this dissertation and the research work involved would not have been possible without his continuing support and encouragement. I would also like to thank the other members of my doctoral committee for their time and interests in sharing their expertise in this dissertation, which is a significant milestone in my academic endeavor.

During the course my PhD studies, I had the privilege to collaborate with many excellent research fellows in the University of Michigan, and I would like to express my thanks to all of them. In particular I'd like to extend my acknowledgement to Professor Khalil Najafi, Dr. Ethem Erkan Aktakka, Dr. Jong-Kwan Woo, Robert Gordenker and many others for their support in the work related MEMS IMU calibration. I would also like to thank Professor Wang, Dr. Xiyu Duan, Dr. Haijun Li, Miki Lee and Dr. Zhen Qiu for their help and support in work related to electrostatic micro-scanners.

I would also like to thank my current and former labmates and colleagues, including Dr. Jongsoo Choi, Dr. Kendall Teichert, Dr. Jinhong Qu, Lu Wang and Mayur Birla for imparting their knowledge and expertise on many insightful discussions. I would also like to thank my roommate and best friend Zhen Wu for his encouragement and support in both life and scientific research.

Finally, I also would like to thank my parents, my younger brother and sister for their encouragement and support during the years of this PhD studies. Most importantly, I would like to thank my loving and supportive fiancée Ye Wang, for her love, patience and encouragement.

## Table of Contents


Dedication ii

Acknowledgements iii

List of Tables ix

List of Figures x

Abstract xv

Chapter 1 Introduction 1

1.1 Background and motivation 1

1.2 Dissertation outline 5

Chapter 2 Capacitive Sensing for Position Measurement and Extended Kalman Filter 6

2.1 Electrode configurations 6

2.2 Sensing circuitry for position measurement 7

2.3 Extended Kalman filter for nonlinear processes estimation 10

Chapter 3 Motion Estimation of Micro-stage for in-situ MEMS Gyroscope Calibration 14

3.1 Chapter overview 14

3.2 Background and motivation 15

3.3 Description of micro-stage based calibration 19

3.3.1 Gyroscope model and scale factor calibration 19

3.3.2 Micro-stage based calibration 22

3.3.3 Piezoelectric actuation stage 23

3.3.4 On-chip capacitive sensor 23

3.4 Motion estimation 26
3.4.1 Overview of motion estimator 26
3.4.2 Model of PE stage 27
3.4.3 Model of capacitive sensor 29
3.4.4 Integration with EKF 32
3.5 Experiments and parameter identification 35
3.5.1 Overview of methods 35
3.5.2 Description of setup 36
3.5.3 Description of experiments 38
3.5.4 Parameter identification and post-processing 41
3.6 Results and discussion 44
3.6.1 Evaluation of off-axis signal rejection by capacitance sensor 44
3.6.2 Validation of motion estimation 46
3.6.3 Calibration of MEMS IMU 47
3.6.4 Benchmarks and source of error 50
3.7 Chapter Summary 52
Chapter 4 Threshold Sensing with Micro-scanner 54
4.1 Chapter overview 54
4.2 Background and Motivation 55
4.2.1 Impact of temperature on capacitive sensing and prior studies 55
4.2.2 Electrostatic micro-scanner and threshold sensing 56
4.2.3 Challenges 60
4.3 System modelling 61
4.3.1 Process and sensor model 61
4.3.2 Extended Kalman filter with threshold sensing 62
4.4 Experiments and model identification 64
4.4.1 Experimental set-up and methods 64
4.4.2 Identification of process and sensor models 66

4.5 Parametric study of factors impacting threshold detection 68
4.5.1 Sampling rate effects 68
4.5.2 Sensor map effects 69
4.6 Experimental results and discussion 71
4.6.1 Effect of DOG filter on threshold detection 71
4.6.2 Effect of threshold sensing on EKF 73
4.7 Chapter summary 76
Chapter 5 Motion Estimation with Shared Electrodes for Driving and Sensing 78
5.1 Chapter overview 78
5.2 Background and motivation 79
5.3 Methods 82
5.3.1 Target accuracy of phase shift estimation 82
5.3.2 System dynamics and process model 83
5.3.3 Sensing principle and measurement model 84
5.3.4 EKF and UKF description 90
5.4 Experiments 93
5.4.1 Description of set-up 93
5.4.2 Experimental procedures 95
5.4.3 Post-process 96
5.5 Results and discussion 96
5.5.1 Actuator model identification 96
5.5.2 Sensor model identification 97
5.5.3 Estimators performance comparison 98
5.6 Chapter summary 101
Chapter 6 Concluding Remarks 103
6.1 Summary 103
6.2 Research contributions 106

6.3 Recommendations for future works 106
6.3.1 Non-orthogonality calibration 106
6.3.2 Threshold sensing without complete power cut-off 107
6.3.3 Multi-axis motion estimation with shared electrodes 107
6.3.4 Optimization for on-line estimation 108
Appendix 109
Bibliography 111

## List of Tables

Table 3.1. Specifications of the InvenSense MPU-6500 gyroscope [53] .................................... 37

Table 3.2. Summary of experiments and operational settings ..................................................... 41

Table 3.3. Identified parameters of model of PE stage and capacitive sensor at room temperature ...................................................................................................................................... 43

Table 3.4. Off-axis signal rejection ratio, $R_{off}$ with respect to off-axis motion ratio .................... 45

Table 3.5. Validated RMSE, average scale factor and bias of $\boldsymbol{\omega EST}$ of stage at room temperature ...................................................................................................................................... 47

Table 3.6 Scale factors and biases measured by LDV and stage with two temperature settings . 49

Table 3.7 Comparison of representative reported in-situ calibration results of MEMS gyroscope scale factor ........................................................................................................................ 50

Table 4.1 Algorithm, EKF with Hybrid Sensing Scheme ........................................................... 64

Table 4.2 Baseline setting for parametric Study ......................................................................... 67

Table 4.3 Summary of RMSE of estimated tilting angle ............................................................ 75

Table 5.1 Experimental settings for electrostatic micro-scanner ................................................. 94

Table 5.2 Identified parameters of actuator model, sensor model, EKF and UKF ....................... 97

Table 5.3 RMSE of estimated phase shift and amplitude by implemented estimators .............. 101

Table 6.1 Summary of pros and cons for discussed methods associated with capacitive sensors ...................................................................................................................................... 105

Table A.1. Upper and lower limits of integration for each sensing capacitor ........................... 109

Table A.2 Dimension of capacitive sensors with rotational parallel-plate configuration........... 110

## List of Figures

Fig. 2.1. Commonly used configurations for capacitive sensing: (a) Varying gap; (b) Varying overlapped area. ........ 6

Fig. 2.2. Two AMDM circuits for measurement of capacitance (a) sensing circuit to measure $Cs$ with a single-diode demodulator. (b) sensing circuit to measure $Cs$ with synchronous demodulator. ........ 8

Fig. 2.3. A schematic of the DC sensing circuit for the capacitance rate of change measurement. A DC voltage source, a transimpedance amplifier and a feedback resistor are used to convert the sensing current generated by the variable capacitance into measurable voltage output. ........ 9

Fig. 3.1. Illustration of micro-stage and MEMS IMU (left) and flowchart of micro-stage based calibration method (right). ........ 22

Fig. 3.2. A schematic of micro-stage with integrated 6-axis MEMS IMU, the stage includes a piezoelectric actuation stage with 6 DOF motion generation capability and a capacitive sensing stage for measuring $X$ and $Y$ tilting motion. The schematic is to illustrate the major internal configurations of micro-stage and the dimensions are not scaled to the true dimensions of the device. ........ 23

Fig. 3.3. Integrated micro-stage and MEMS IMU (left, cross-sectional side view) and design of capacitive sensor for $X$ and $Y$ tilting motion (right, top view). ........ 24

Fig. 3.4. A schematic of the sensing circuit for the capacitive sensors; a transimpedance amplifier is used to convert the current generated by the variable capacitance into measurable voltage. ... 25

Fig. 3.5. Overview of the micro-stage motion estimator; the extended Kalman filter is used to integrate the PE stage model and capacitive sensor model to compute *a posteriori* state estimates of tilting motion with the measurement of the applied driving voltage and capacitive sensor signal. ........ 27

Fig. 3.6. Illustration of vertical translation mode (1st natural frequency) and single axis tilting mode (2nd natural frequency) of PE stage ........................................................................ 28

Fig. 3.7. A depict of a capacitor formed by a pair of silicon rotor and stator with existence of rotations about both $\boldsymbol{X}$ (off-axis rotation) and $\boldsymbol{Y}$ (main-axis rotation) axes. The capacitance as a function of $\boldsymbol{\theta X}$ and $\boldsymbol{\theta Y}$ (positive to be clockwise with axes pointing away from observer) is derived based on the geometric relation between the rotor and stator. ........................................ 30

Fig. 3.8. Detailed EKF routine for motion estimation. The matrix of observation is updated with *a priori* estimate of angular position, at each step of estimation. ................................................ 33

Fig. 3.9. Block diagram of components involved in parameter identification (left) and the performance evaluation during IMU calibration (right). ........................................................... 35

Fig. 3.10. A photo (left) of miro-stage (9 × 9 mm) with a 6-axis InvenSense MPU-6500 MEMS IMU (3 × 3 × 0.9 mm) as payload and a schematic (right) of experimental set-up. A LDV is used to measure the tilting motion for parameter identification and performance evaluation of motion estimator. ........................................................................................................ 36

Fig. 3.11. Nyquist curve fit and frequency response of single axis tilting mode......................... 42

Fig. 3.12. Due to the nonlinear relation between $\boldsymbol{C}$ and $\boldsymbol{\theta}$, the sensing signal output by the capacitive sensor model shows that the crest-to-trough distance $\boldsymbol{\lambda}$ changes as $\boldsymbol{Dn}$ changes, such a feature is extracted and used to identify optimal $\boldsymbol{Dn}$.The amplitude of the signals are normalized (- 0.5 to 0.5) with respect to their own amplitude for comparison purpose................................ 43

Fig. 3.13. Identified capacitance profiles for two representative channels from both single and dual axis capacitive sensor models (left), and two simulated time domain signals from the two sensor models (for main-axis tilting motion) respectively (right). The simulation assumes 10 % of off-axis motion for demonstration purpose. ........................................................................ 45

Fig. 3.14. Comparison of angular velocities, $\boldsymbol{\omega}$, measured by LDV (black) and (red) by stage in the testing data set, the waveforms are averaged into one period for noise reduction and demonstration purpose. ........................................................................................................ 47

Fig. 3.15. peak-to-peak $\boldsymbol{\omega IMU}$ vs. $\boldsymbol{\omega REF}$, $\boldsymbol{\omega_REF}$ (measured by LDV and stage respectively) Scale factor of MEMS gyroscope under two temperature settings are computed by least square method and then compared. .......... 48

Fig. 3.16 Estimated standard deviation of scale factor error (in ppm) as a function of sensor noise variance, based on EKF error covariance and Monte Carlo simulation of noise influence on parameter identification accuracy. .......... 51

Fig. 4.1. (a) Scanning electron microscope image of a parametrically-resonant micro-scanner tested in this study. (a) Illustration of comb-finger electrodes used as actuators and capacitive sensors. (b) Zoomed in image of a representative comb-finger structure. .......... 57

Fig. 4.2. An illustration of threshold angle crossing and mechanism of threshold angle sensing and detection. (a) Configurations of comb-finger (1), (2) and (3) correspond to before, at, and after threshold angle crossing. (b) Sensing capacitance vs. tilting angle $\boldsymbol{\theta}$. (c) Tilting angle vs. time. (d) Noisy sensing signal vs. time; the crossing event generates rapid change of signal around (2). (e) Comparison of filtered signal by a derivative operator and a DOG operator. DOG operator is effective in detecting the timing of rapid signal change. .......... 59

Fig. 4.3. Schematic depiction of extended Kalman filter synthesizing capacitive sensing and threshold angle measurement. .......... 63

Fig. 4.4. Experimental set-up: (a) Schematic of major experimental modules and signal flow. (b) Top view of set-up and illustration of geometric relationship between the laser source, MEMS scanner and PSD. (c) Schematic sensing and driving circuitry for the MEMS scanner. .......... 65

Fig. 4.5. (a) Experimentally measured free oscillations vs. simulated decay curve of free oscillations with identified natural frequency and damping ratio of the MEMS scanner. (b) Experimentally identified sensing capacitance with respect to tilting angle. .......... 67

Fig. 4.6. (a) Variance of detection error in threshold angle vs. sampling frequency. (b) Variance of detection error in threshold angle vs. maximum sensor gain slope. .......... 69

Fig. 4.7. Sweep of maximum sensor gain slope. (a) Sensing capacitance becomes sharper around threshold angle as $\boldsymbol{N\theta}$ increase. (b) Sensor gain slope becomes steeper around threshold angle as $\boldsymbol{N\theta}$ increases. .......... 70

Fig. 4.8. Comparison between the sampled error of threshold angle detections and normal distribution with corresponding mean and variance. .................................................................. 72

Fig. 4.9. Distribution of detection errors in threshold angle from experimental measurements at different signal-to-noise ratios can be well modeled by normal distributions. ............................ 72

Fig. 4.10. A representative experimental measurement and estimation result in time domain. (a) Four snapshots of threshold angle crossing detection improving tilting angle estimation. (b) Overall trajectories of tilting angle measurement and estimations. (c);Overall trajectories of sensing signal and response of DOG filter. (d) Corresponding snapshots of sensing signal, where local maxima of filtered response detects threshold angle crossing. ........................................... 74

Fig. 4.11. Variance of detection error in threshold angle during experiments with respect to the standard deviation of DOG filter. ........................................................................................ 75

Fig. 4.12. Normalized RMSE with different signal-to-noise ratios and various $\boldsymbol{\sigma DOG}$settings. Under noisy condition (low SNR), increasing $\boldsymbol{\sigma DoG}$ effectively increases threshold detection accuracy and therefore increases state estimation accuracy of the EKF. .................................... 76

Fig. 5.1. Dual axis electrostatic micro-scanner studied in this chapter. The electrodes are shared for both driving and sensing purpose. ........................................................................... 83

Fig. 5.2. Schematic of driving and sensing circuit (1), place holder for frequency domain analysis ........................................................................................................................................ 85

Fig. 5.3. Frequency spectra illustration of sensing circuits......................................................... 88

Fig. 5.4. Schematic of experimental set-up. A optical sensing system is used to provide ground truth measurement of the tilting motion.......................................................................... 93

Fig. 5.5. Schematic of optical sensing device. A beam splitter is used to deflect the laser beams from the source and from the MEMS scanner in order to reduce the distortion generated. ......... 95

Fig. 5.6. Measurement of ringdown test and fitted decay curve for actuator model parameter identification ........................................................................................................................ 96

Fig. 5.7. Experimentally identified capacitance profile and modeled capacitance profile. .......... 98

Fig. 5.8. Experimentally measured driving voltage (top), tilting angle measured by optical sensing (EXP) and estimated by EKF, UKF (mid), measured and estimated sensing output by optical sensing, EKF and UKF respectively (bottom). ............ 99

Fig. 5.9. Measured and Estimated tilting angles and phase shift, and RMSE of tilting angle and phase shift. ............ 101

Fig. A.1. Design of capacitive sensor for ***X*** and ***Y*** rotational motion (top view) with key dimensions labels (left); CAD drawing (top view) of all electrodes layout for sensing ***X*** and ***Y*** rotational and translation motions (right) ............ 109

## Abstract

With the development of micro-electro-mechanical system (MEMS) technologies, emerging MEMS applications such as *in-situ* MEMS IMU calibration, medical imaging via endomicroscopy, and feedback control for nano-positioning and laser scanning impose needs for especially accurate measurements of motion using on-chip sensors. Due to their advantages of simple fabrication and integration within system level architectures, capacitive sensors are a primary choice for motion tracking in those applications. However, challenges arise as often the capacitive sensing scheme in those applications is unconventional due to the nature of the application and/or the design and fabrication restrictions imposed, and MEMS sensors are traditionally susceptible to accuracy errors, as from nonlinear sensor behavior, gain and bias drift, feedthrough disturbances, etc. Those challenges prevent traditional sensing and estimation techniques from fulfilling the accuracy requirements of the candidate applications.

The goal of this dissertation is to provide a framework for such MEMS devices to achieve high-accuracy motion estimation, and specifically to focus on innovative sensing and estimation techniques that leverage unconventional capacitive sensing schemes to improve estimation accuracy. Several research studies with this specific aim have been conducted, and the methodologies, results and findings are presented in the context of three applications. The general procedure of the study includes proposing and devising the capacitive sensing scheme, deriving a sensor model based on first principles of capacitor configuration and sensing circuit, analyzing the sensor's characteristics in simulation with tuning of key parameters, conducting

experimental investigations by constructing testbeds and identifying actuation and sensing models, formulating estimation schemes is to include identified actuation dynamics and sensor models, and validating the estimation schemes and evaluating their performance against ground truth measurements. The studies show that the proposed techniques are valid and effective, as the estimation schemes adopted either fulfill the requirements imposed or improve the overall estimation performance. Highlighted results presented in this dissertation include a scale factor calibration accuracy of 286 ppm for a MEMS gyroscope (Chapter 3), an improvement of 15.1% of angular displacement estimation accuracy by adopting a threshold sensing technique for a scanning micro-mirror (Chapter 4), and a phase shift prediction error of 0.39 degree for a electrostatic micro-scanner using shared electrodes for actuation and sensing (Chapter 5).

# Chapter 1
# Introduction

## 1.1 Background and motivation

Accompanying the development of micro-electro-mechanical system (MEMS) technologies in the last few decades, capacitive sensing usage has been translated into a vast array of industrial and consumer electronics applications. The capacitive sensing principle is to form a capacitor by separating two or more electrodes across a dielectric (Fig. 2.1), and the change of capacitance due to the change of relative position of the electrodes [1] [2], dielectric constant [3] or addition of external capacitance can be converted into an electrical signal by various sensing circuits [1] [4]. Typical sensing applications include MEMS accelerometers and gyroscopes [5] [6], displacement and position sensors [1] [7] [8], pressure [9] and force sensors [10] including microphones [11], humidity sensors [3] [12], and proximity [13] and tactile sensors [14] [15]. Compared to other transduction mechanisms at small scales, capacitive sensors in general have advantages of low cost, small size, high sensitivity and low power consumption [1] [16].

Recently, a number of MEMS-based applications with additional actuation and sensing requirements have emerged, such as generation of motion stimulus for inertial sensors or optical beam steering [17] [18] [19] [20]. These applications require highly accurate position and/or velocity measurements and may employ various on-chip sensing technologies for that purpose. Capacitive sensing has been proposed in many of these applications owing to its being comparatively easy to fabricate and easy to integrate within system level architectures [21].

However, due to specifications imposed by these applications and, in some cases, the fabrication techniques used, the design of the capacitive sensors can be different from conventional capacitive sensors and pose unique challenges.

The first challenge is that unconventional configurations of capacitive sensor electrodes result in nonlinear mapping between position and capacitance, which means that the traditional sensing circuit cannot be applied to measure motion directly based on raw sensor output. More specifically, the most commonly used capacitive sensors for position measurement are gap-varying and overlapped-area-varying geometries [1] [2]. In the former configuration the gap between the electrodes is designed to vary, whereas in the latter the overlapped area of electrodes is designed to vary. The latter is typically linear, and the former is nonlinear but usually used over small displacements, such that nonlinearity can be neglected. By applying an AC voltage or current to the electrodes, an electrical signal proportional to the position can be generated and therefore measured [1]. In unconventional configurations examined in this dissertation [17] [22] [23], the motion of interest is often rotational with respect to the electrodes and frequently large in amplitude, such that the rotations affect either the gap between the electrodes or their overlapped area nonlinearly. To be able to establish the relationship between the rotation and the capacitance, nonlinear sensor models incorporating knowledge of capacitance as a function of position, and capacitance into motion information (position and/or velocity) are required. Such models may be derived from first principles of capacitive sensing and corresponding sensing circuits, or empirically.

The second challenge is that for applications with stringent space limitations, no dedicated capacitive sensing module may be permissible on the MEMS device, and meaningful signal needs to be extracted from the same capacitor modules designed to generate electrostatic

forces [24]. Such a configuration increases the magnitude of feedthrough generated by the driving signal into the sensed output and increases the challenge of extracting meaningful feedback signal. Previous studies involving modeling of on-chip capacitive sensors and sensing circuits predominantly employ a dedicated capacitive sensing module separated from any driving module [1] [25]. There are other recent studies using shared electrodes for both driving and sensing, but they either employ conventional capacitive sensor configurations with linear relationships between position and capacitance [26] [27], or lack necessary modeling effort to characterize the amplitude-modulated and demodulation (AMDM) sensing circuit to analyze the principal frequency bands of the signals in presence of nonlinearities [24]. Such analysis is important in understanding the distribution of the frequency bands of the signal and to properly design the sensing circuit, especially in the presence of nonlinear features. The analysis is also helpful to build a sensor model to map the positions of interest and the sensing signal, and to integrate this type of capacitive sensor into a nonlinear motion estimation scheme.

The third challenge, shared among the conventional and the proposed capacitive sensing geometries and other small-scale transducers, is that they are susceptible to gain and bias drift due to environmental perturbations such as temperature change [28]. In this work, some unique features of capacitive sensors in those unconventional capacitive sensing applications are proposed to be utilized to improve estimation accuracy. Primarily, in a configuration where capacitance is not monotonic with respect to displacement, a threshold position measurement can possibly be established and used to improve the estimation accuracy [29] [30] [31] [32]. Such a feature may be desirable in capacitive sensing schemes when it can be designed to be insensitive to environmental perturbations such as temperature, or assembly tolerance due to misalignment [33]. However, extracting such a threshold measurement is non-trivial due to existing noise and

bias and has not been rigorously explored previously. Other applications use other attributes of nonlinearity in capacitance versus position to better identify parameters in sensor and estimation models that may vary over time.

This dissertation aims to present a framework for formulating estimation schemes for MEMS devices with nonlinear actuation capability and capacitive sensors, and to introduce innovative sensing and estimation techniques utilizing the unconventional design of capacitive sensors to achieve high-accuracy motion estimation.

The research objectives include:

1. Derive sensor models for each capacitive sensor application and associated sensing circuitry to understand relationships between motion and sensing signals. Devise effective feedthrough reduction methods based on characterization of the sensor design and the specific application.
2. Develop signal processing techniques to extract threshold position measurements and incorporate them into motion estimation schemes. Analyze the improvement of estimation accuracy with threshold sensing methods used, and study the impact of various factors (sampling rate, noise variance, capacitance profile, etc.) that can possibly affect the performance of threshold sensing.
3. Formulate motion estimation schemes incorporating nonlinear process and sensing models. Identify model parameters, validate the analysis and quantify the estimation performance in the context of the use case by constructing testbeds and performing experimental investigations for the studied MEMS devices.

## 1.2 **Dissertation outline**

The dissertation is organized into 6 chapters in total, with the remaining chapters organized as follows:

In Chapter 2, a more detailed introduction of capacitive sensors and circuits for position sensing is given, and the standard extended Kalman filters (EKF) for nonlinear process estimation is also described.

In Chapter 3, a capacitive sensor design used in a MEMS micro-stage for *in-situ* MEMS IMU calibration is presented. An EKF based motion estimator incorporating a nonlinear sensor model is derived and evaluated, and a feedthrough reduction method based on repetitive measurement is proposed and implemented.

In Chapter 4, a threshold position sensing principle using non-monotonic capacitance profile is introduced. A signal processing technique to reliably and efficiently detect threshold position signal is introduced and is implemented in an EKF based motion estimator with simulation and experiments.

In Chapter 5, a motion estimator for a micro-scanner using shared electrodes for driving and sensing is presented. A nonlinear sensor model incorporating capacitance profile and an AMDM circuit is derived and identified. Both EKF and UKF estimators are implemented and experimentally investigated.

In Chapter 6, a summary of the dissertation is provided. The major research contributions are highlighted, and recommendations for future works are provided.

# Chapter 2
# Capacitive Sensing for Position Measurement and Extended Kalman Filter

## 2.1 Electrode configurations

Most capacitive sensors rely on a change in the geometric relationship between two electrodes to measure displacement. The two most common approaches are to vary the electrode gap or vary their overlapped area [5]. Capacitance, *C*, is given by

$$C = \frac{\epsilon_0 \epsilon_r A}{D} \tag{1}$$

where $\varepsilon_r$ is the relative static permittivity (1 for air), $\varepsilon_0$ is the dielectric constant ($8.8542 \times 10\text{-}12$ F $m^{-1}$), $A$ is the overlap area of electrodes and $D$ is the distance between the electrodes. As illustrated in Fig. 2.1, either the change of $D$ (Fig. 2.1 (a)) or change of overlapped area $A$ (Fig. 2.1 (b)) between the electrodes will cause a change of capacitance. The change of capacitance can then be converted into a measurable electrical signal using various sensing circuits [34].

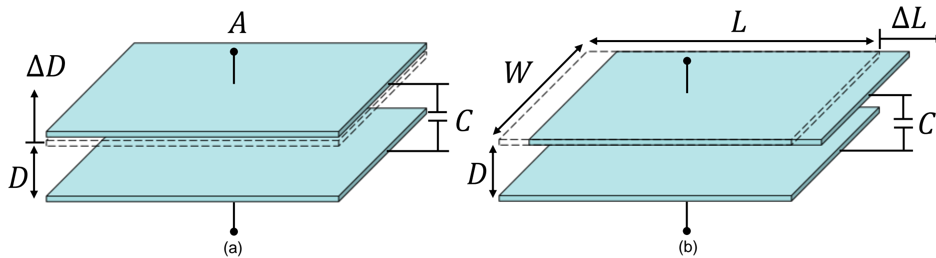


**Fig. 2.1. Commonly used configurations for capacitive sensing: (a) Varying gap; (b) Varying overlapped area.**

In general, applications that make use of gap variation provide greater sensitivity at the cost of nonlinearity and a limited range of measurement. On the other hand, configurations based

on change in area typically provide less sensitivity but more linear behavior, and can be designed to provide a unique feature of a maximal capacitance when electrodes reach their position with maximum overlapped area, a detailed examination of such a mechanism being studied in Chapter 4.

## 2.2 **Sensing circuitry for position measurement**

The function of sensing circuitry for a capacitive sensor is to convert the capacitance into an output signal. From a modeling perspective, the capacitor maps the position to be measured into a capacitance, and the sensing circuit (when at steady state output), establishes a mapping between the capacitance and an output signal.

There are several types of sensing circuits for different capacitive sensing applications [1] [2] [5] [34]. Within the scope of this dissertation, two will be extensively applied and are therefore discussed here.

The first type of sensing circuit is most commonly used in measuring the capacitance using an applied AC voltage [1]. By applying an AC voltage, $V_{ac}$ to a varying area type capacitor, the resulting sensing current $I_s$ can be characterized as

$$I_s = j\omega_{ac,V} V_{ac} C_s(x) \tag{2}$$

where $\omega_{ac,V}$ is the frequency of $V_{ac}$. Notice $I_s$ is proportional to capacitance and thus to displacement, $x$, for a varying area configuration. For a varying gap configuration, if an AC current is applied, one can obtain a sensing voltage $V_s$ as

$$V_s = \frac{I_{ac}}{j\omega_{ac,I} C_s(x)} \tag{3}$$

where $\omega_{ac,I}$ is the frequency of $I_{ac}$, and $V_s$ is inversely proportional to $C_s(x)$ and therefore is linear to $x$.

Since both output sensing signals contain frequency content related to the AC source signal (as a carrier signal), a demodulation technique needs to be applied to separate the motion signal carried by $C(x)$ and the carrier signal in the frequency domain. Fig. 2.2 shows two circuit realizations using amplitude modulation and demodulation (AMDM) principles.

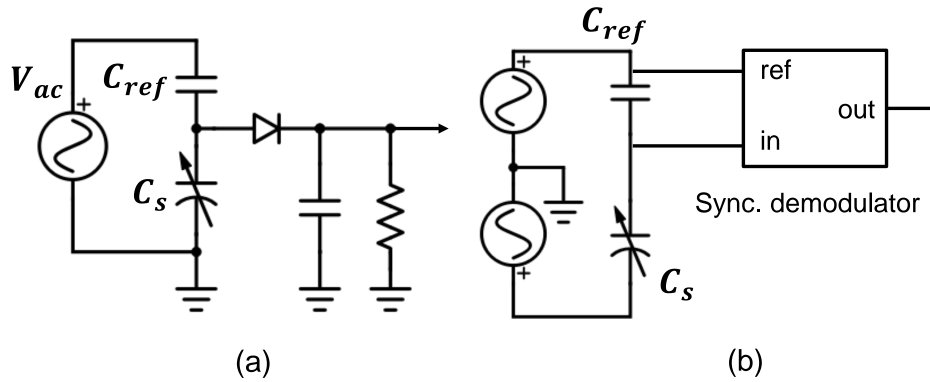


**Fig. 2.2. Two AMDM circuits for measurement of capacitance (a) sensing circuit to measure $C_s$ with a single-diode demodulator. (b) sensing circuit to measure $C_s$ with synchronous demodulator.**

Fig. 2.2(a) shows use of a single diode to form an envelope detector to capture the slow frequency content due to $C(x)$, and (b) shows a synchronous demodulator that uses the carrier signal to perform demodulation. More detailed and exemplary realizations can be found in [34] [25] [35]. It should be noted that although the AMDM circuits provide direct measurement of capacitance, and have additional benefits for filtering noise and disturbances, they add complexity and introduce delay due to the dynamics of amplifiers and filters used for frequency separation.

The second type of circuit is a DC sensing circuit to measure the rate of change of capacitance, as shown in Fig. 2.3.

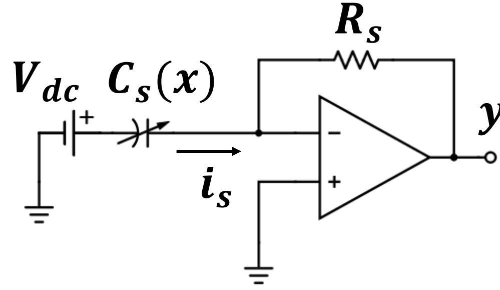


**Fig. 2.3. A schematic of the DC sensing circuit for the capacitance rate of change measurement. A DC voltage source, a transimpedance amplifier and a feedback resistor are used to convert the sensing current generated by the variable capacitance into measurable voltage output.**

A DC sensing circuit consists of a DC voltage source, a transimpedance amplifier and a feedback resistor. The DC voltage source applies a constant voltage $V_{dc}$ between one side of the variable capacitor, $C_s(x)$ and the common node of the capacitor and resistor. A sensing current $i_s$ is then generated as the rate of change of charge with respect to time:

$$i_s = d(V_{dc}C_s)/dt = V_{dc}\, dC_s/dt \tag{4}$$

$i_s$ is amplified by a negative gain determined by the feedback resistance $R_s$ and the output signal is a voltage signal $y$:

$$y = -R_s i_s \tag{5}$$

and $y$ thus becomes

$$y = -V_{dc}R_s \frac{dC_s}{dt} \tag{6}$$

where $C_s(x)$ is a function of capacitance with respect to the position $x$ (translational or rotational depending on the configuration of electrodes). Given that $V_{dc}$ and $R_s$ are known parameters, this circuit provide a linear measurement of $\frac{dC_s}{dt}$.

The advantage of this type of circuit is that it is simple to build and has fast response and less distortion compared to other more complex circuits, as it does not use many active components such as amplifiers or nonlinear elements such as multipliers or diodes that can introduce higher-order dynamics or delays. The disadvantage is that it is susceptible to

feedthrough disturbances introduced by parasitic capacitance to the driving voltage applied to MEMS devices for actuation. Despite these drawbacks, the direct measurement of $\frac{dC_s}{dt}$ can be very useful in at least three respects:

1. the measurement of $\frac{dC_s}{dt}$ can be integrated with respect to time and used to identify the capacitance vs. position function $C_s(x)$ if a synchronous position measurement is provided. A detailed identification method is described in Chapter 4 and Chapter 5.

2. the measurement of $\frac{dC_s}{dt}$ can be used as a source of velocity measurements for $\frac{dx}{dt}$, as long as $\frac{dC_s(x)}{dx}$ is identified, since

$$\frac{dC_s(x)}{dt} = \frac{dC_s(x)}{dx}\frac{dx}{dt}. \tag{7}$$

Such usage, and a complementary feedthrough reduction method, is described in Chapter 3.

3. the measurement of $\frac{dC_s}{dt}$ can serve as a sensitive indication for a threshold position, $x_{th}$, where maximum capacitance is reached due to maximal overlap of electrodes, i.e.

$$x_{th} = \arg\max_{x \in S_x} C_s(x) \tag{8}$$

where $S_x$ is a set of all admissible positions of $x$, which in practice is bounded by the maximum range of position that the MEMS device can achieve. Special signal processing techniques can be applied to extract this threshold position measurement and are discussed in detail in Chapter 4.

### 2.3 **Extended Kalman filter for nonlinear processes estimation**

As mentioned in Chapter 1, due to the unconventional electrode configurations of MEMS devices and applications studied in this work, the devices to be discussed here have nonlinear capacitance models. With sufficient modeling and/or experimental effort to characterize the dynamics of the actuation (process model) associated with a selected transduction technology (piezoelectric, electrostatic, electromagnetic, etc.), as well as the structure of the MEMS device,

motion estimation can be well fit into a nonlinear filtering scheme. Due to its computational efficiency [36], the extended Kalman filter (EKF) is chosen as the first approach for estimation in these applications, though other types of nonlinear filtering algorithm such as the unscented Kalman filter (UKF), particle filter, etc., exist. In one application of Kalman filtering to a MEMS micro-scanner, presented in Chapter 5, an UKF is implemented and its performance is compared to that of an EKF.

A Kalman filter is a realization of a Bayes filter to estimate states of a linear process having Gaussian distributions. It provides the optimal solution for a linear process in terms of minimizing the mean square error of estimation [37]. Since its publication in 1961 by Kalman and Bucy [38], the algorithm and its variations have been extensively used in applications such as navigation and tracking objects, chemical plant control and communications, etc. [39] [36]. In practice, the estimation problem can involve nonlinear processes. To deal with that, an EKF is often used due to its high computational efficiency, which is important for real-time applications [36]. The setting and the implementation of the EKF is described as below:

For a discrete-time controlled process governed by a nonlinear stochastic difference equation:

$$x_k = f(x_{k-1}, u_k) + w_k \tag{9}$$

and measurement model:

$$y_k = h(x_k) + v_k \tag{10}$$

where the subscript $k$ stands for k-th sampling instance, and $x_k$ is states of the controlled process, $u_k$ is the control input, $y_k$ is measurement. $f(\cdot)$ and $h(\cdot)$ stands for the nonlinear process model and measurement model respectively. The random variables $w_k$ and $v_k$ are

process and measurement noise respectively, and they are assumed to be independent of each other, and are modeled with zero-mean Gaussian distributions, i.e.,

$$p(w_k) \sim N(0, Q) \tag{11}$$

$$p(v_k) \sim N(0, R) \tag{12}$$

where $Q$ is the process noise covariance matrix and $R$ is the measurement noise covariance matrix. The EKF algorithm recursively predicts *a priori* estimates (an unconditional expectation) of the states, denoted as $\hat{x}_k^-$; and updates them with measurement information into *a posteriori* estimates (a conditional expectation) of the states, denoted as $\hat{x}_k$. More specifically, the estimation algorithm recursively computes the estimates as described below:

---

**Algorithm: EKF**

---

1. Prediction steps
   - compute *prior* state estimates and error covariance matrix

$$\hat{x}_k^- = f(\hat{x}_{k-1}, u_k), \quad P_k^- = F_k P_{k-1} F_k^T + Q$$

2. Measurement update steps
   - compute predicted measurement

$$\hat{y}_k = h(\hat{x}_k^-)$$

   - compute the optimal filter gain (Kalman gain)

$$K_k = P_k^- H_k^T (H_k P_k^- H_k^T + R)^{-1}$$

   - compute *posterior* state estimates and error covariance matrix

$$\hat{x}_k = \hat{x}_k^- + K_k(y_k - \hat{y}_k), \quad P_k = P_k^- - K_k H_k^T P_k^-$$

---

where $\hat{y}_k$ is the predicted measurement and $K_k$ is the optimal filter gain (also called as Kalman gain). $P_k^-$ is the *a priori* error covariance matrix and $P_k$ is the *a posteriori* error covariance matrix, defined as:

$$P_k^- = E[[x_k - \hat{x}_k^-][x_k - \hat{x}_k^-]^T] \tag{13}$$

$$P_k = E\big[[x_k - \hat{x}_k^-][x_k - \hat{x}_k^-]^T \mid y_k\big] \tag{14}$$

Notice that in order to perform the covariance matrix computation, a first order Taylor expansion is performed on both the nonlinear process and measurement models. More specifically, $F_k$ is the Jacobian of $f(\cdot)$ with first order Taylor expansion evaluated over $\hat{x}_{k-1}$ and $u_k$:

$$F_k = \frac{\partial f(\hat{x}_{k-1}, u_k)}{\partial x_{k-1}} \tag{15}$$

Similarly, $H_k$ is the Jacobian of $h(\cdot)$ with first order Taylor expansion evaluated over $\hat{x}_k^-$:

$$H_k = \frac{\partial h(\hat{x}_k^-)}{\partial x_k} \tag{16}$$

In this dissertation, one of the major focuses is to derive and identify accurate sensor models $h(\cdot)$ given a particular application and goal, capacitive sensor configuration, and associated sensing circuitry. The modeling efforts, identification methods, and associated feedthrough reduction methods are discussed in detail in Chapter 3 to Chapter 5.

# Chapter 3
# Motion Estimation of Micro-stage for in-situ MEMS Gyroscope Calibration

## 3.1 Chapter overview

We first examine a rotational, parallel-plate, on-chip capacitive sensor design and a motion estimation method for measuring multi-axis out-of-plane tilting motion of a micro-stage that is used for *in situ* calibration of an integrated MEMS gyroscope. On-chip sensing and motion estimation is critical for this application, since precision in measuring high frequency tilting motion of the micro-stage determines how accurately an on-stage MEMS gyroscope can be calibrated in the field with respect to this motion. To obtain decoupled sensing signals from multi-axis out-of-plane tilting motion, a capacitive sensing layout with high off-axis signal rejection capability is introduced. With the proposed design specifications and range of tilting motion, a dual axis capacitive sensor model is developed, and simulation results show that the sensor is able to reject more than 99.90% of the off-axis signal. The sensor also permits detection of perturbations to stage geometry due to ambient temperature variation through the effects of nonlinear behavior on signal timing. To measure tilting motion with the obtained sensing signal, a motion estimator with extended Kalman Filter (EKF) is also developed. With assistance of a laser Doppler vibrometer (LDV), experiments are performed to identify the parameters of the motion estimator and validate its performance. The experimental results demonstrate a 286 ppm error in scale factor calibration of a commercial MEMS gyroscope by the micro-stage with moderate temperature variation.

This chapter is organized as follows: Chapter 3.3 provides an overview of the micro-stage-based calibration method, a brief description of the PE stage and a description of the on-chip capacitive sensing stage. Chapter 3.4 introduces the modeling and estimation method used to measure the reference motion with on-chip capacitive sensor. Chapter 3.5 presents the experiments and post-processing procedures. Chapter 3.6 presents results and discussion, followed by Chapter 3.7 with a summary.

## 3.2 **Background and motivation**

Positioning and navigation are important to many modern vehicles, such as ships, aircraft, missiles, spacecraft, and UAVs [16]. A commonly used navigation framework for performing positioning and navigation consists of a signal receiver for the Global Positioning System (GPS) and an inertial navigation system (INS). Position estimation from both systems is integrated using a Kalman filter [16]. When the GPS signal is unavailable, the position estimation is conducted by the INS in stand-alone mode, and the accuracy of the estimation is critically dependent on the accuracy of its inertial measurement unit (IMU). In the last few decades, MEMS IMUs have overcome many shortcomings of their traditional counter-parts, especially in terms of cost, size, and power consumption. This has resulted in the development of GPS / MEMS IMU navigation applications, with examples demonstrated by Godha and Cannon in a land vehicle navigation [40] and in an autonomous helicopter by Wendel *et al.* [41].

However, MEMS IMUs suffer from substantial drift of scale factor and bias caused by perturbations of environmental factors, such as temperature [42]. Such drift results in accumulated errors of position estimation over time during operation in stand-alone mode, therefore limiting their application in navigation scenarios requiring high accuracy. Taking gyroscopes as an example, for tactical grade navigation, the scale factor error of a gyroscope

needs to be about 100 to 1000 ppm (parts per million or $10^{-6}$), or less than 10 ppm for inertial/strategic grade navigation [6] [43].

A standard method for calibrating an INS with triads of accelerometers and gyroscopes is to use a six-position and rate test. It requires the INS to be mounted on a perfectly leveled frame, and recording the different readings induced by earth's gravity. With this method it is possible to calibrate the scale factor, bias and non-orthogonality of the accelerometers by changing the orientation of the sensitivity axis of the accelerometers. A gyroscope is calibrated in a rate test by applying clockwise and counter-clockwise rotation with known magnitude around each gyro axis. A modified multi-position calibration method for MEMS IMUs has also been developed [44] [45]. This method relaxes the requirement of precise alignment of the IMU during calibration by taking readings from the IMU at multiple orientations within a turntable. Compared to the six-position and rate test, the modified multi-position calibration method does not require the orientations to be exactly known, therefore eliminating the need for the perfect alignment. The aforementioned calibration methods all require a rate table to provide precise rotation to the gyroscope, which requires substantial cost and manpower to perform and are impractical to be conducted in the field.

As a result of the above limitations, several researchers are focusing on the development of various in-field or *in situ* calibration methods. An in-field calibration method without external equipment was proposed by Lotters [46] to calibrate the scale factors and biases of a triad of accelerometers based on the principle that the measured accelerations by the triads of accelerometers must be equal to the earth's gravity. This methodology was further developed and led to the aforementioned modified multi-position method. Fong *et al.* [47] expanded this method to calibrate a MEMS IMU with three-axis accelerometers and three-axis gyroscopes

without external equipment by applying the following constraint: the gravity vector measured by triads of the acceleration equals to the gravity vector computed using attitude derived from the measurement of gyroscopes. In practice, since the reference for calibration is generated by the triad of accelerometers, the accuracy of calibration for the gyroscopes is limited by the precision of accelerometers and the obtained quasi-static states.

Some other methods utilize the MEMS gyroscope itself to do the calibration. For instance, there are ongoing works using virtual rate input for *in situ* calibration, where the virtual rate is generated by an amplitude modulated input applied to the driving and sensing electrodes of a MEMS gyroscope [48]. This is effective in some circumstances but also has its limitations, for instance that the virtual rate can vary due to aging of the gyroscope over its long-term use and implementation can be highly device specific.

An alternative emerging approach for *in situ* calibration is referred to in this work as micro-stage-based calibration. The core idea of the method is to migrate the actuation and sensing functionalities of performing in-lab IMU calibration, as by a rate table, into a MEMS micro-stage. The calibration process is realized by applying specific reference motions to the integrated MEMS IMU and comparing its measurements to the reference motion. The micro-stage is designed specifically to perform actuation and sensing tasks for *in situ* calibration and is realized with suitable MEMS fabrication technologies. The size of the micro-stage is comparable to that of MEMS IMU and would allow the calibration of IMU conveniently be carried out in the field.

Example micro-stage-based calibration of a gyroscope is reported by Aktakka *et al.* [49]. An important aspect of the micro-stage is to provide a reliable multi-axis reference motion. Nadig *et al.* [50] demonstrated a 3 DOF piezoelectric actuation with 50 ppm precision

performance, but on-chip sensing is lacking in the design which makes the long-term calibration process susceptible to an actuator's property changes. Aktakka and Najafi [17] presented a 6 DOF piezoelectric actuation stage (PE stage) with less than 0.1% off-axis tilting motion (off-axis motion is defined as the undesired motion other than the reference motion generated by other axis). Obtaining highly accurate knowledge of the reference motion applied by these stages with on-chip sensor and/or estimator is crucial for calibration. The reference motion can be referred from a pre-calibrated voltage-motion relationship of the stage or can be measured via on-chip sensing. Edamana *et al.* [29] presented sensing and estimation with high-accuracy threshold sensing angles for improved estimation of reference motion, and the estimation scheme was implemented with mixed on-chip piezoelectric sensing and off-chip optical measurements. Chen *et al*. [51] have developed a single axis capacitive sensor model to measure tilting motion, but neither of the latter works present experimental validation for scale factor calibration of an on-chip MEMS IMU. Furthermore, the use of a multi-axis on-chip sensor also calls for a method to evaluate the impact of off-axis motion to the accuracy of calibration.

This chapter aims to address these issues by presenting a dual axis capacitive sensor model that can be used to evaluate the capability of the sensor to reject off-axis signals, as well as track changes in sensor parameters, particularly nominal capacitive gap, as ambient conditions change. With the proposed sensor design and its characteristic nonlinear mapping between capacitance and tilting motion, a corresponding parameter identification framework is proposed and can be used in situations when key sensor parameters may be perturbed due to temperature change. Based on the inherent nonlinear relationship between angular displacement and capacitance, a motion estimator based on an EKF is developed. With the assistance of a laser Doppler vibrometer (LDV) for initial system identification and later validation, the motion

estimator is experimentally implemented and validated. Finally, the performance of on-chip capacitive sensor and motion for *in situ* calibration is experimentally validated through scale factor calibration of a MEMS gyroscope at two ambient temperature settings.

## 3.3 **Description of micro-stage based calibration**

### 3.3.1 Gyroscope model and scale factor calibration

In this section, we evaluate how various non-ideal features of capacitive sensing propagate to calibration errors in a general micro-stage and inertial sensor context. To introduce the calibration procedure, we begin at a generic relationship between motion of the gyroscope and its outputs.

For a 3-axis gyroscope, input motions are collected as:

$$\boldsymbol{\Omega} = \begin{bmatrix}\omega_x & \omega_y & \omega_z\end{bmatrix}^T \tag{17}$$

where $\omega_x$, $\omega_y$, $\omega_z$ are angular velocities experienced by the gyroscope in the $x$, $y$, and $z$ axes in its body frame, respectively. The angular velocities measured (or output) by the gyroscope are denoted as:

$$\boldsymbol{\Omega_I} = \begin{bmatrix}\omega_{I,x} & \omega_{I,y} & \omega_{I,z}\end{bmatrix}^T \tag{18}$$

The relation between $\boldsymbol{\Omega_I}$and $\boldsymbol{\Omega}$ can be represented as:

$$\begin{bmatrix}\omega_{I,x}\\ \omega_{I,y}\\ \omega_{I,z}\end{bmatrix} = \underbrace{\begin{bmatrix}k_{xx} & k_{xy} & k_{xz}\\ k_{yx} & k_{yy} & k_{yz}\\ k_{zx} & k_{zy} & k_{zz}\end{bmatrix}}_{\boldsymbol{K}} \begin{bmatrix}\omega_x\\ \omega_y\\ \omega_z\end{bmatrix} + \begin{bmatrix}\omega_{I0,x}\\ \omega_{I0,y}\\ \omega_{I0,z}\end{bmatrix} \tag{19}$$

where in the 3 by 3 scale factors matrix $\boldsymbol{K}$, the diagonal terms $k_{xx}$, $k_{yy}$ and $k_{zz}$ are the scale factors for each axis and the off-diagonal terms represents the cross-axis sensitivities, as caused by misalignments of axes of the triads of the gyroscopes [45]. $\omega_{I0,x}$, $\omega_{I0,y}$ and $\omega_{I0,z}$ are biases of the corresponding outputs.

The standard laboratory calibration method for a gyroscope is based on angular rate tests. It requires the gyroscope be mounted on a precise rate table and be applied a series of predefined reference motion by the rate table, namely different angular rates in clockwise and counter-clockwise direction. The scale factors, biases, and cross-axis sensitivities can then be identified via a parameter identification approach such as least-square estimation. The time period for identified scale factors and biases to vary is considered significantly longer than the time required to perform the calibration with the rate table or micro-stage (seconds to tens of seconds).

In the calibration approach presented here, the MEMS IMU is mounted on the micro-stage, and the tilting motion of $x$ and $y$ axes can be excited independently with less than 0.1% off-axis coupling [17], therefore the calibration of each gyroscope axis is performed with insignificant off-axis motion disturbance. Without losing generality, we examine the calibration of a single output channel of a MEMS gyroscope, and present the analysis and the experimental results with respect to $x$-axis as the representative example in this chapter. The single axis gyro model is simplified as:

$$\omega_I = k_I \omega + \omega_{I0} \tag{20}$$

where $\omega_I$ is the measured gyroscope output, $\omega$ is the angular velocity experience by the gyroscope, $k_I$ and $\omega_{I0}$ are the scale factor and bias for the corresponding axis.

Prior to scale factor calibration, the parameter $k_I$ in (4) is not assumed to be known. Rather, it is to be inferred from reference angular velocities, $\omega$, actuated by the micro-stage. However, the stage's dynamic response may vary over time as well. So the reference velocity must in turn be monitored by the stage's on-chip sensing. The angular velocity estimated from the stage's sensors, $\omega_s$, can be summarized by

$$\omega_S = k_S\omega + \omega_{S0} \tag{21}$$

where $k_S$ is the scale factor and $\omega_{S0}$ is the bias of the stage.

Additional actuation and sensing is only beneficial if it can be performed, for at least some excitations, with higher accuracy than the uncalibrated performance of the gyroscope. Stage velocities are measured using features of the on-chip capacitance with errors that can be estimated from the error covariance matrices of EKF, by methods described in later sections. Substituting for $\omega_R$ by the measured $\omega_s$, (4) becomes

$$\omega_I = \frac{k_I}{k_S}\omega_S + (k_S\omega_{I0} - k_I\omega_{S0})/k_S \tag{22}$$

or

$$\omega_I = k_{I|S}\omega_S + \omega_{I|S} \tag{23}$$

where $k_{I|S}$ is defined as the IMU scale factor given reference motions observed by the stage, and $\omega_{I|S}$ is defined as the IMU bias given reference motions observed by the stage.

Scale factor $k_{I|S}$, taken to represent $k_I$ if $k_S$ can be maintained close to one, is obtained through repeated periodic excitation of the stage at varying amplitudes. After collecting measurements of $\omega_S$ and $\omega_I$ at various amplitudes, a set of pairs of estimated angular velocities and IMU output measurements are obtained. These are averaged over many stage vibration oscillations to reduce measurement noise. Specifically, for a set of $n$ trials at different driving voltages, one can obtain $2n$ sets of observations regarding the reference motions, one is from IMU, denoted by $n$x1 column vector $\boldsymbol{\Omega_I}$:

$$\boldsymbol{\Omega_I} = \begin{bmatrix}\omega_{I,1} & \omega_{I,2} & \cdots & \omega_{I,n}\end{bmatrix}^T \tag{24}$$

and another from the stage, denoted by $n$x1 column vector $\boldsymbol{\Omega_S}$:

$$\boldsymbol{\Omega_S} = \begin{bmatrix} \omega_{S,1} & \omega_{S,2} & \cdots & \omega_{S,n} \end{bmatrix}^T \tag{25}$$

The parameter to be estimated are defined as $\boldsymbol{\Theta} = \begin{bmatrix} k_{I|S} \\ \omega_{I|S} \end{bmatrix}$ and letting $\boldsymbol{\Omega_{S,I}} = [\boldsymbol{\Omega_S}\ \boldsymbol{I}]$ be an $n$x2 vector, where $\boldsymbol{I}$ is $n$x1 unitary column vector, then

$$\boldsymbol{\Omega_I} = \boldsymbol{\Omega_{S,I}}\boldsymbol{\Theta} \tag{26}$$

The parameters solved by least square estimation become

$$\boldsymbol{\Theta} = \left(\boldsymbol{\Omega_{S,I}^T}\boldsymbol{\Omega_{S,I}}\right)^{-1}\boldsymbol{\Omega_{S,I}^T}\boldsymbol{\Omega_I} \tag{27}$$

### 3.3.2 Micro-stage based calibration

Fig. 3.1 illustrates the idea of the micro-stage-based calibration: the stage incorporates an on-stage actuator and a set of sensors, and it serves as a mini rate-table source in the calibration process for the integrated MEMS IMU. Taking MEMS gyroscope calibration as an example, with a specific driving voltage, a sinusoidal rotational vibration (often referred to as tilting motion in the context of this dissertation) with specific amplitude and frequency is generated by the on-stage actuator, and the tilting motion is measured by both the on-stage MEMS gyroscope and the on-chip sensors (with necessary signal processing). The measurements from the gyroscope and stage itself are then compared for calibration of the MEMS gyroscope.

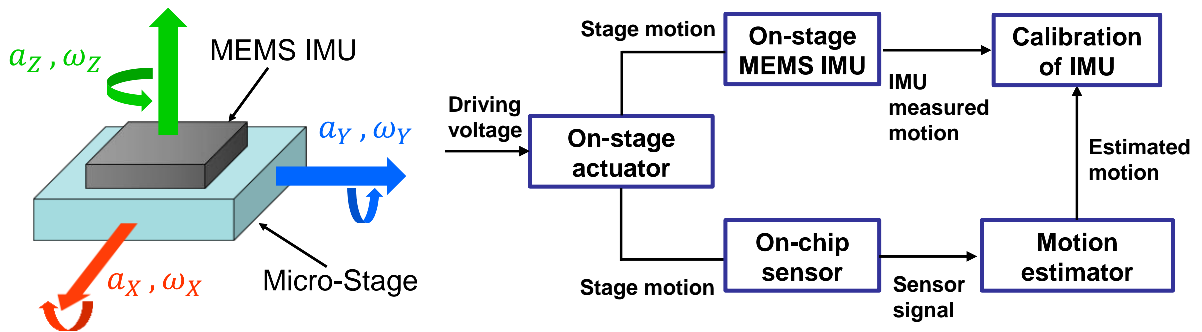


**Fig. 3.1. Illustration of micro-stage and MEMS IMU (left) and flowchart of micro-stage based calibration method (right).**

### 3.3.3 Piezoelectric actuation stage

The micro-stage studied in this Chapter consists of a piezoelectric actuation stage, a capacitive sensing substrate and an integrated 6-axis MEMS IMU [17]. The piezoelectric actuation stage is able to perform both translational motion and rotational motion in $X$, $Y$ and $Z$ directions. The multi-axis actuation capability also allows the stage to reduce the off-axis tilting motion within 0.1 % of the amplitude by compensating off-axis motion [17]. Fig. 3.2 illustrates the geometric correlation between the integrated MEMS IMU, piezoelectric actuation stage and on-chip capacitive sensors for X and Y tilting motion. More details regarding the actuation stage and dynamics of actuation can be found in [17].

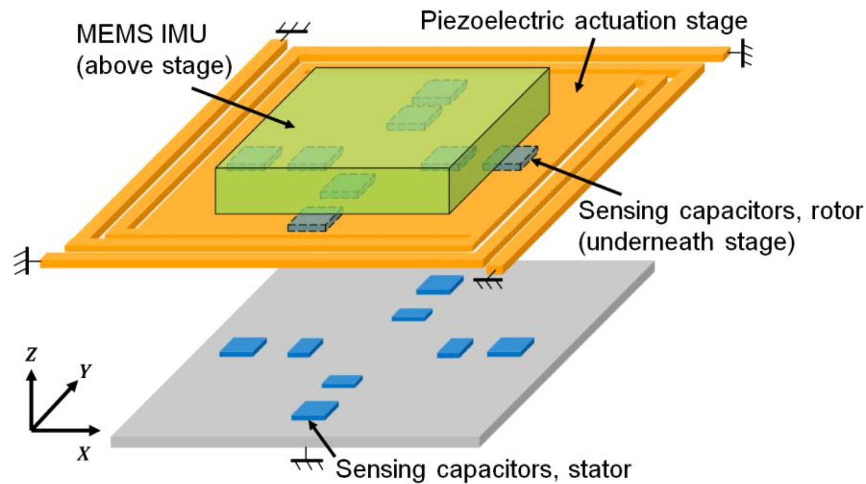


**Fig. 3.2. A schematic of micro-stage with integrated 6-axis MEMS IMU, the stage includes a piezoelectric actuation stage with 6 DOF motion generation capability and a capacitive sensing stage for measuring $X$ and $Y$ tilting motion. The schematic is to illustrate the major internal configurations of micro-stage and the dimensions are not scaled to the true dimensions of the device.**

### 3.3.4 On-chip capacitive sensor

The goal of *in situ* calibration imposes stringent requirements on the size of the stage, which translate into requirements for high sensitivity, small size and low power consumption from the chosen sensing technology. Due to its high sensitivity, mature fabrication process, compact design and low-power dissipation, capacitive sensing becomes a natural choice for this application [1]. However, the scale factor and bias of capacitive sensor themselves are

susceptible to environmental perturbations, which calls for unique design features and that are robust to such perturbation.

To fulfill such requirements, a capacitive sensor is designed to measure $X$ and $Y$ tilting (out-of-plane rotational) motion of the stage. As illustrated by the cross-section side view shown in Fig. 3.3, the sensing stage is assembled underneath the actuation stage, and is composed of silicon pillars with specific geometry. To measure the tilting motion about each single axis, 4 pairs of electrodes with the top to be the rotor and the bottom to be the stator are fabricated to form 4 capacitors. When the PE stage rotates along one axis, the capacitance, $C$ of each capacitor varies depending on its placement and the angular displacement, $\theta$. As shown in the top view of the sensor layout in Fig. 3.3, the rotors and stators are placed along the central axes in order to minimize the sensing current generated by off-axis rotation. The areas of the rotor electrodes are identical, whereas the areas of the inner stators are intentionally designed smaller than that of the outer stators. Such design allows for imbalanced capacitance to be generated at a specific angle, which can potentially improve the precision of estimation of angular position [51]. Additional capacitive sensors are also designed to sense translational motion in $X$ and $Y$ directions, and the detailed layout and dimensions of electrodes are shown in Fig. A.1 of the Appendix.

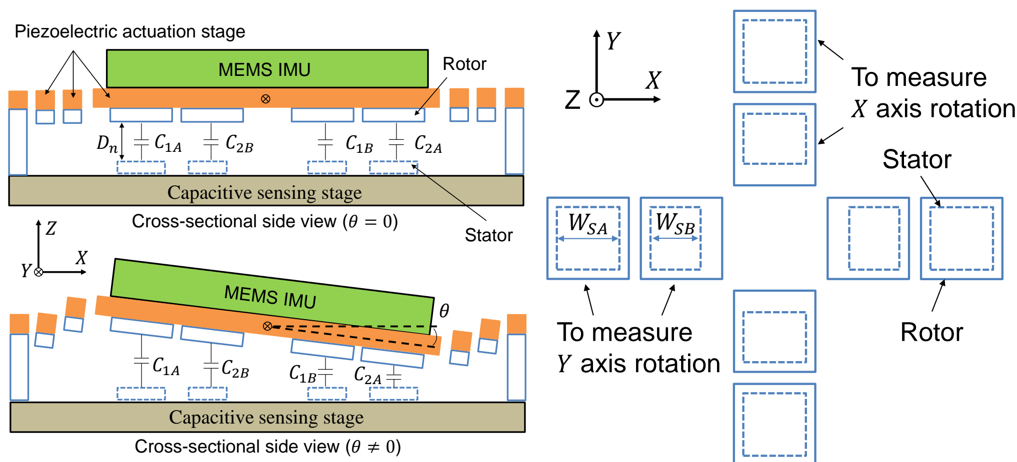


**Fig. 3.3. Integrated micro-stage and MEMS IMU (left, cross-sectional side view) and design of capacitive sensor for *X* and *Y* tilting motion (right, top view).**

To convert the capacitance change caused by tilting motion into a measurable voltage signal and to reduce the parasitic capacitances and noise from the interconnections and circuits, an integrated charge sensing circuit using a transimpedance amplifier is implemented [52]. A differential readout circuit was initially used with each pair of opposite capacitors connected, but it was found not able to fully cancel out feedthrough and noise, attributed to differences in parasitic across pairs of electrodes. While additional parasitic modeling might address this issue, in the current work a post signal processing method is used to reduce the disturbance of feedthrough and noise as described in section 4.4, and each individual capacitor is used as a single channel in order to increase number of signal channels. Other types of amplitude modulation and demodulation based circuit can be potentially used as well, but the additionally introduced distortion to the signal could also affect the accuracy of estimation of tilting motion.

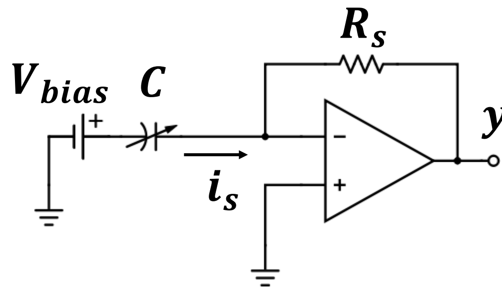


**Fig. 3.4. A schematic of the sensing circuit for the capacitive sensors; a transimpedance amplifier is used to convert the current generated by the variable capacitance into measurable voltage.**

As shown in Fig. 2.3, a variable capacitor and a transimpedance amplifier comprises a single sensing channel. With a DC bias voltage, $V_{bias}$ applied to the common node of the sensing capacitor, a sensing current $i_s$ is amplified by a negative gain determined by the feedback resistance $R_s$ and is measured as a sensing signal $y$ (voltage signal), according to:

$$y = -R_s i_s \tag{28}$$

Since the sensing current $i_s$ is the rate of change of charge with respect to time, and $V_{bias}$ is DC voltage, we have

$$i_s = d(V_{bias}C)/dt = V_{bias}\, dC/dt \tag{29}$$

and $y$ becomes

$$y = -V_{bias}R_s\, dC/dt \tag{30}$$

where $C$ is a function of capacitance with respect to the tilting angles. For the purpose of evaluating the off-axis tilting motion to the sensing signal, a dual axis capacitive sensor model is derived in Chapter 3.4.3, and simulations are performed to compare it with its single model in Chapter 3.6.1.

## 3.4 **Motion estimation**

### 3.4.1 Overview of motion estimator

According to Eq.3, the sensing signal, $y$ is a function of $dC/dt$, and $C$ is a nonlinear function of $\theta$ (described in detail Section 3.3). Therefore, without the knowledge of $C(\theta)$, it is not possible to directly solve for the states related to tilting motion of the actuation stage, including $\theta$ and angular velocity, $\omega$ from sensing signal $y$. To address this issue, a motion estimator with an EKF to estimate $\theta$and $\omega$ is developed, which includes the knowledge of the dynamics of the PE actuation stage, capacitive sensing mechanism and available measurements including driving voltages and measured signal from on-chip sensor.

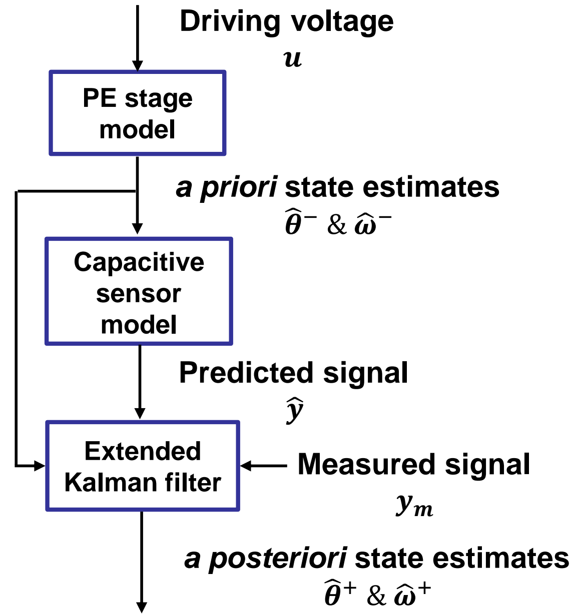


**Fig. 3.5. Overview of the micro-stage motion estimator; the extended Kalman filter is used to integrate the PE stage model and capacitive sensor model to compute *a posteriori* state estimates of tilting motion with the measurement of the applied driving voltage and capacitive sensor signal.**

More concretely, as depicted in Fig. 3.5, the estimation pipeline starts with the measured driving voltage $u$ as input into the model of PE stage, and outputs *a priori* state estimates as $\hat{\theta}^{-}$ and $\hat{\omega}^{-}$ (The superscript $^{-}$ stands for *a priori* or estimate without measurement; $^{+}$ stands for *a posteriori* or estimate with measurement and $\hat{}$ stands for estimated quantities). The capacitive sensor model is then updated with $\hat{\theta}^{-}$. Then the EKF uses the updated sensor model, measured signal and the *a priori* state estimates to compute *a posteriori* estimates $\hat{\theta}^{+}$ and $\hat{\omega}^{+}$. The model for the PE stage and capacitive sensor and the EKF are described below.

### 3.4.2 Model of PE stage

A model of the PE stage has been developed to predict the out-of-plane tilting motion with an input driving voltage for a specific range of driving frequencies. For the PE stage tested in this study, the first natural frequency is measured to be 1002 Hz for the vertical translation mode (Fig. 3.6, left) [17], and the second natural frequency is measured to be around 1715 Hz for the tilting mode (Fig. 3.6, right)..

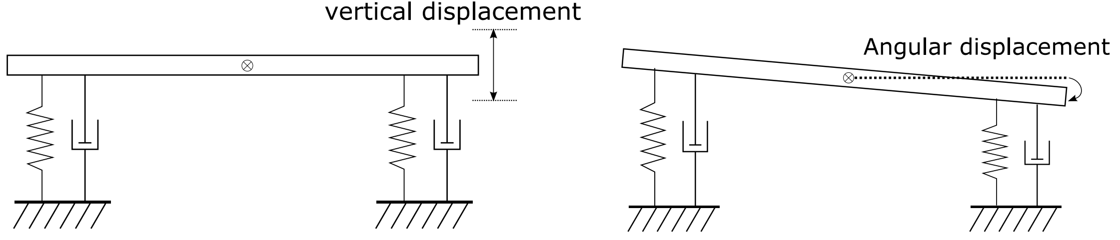


**Fig. 3.6. Illustration of vertical translation mode (1st natural frequency) and single axis tilting mode (2nd natural frequency) of PE stage**

It is worth mentioning that the first resonant frequency is designed to be above 1 kHz to avoid low frequency mechanical vibrations from the environment to be amplified by the micro-stage. In a more practical *in situ* calibration application, an iterative learning control loop or other feedback controller can be used to damp out disturbance from the environment, as suggested in [29]. In this study, the experiments were performed on an optical table as a standard lab procedure, with mechanical vibrations from environment negligible after filtering.

Due to the existence of parasitic capacitance within the micro-stage and associated printed circuit boards and chip packaging, a feedthrough signal is introduced into the sensing system. In order to reduce this feedthrough signal (proportional to driving voltage) while obtaining as large as possible motion signal, the driving frequency was chosen to be around the second resonant frequency (tilting mode) to permit a low driving voltage amplitude. . Due to the symmetric placement of actuators and control of phases of driving voltages, the vertical displacement of stage is measured to be at the nanometer level under the tilting excitation mode. Therefore, a 2nd-order linear time-invariant (LTI) model for the tilting mode of the PE stage around second natural frequency is considered sufficient for estimation purpose. The tilting motion presented in Fig. 3.6 can be characterized in a state space representation as

$$\dot{x} = A_c x + B_c u \tag{31}$$

where in the state vector, $x = \begin{bmatrix} \theta \\ \omega \end{bmatrix}$, $\theta$ and $\omega$ are angular displacement and angular velocity of the PE stage with respect to the corresponding center axes, respectively, $u$ is driving voltage. $A_c$ is an $\mathbb{R}^{n_x \times n_x}$ state matrix and $B_c$ is an $\mathbb{R}^{n_x \times n_u}$ input matrix. While the dimensions of $A_c$ and $B_c$ can be expanded for a study of a multi-input-multi-output estimation and control, in this study we focus on studying single-axis tilting motion, such that $n_x$ is set to be 2 within the estimation accuracy provided by other sources of error. Due to the fact that voltages on the electrodes of the PZT structures are identical and either exactly in-phase or 180° out-of-phase with same or proportional amplitudes, only one representative driving voltage needs to be recorded, and $n_u$ is 1. Then, $A_c$ and $B_c$ are defined as the following:

$$A_c = \begin{bmatrix} 0 & 1 \\ -\omega_n^2 & -2\zeta\omega_n \end{bmatrix} \tag{32}$$

$$B_c = \begin{bmatrix} 0 \\ b_c \end{bmatrix} \tag{33}$$

where $\omega_n$ is the relevant natural frequency of the PE stage, and $\zeta$ is its damping ratio. In implementation, the state representations are discretized at the sampling frequency as follows:

$$x_k = A_d x_{k-1} + B_d u_k \tag{34}$$

where $x_k$ is the discretized states, $u_k$ is the discretized driving voltage, and $A_d$ and $B_d$ are the $\mathbb{R}^{n_x \times n_x}$ and $\mathbb{R}^{n_x \times n_u}$ discretized state matrix and input matrix, respectively.

### 3.4.3 Model of capacitive sensor

A single axis capacitive sensor model has been developed in [51] with an assumption of no off-axis tilting motion. Although the assumption is valid with good off-axis motion control ($<$ 0.1%) provided by the stage presented [17], it is desirable from a design point of view to quantify the sensor's capability for rejecting the signal caused by off-axis tilting motion. Therefore, a dual axis capacitance model was developed and is presented below.

To map the angular displacement $\theta$ into the sensing signal $y$, we first start with the parallel plate of capacitance formulation

$$C = \frac{\varepsilon_r \varepsilon_0 A}{D} \tag{35}$$

where $\varepsilon_r$ is the relative static permittivity (1 for air), $\varepsilon_0$ is the electric constant ($8.8542 \times 10^{-12}$ F m$^{-1}$), $A$ is the area of overlap between the two plates, and $D$ is the distance between two plates. When two plates are no longer parallel due to the tilting motion, $A$ and $D$ will change according to the position and geometry of the plates, resulting in a change of capacitance $C$.

As depicted in Fig. 3.7, a coordinate system is defined with the origin defined to be the center of the PE stage. For the purposes of this derivation, the $Y$ axis is selected as the main-axis of rotation and the $X$ axis is the off-axis of rotation. A rotor and stator pair is defined with the rotor lying in the nominal horizontal plane ($XY$ plane) and the stator underneath. $\theta_Y$ (positive defined to be clockwise with $Y$ axis pointing away from observer) is the angular displacement of the main-axis and it is defined as the angle between the $X$ center line of the rotor and the $XY$ plane, and $\theta_X$ (positive defined to be clockwise with $X$ axis pointing away from observer) is the angular displacement of the off-axis and it is defined as the angle between the $X$ center line of the rotor and the $X'Y$ plane.

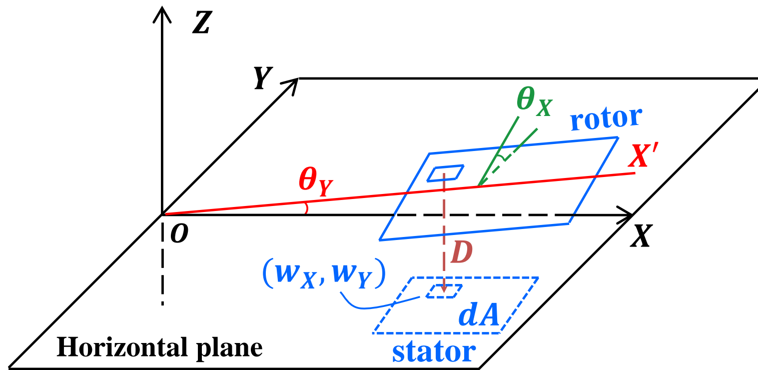


**Fig. 3.7. A depict of a capacitor formed by a pair of silicon rotor and stator with existence of rotations about both $X$ (off-axis rotation) and $Y$ (main-axis rotation) axes. The capacitance as a function of $\theta_X$ and $\theta_Y$ (positive to be clockwise with axes pointing away from observer) is derived based on the geometric relation between the rotor and stator.**

The capacitance formed by an arbitrarily small differential element of a rotor electrode and its underlying stator is expressed as

$$dC = \frac{\varepsilon_0 \varepsilon_r dA}{D} \tag{36}$$

where $dA$ is the finite area on the stator projected from the rotor, and $D$ is the variable distance between the two finite areas. $dA$ is simply the product of the finite lengths of $dw_X$ and $dw_Y$, where $w_X$ and $w_Y$ are the coordinates of the finite area of the stator:

$$dA = dw_X * dw_Y \tag{37}$$

By trigonometry, $D$ can be expressed as

$$D = D_n - w_X tan\theta_Y + w_Y tan\theta_X \tag{38}$$

where $D_n$ is the neutral distance between plates. Then $dC$ can be re-written as

$$dC = \frac{\varepsilon_0 \varepsilon_r dw_X dw_Y}{(D_n - w_X tan\theta_Y + w_Y tan\theta_X)} \tag{39}$$

The total capacitance formed by the rotor and stator can be computed by evaluating the double integral:

$$C = \int_{w_Y=w_3}^{w_Y=w_4} \int_{w_X=w_1}^{w_X=w_2} \frac{\varepsilon_0 \varepsilon_r dw_X dw_Y}{(D_n - w_X tan\theta_Y + w_Y tan\theta_X)} \tag{40}$$

Eq.13 can be evaluated as

$$C(\theta_X, \theta_Y) = \frac{-\varepsilon_0 \varepsilon_r}{tan\theta_X tan\theta_Y} [g(w_2, w_4) - g(w_2, w_3) - g(w_1, w_4) + g(w_1, w_3)] \tag{41}$$

with

$$g(w_X, w_Y) = [(D_n - w_X tan\theta_Y + w_Y tan\theta_X)\, ln(D_n - w_X tan\theta_Y + w_Y tan\theta_X)] - w_Y tan\theta_X \tag{42}$$

where $w_1$, $w_2$, $w_3$ and $w_4$ are lower and upper limits of definite integration defined by the dimensions and geometric relation between plates. The values of those limits together with the illustration are listed in Table A.1 and Fig. A.1 in the Appendix.

To further expand the sensing readout described by Eq.3, $\frac{dC}{dt}$ can be expressed as

$$\frac{dC(\theta_X,\theta_Y)}{dt} = \frac{\partial C}{\partial \theta_X}\frac{\partial \theta_X}{\partial t} + \frac{\partial C}{\partial \theta_Y}\frac{\partial \theta_Y}{\partial t} = [\frac{\partial C}{\partial \theta_X} \ \ \frac{\partial C}{\partial \theta_Y}]\begin{bmatrix}\omega_X\\ \omega_Y\end{bmatrix} \tag{43}$$

and let

$$h(\theta_X, \theta_Y; \eta, D_n) = \eta[\frac{\partial C}{\partial \theta_X} \ \ \frac{\partial C}{\partial \theta_Y}] \tag{44}$$

be a state-dependent gain of the capacitive sensor. $\eta$ is the effective gain of amplification and $D_n$ is the neutral distance between plates, and $P_s = [\eta, D_n]$ is a set of parameters describing the sensor to be tuned upon assembly of the sensing stage and over later environmental perturbations. The dual axis capacitive sensor model can be expressed as

$$y = h(\theta_X, \theta_Y; P_s)\begin{bmatrix}\omega_X\\ \omega_Y\end{bmatrix} \tag{45}$$

To obtain a single axis capacitance model, a similar derivation can be followed with assumption of the tilting angle of the off-axis equals to zero. For instance, by assuming $\theta_X = 0$, one can get

$$C(\theta_Y) = \frac{-\varepsilon_r\varepsilon_0(w_4-w_3)}{tan\,\theta_Y} ln(\frac{D_n-w_1tan\theta_Y}{D_n-w_2tan\theta_Y}) \tag{46}$$

and the single axis capacitive sensing model is

$$y = h(\theta_Y; P_s)\omega_Y \tag{47}$$

It should be pointed out that the small angle approximation can be applied in the above derivation, i.e. $\theta \approx sin\theta \approx tan\theta$ to <50 ppm error, therefore one can use $\theta$ or $sin\theta$ to replace $tan\theta$ in Eq. 15 and Eq. 19 with little effect on estimation results at the levels of accuracy obtained in this work. Thanks to the nonlinear relation between $C$ and $\theta_X$, $\theta_Y$, the signal generated by ordinary sinusoidal tilting motion exhibits unique traits (Fig. 3.12) that can be used to aid identification of $P_s$, which will be further discussed in Section 4.4.

### 3.4.4 Integration with EKF

The PE stage model and the capacitive sensor model are integrated with the EKF to compute *a posteriori* state estimates. As will be shown in section 3.6.1, by analyzing the signal

outputs from the dual-axis capacitive sensor model and the single-axis capacitive sensor model, the designed capacitive sensor is capable of negating the effects of off-axis tilting motion. Therefore, it is then sufficient to use a single-axis capacitive sensor model in the estimator itself. Details of the estimation scheme are described below and summarized in Fig. 3.8.

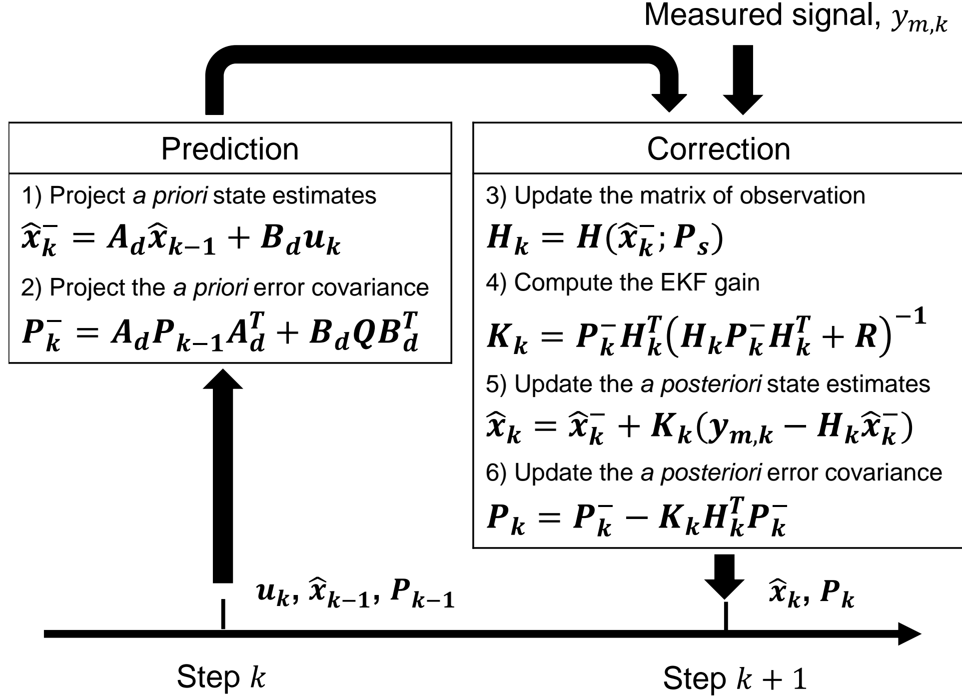


**Fig. 3.8. Detailed EKF routine for motion estimation. The matrix of observation is updated with *a priori* estimate of angular position, at each step of estimation.**

Step1. Project *a priori* state estimates,

$$\hat{x}_k^- = A_d\hat{x}_{k-1} + B_d u_k \tag{48}$$

with the PE stage model described in Eq.7, where the subscript $k$ stands for $k$-th step in the estimation routine, $\hat{x}_k^-$ stands for *a priori* state estimates at the $k$-th step, $\hat{x}_k^- = \begin{bmatrix} \hat{\theta}_k^- \\ \hat{\omega}_k^- \end{bmatrix}$, $\hat{x}_{k-1}$ is the *a posteriori* state estimates at the $(k-1)$-th step, $\hat{x}_{k-1} = \begin{bmatrix} \hat{\theta}_{k-1} \\ \hat{\omega}_{k-1} \end{bmatrix}$, $u_k$ is the measured driving

voltage at the $k$-th step, and $A_d$ and $B_d$ are the discretized state and input matrices that model the dynamics of the PE stage.

Step 2. Project the *a priori* error covariance,

$$P_k^- = A_d P_{k-1} A_d^T + B_d Q B_d^T \tag{49}$$

where $P_k^-$ is the a priori error covariance matrix at the k-th step, $P_{k-1}$ is the a posteriori error covariance matrix at the $(k-1)$-th step, and Q is the covariance matrix of process noise.

Step 3. Update the matrix of observation,

$$H_k = \begin{bmatrix} 0 & h(\hat{\theta}_k^-; P_{s,1}) \\ \vdots & \vdots \\ 0 & h(\hat{\theta}_k^-; P_{s,n_y}) \end{bmatrix} \tag{50}$$

for $H_k$ as the matrix of observation at the $k$-th step, $n_y$ the number of capacitive sensors ($n_y$ can be 1 to 4 depending on number of sensing channels used), and $P_{s,1}$ to $P_{s,n_y}$ representing the corresponding tuned parameters of the capacitive sensor model; the capacitive sensor model used in this estimation scheme is based on Eq.20. Since $h$ depends on $\theta$, it is necessary to update the $h$ at every step with $\hat{\theta}_k^-$ in this estimation scheme.

Step 4. Compute the EKF gain,

$$K_k = P_k^- H_k^T (H_k P_k^- H_k^T + R)^{-1} \tag{51}$$

using the a priori estimate error covariance matrices $P_k^-$ and $H_k$. R is the covariance matrix of measurement noise.

Step 5. Update the *a posteriori* state estimates by

$$\hat{x}_k = \hat{x}_k^- + K_k(y_{m,k} - H_k \hat{x}_k^-) \tag{52}$$

where $\hat{x}_k$ is the a posteriori state estimates at the k-th step, and $y_{m,k}$ is the measured signal at k-th step.

Step 6. Update the *a posteriori* estimation error covariance

$$P_k = P_k^- - K_k H_k^T P_k^- \tag{53}$$

where $P_k$ is the *a posteriori* estimate error covariance matrix at the k-th step

## 3.5 **Experiments and parameter identification**

### 3.5.1 Overview of methods

Open-loop experiments have been previously carried out to evaluate the multi-axis actuation functionality of the micro-stage [17]. Owing to the good off-axis motion compensation provided by the actuation stage and off-axis signal rejection provided by the sensor, the estimation of multi-axis tilting motion can be decoupled into estimation of the tilting motion around each single axis. Various experiments have been performed to examine the capacitive sensors for both the *X* and *Y* axes, and representative results with respect to a sample axis are presented in this study.

To obtain an accurate *a posteriori* estimate of the tilting motion, it is necessary to first identify the parameters of each component in the motion estimator with accurate external measurements. With only on-chip capacitive sensors such measurements cannot be obtained prior to the calibration of the motion estimator, therefore an off-stage laser Doppler vibrometer (LDV) system was used to provide ground-truth measurement.

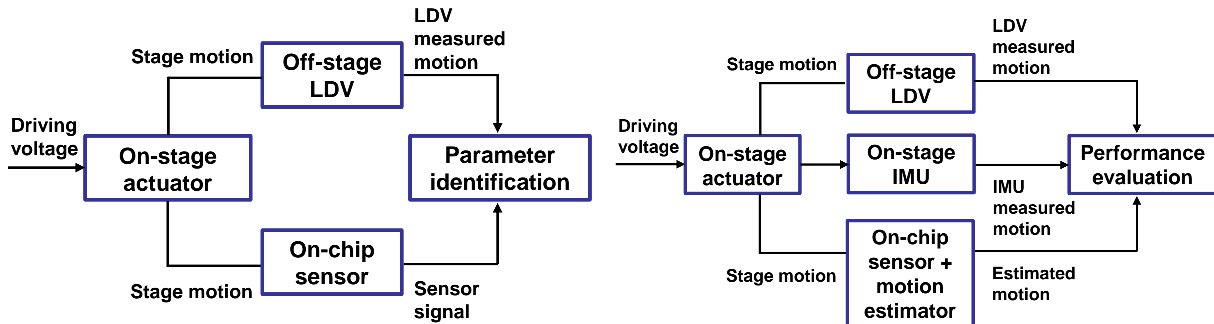


**Fig. 3.9. Block diagram of components involved in parameter identification (left) and the performance evaluation during IMU calibration (right).**

The parameter identification and performance evaluation phases of micro-stage testing are illustrated in Fig. 3.9. During the parameter identification phase, the stage was excited by a driving voltage with a specific frequency and amplitude, and the tilting motion was measured with the on-chip capacitive sensor and off-stage LDV. The parameters of the models for the PE stage and capacitive sensor and the EKF were then identified, respectively.

In the performance evaluation phase, the stage was excited again with different voltage settings and the tilting motion was measured by 3 different types of sensors: the on-chip capacitive sensor plus motion estimator without LDV input, on-stage MEMS gyroscope, and off-stage LDV. The performance was then evaluated in terms of the accuracy of $\omega$ estimation, the scale factor and bias of the motion estimator itself, and the calibration error of scale factor for on-stage MEMS gyros. The motion measured by the LDV was used as the reference motion for both the initial parameter identification and the performance evaluation phases, but only to validate estimator performance in the latter.

### 3.5.2 Description of setup

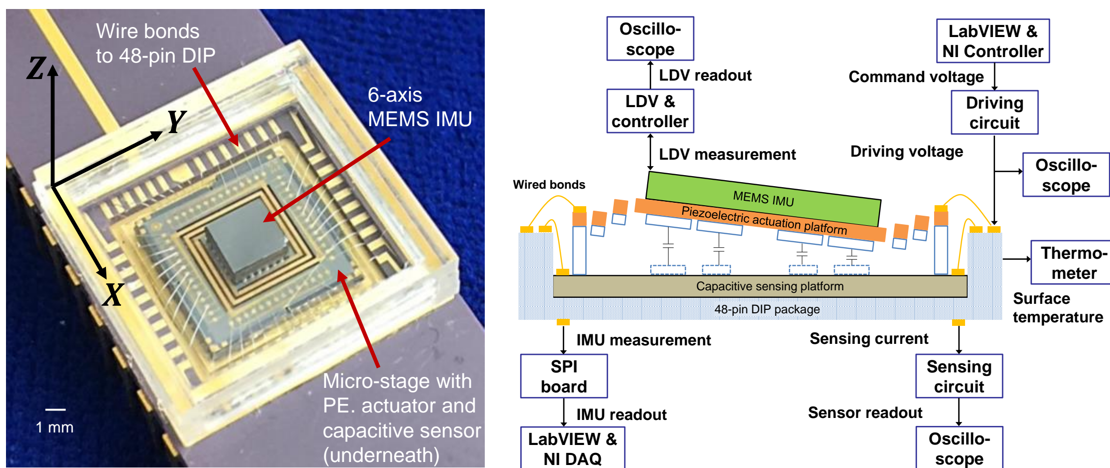


**Fig. 3.10. A photo (left) of miro-stage (9 × 9 mm) with a 6-axis InvenSense MPU-6500 MEMS IMU (3 × 3 × 0.9 mm) as payload and a schematic (right) of experimental set-up. A LDV is used to measure the tilting motion for parameter identification and performance evaluation of motion estimator.**

As depicted in Fig. 3.10 [17], an InvenSense MPU-6500 is used as the on-stage MEMS IMU to be calibrated. It consists of a 3-axis gyroscope and 3-axis accelerometers, and a LDV system was used to measure out-of-plane tilting motion generated by the PE stage. For the purpose of performance evaluation of on-chip capacitive sensor and motion estimation, the key specs of the gyroscope are summarized in Table 3.1.

**Table 3.1. Specifications of the InvenSense MPU-6500 gyroscope [53]**

[1] Derived from validation or characterization of parts, not guaranteed in production.

| Specifications | Value |
|---|---|
| Full scale range | ±250 dps to ±2000 dps<br>(±4.4 rad/s to ±34.9 rad/s) |
| Scale factor error (at 25°C) | ±3 % |
| Bias error (at 25°C) | ±5 dps |
| Scale factor variation over temperature (-40°C to +85°C) [1] | ±4 % |
| Cross-axis sensitivity | ±2 % |
| Total RMS noise | 0.1 dps - rms |

The overall experimental set-up consisted of a Polytec OFV-534 sensor head with a 20x objective lens, a Polytec OFV-5000 vibrometer controller and a VD-09 velocity decoder with gain of 20 mm/s/V. In order to maximize the measured velocity signal and obtain a high signal-to-noise ratio, the observation point of the LDV was located at the surface of the MEMS IMU that was at the center of the studied edges. Since the tilting angle is small (± 0.005 rad), the measured velocity can be approximated as the vertical velocity of the edge, and the measured velocity, $V_{edge}$ is converted to angular velocity $\omega$ as:

$$\omega = \frac{2V_{edge}}{W_{IMU}} \tag{54}$$

where $W_{IMU}$ is the width of the MEMS IMU.

In order to achieve higher sampling speed, the data acquisition and log tasks were implemented using an Agilent InfiniiVision MSO-X 3024A oscilloscope. The analog signals from the capacitive sensing circuits, LDV, and the amplified driving voltage were acquired at 12.5 MHz by the oscilloscope, and the measurements were saved at 625 kHz with a 1024-period averaging enabled for the purpose of noise reduction. The IMU readout was acquired using a serial peripheral interface (SPI) board. The actuation of the PE stage was realized using a National Instruments controller and voltage amplification with a LabVIEW user interface.

A heater was used to change the ambient temperature of the set-up for temperature perturbation tests, while an OMEGA HH802U digital thermometer was used to continuously monitor the surface temperature of the DIP package. In this experiment, plastic foam was used to wrap the lens and sensor head of the LDV for thermal isolation and to minimize the impact of temperature perturbation on the LDV's performance.

### 3.5.3 Description of experiments

To limit feedthrough signals while obtaining as large a tilting motion signal as possible, the excitation frequency was chosen to be near the second resonant frequency (~1715 Hz), which is a resonant mode of the stage associated with $Y$ axis tilting. Operation near a resonance allows the stage to reach its desired tilting amplitude at relatively low voltage input, and therefore lower the feedthrough signal generated. The relatively high resonant frequency also generates large angular velocity with modest amplitude of tilting motion (Eq.20), therefore it not only allows the MEMS gyro to be calibrated over a wider range of velocities, but also increase strength of the signal generated by the capacitive sensor and thus the signal to noise ratio. The operating settings of reported experiments are summarized in Table 3.2.

The first experiment was done to identify the parameters of the model of PE stage. In this experiment, the frequency of a sinusoidal driving voltage was swept from 1711 Hz to 1719 Hz with constant amplitude (0.8 V) while the frequency response of the system was recorded.

The second experiment was conducted to validate off-axis signal rejection of capacitive sensor. In this experiment, the frequency of the driving voltage was set to be 1700 Hz, and the amplitude of the driving voltage was swept from 1.1 V to 2 V to generate variation of tilting rate. During the experiment, the active off-axis motion compensation was turned off to allow the stage to experience certain off-axis motion, and the LDV was used to measure both the main axis tilting motion and the off-axis tilting motion. The measured tilting motions were fed into the single axis sensor model (with main tilting motion as input) and the dual axis sensor model (with both main and off-axis tilting motion as input), and the discrepancy between the output signals are quantified. Detailed analysis and results is shown in section 5.1.

The third experiment was conducted to calibrate and the capacitive sensor model, EKF, and to evaluate the performance of motion estimator and the calibration error of scale factor for the MEMS gyro. In this experiment the ambient temperature of the set-up was changed by 12.8 ℃ by an external heater to produce a shift of scale factor and bias of the MEMS gyro. The frequency of the driving voltage was set to be 1700 Hz and the amplitude of driving voltage was swept from 1 V to 1.3 V to produce a variation in the tilting rate, and measurements of capacitive sensor, LDV and MEMS gyro are all recorded. At each temperature setting, the collected data was split into training and testing sets, with the training set used to calibrate the parameters of the capacitive sensor model and EKF, and the testing set used to evaluate the motion estimator's performance and to calibrate MEMS gyro. The performance of the motion estimator and IMU are compared in sections 3.6.2 and 3.6.3.

**Table 3.2. Summary of experiments and operational settings**

| Purposes of experiment | Driving frequency (Hz) | Voltage amplitude (V) | Range of $\omega_{pp}$ (rad/s) | Temperature (℃) |
|---|---|---|---|---|
| Identify PE stage model | 1711 to 1719 | 0.8 | 48.5 to 54.3 | 22.8 |
| Validate off-axis signal rejection | 1700 | 1.0 to 2.0 | 29.7 to 67.0 | 21.3 |
| Identify sensor model, EKF; calibrate MEMS gyro | 1700 | 1.0 to 1.3 | 29.5 to 46.3 | 22.9 and 35.7 |

### 3.5.4 Parameter identification and post-processing

To mitigate the feedthrough signal, a feedthrough cancellation method [17] was applied by taking two consecutive measurements with sensing bias voltage on and off, and the difference of the two measurements was computed as the signal induced by the tilting motion. In addition, the LDV output was found to have a delay of approximately 6.9 $\mu s$ compared to the on-chip capacitive sensor measurement. This delay was compensated by shifting the LDV measurement with the identified value. The recorded LDV measurements were also discovered to have a constant bias, and it was compensated during the post-process. A low pass filter and a detrending filter were applied to the measured signals for the purpose of reducing noise and bias.

The natural frequency of the resonance being excited (In this study, it is the 2$^{nd}$ mode of the stage) $\omega_n$ and the damping ratio $\zeta$ of the stage resonance were identified using the circle-fit method [54], the identified Nyquist curve fit and frequency response are shown in Fig. 3.11 and the results are listed in Table 3.3.

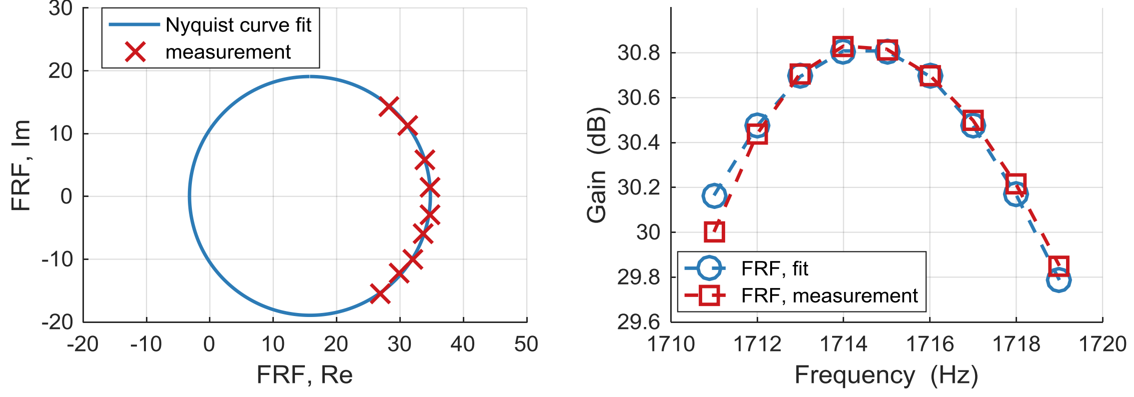


**Fig. 3.11. Nyquist curve fit and frequency response of single axis tilting mode**

In the proposed estimation scheme, the fidelity of the capacitive sensor model is crucial to the final estimation accuracy. As shown in Eq.17, the parameter set $P_s$ to be identified contains $D_n$ (neutral distance between plates) and $\eta$ (effective gain of amplification). To distinguish relevant signals, the measured readout from the capacitive sensor is defined as the measured signal, $y_m$, whereas the output of capacitive sensor model (with LDV measured $\theta$ as input) is defined as a predicted signal, $\hat{y}$. The identification process is to find the optimal parameter set, $P_s^*$ that matches the key features between measured signal and predicted signal, as described in the equation below:

$$P_s^* = arg\,min \sum_{i=1}^{N}[f(y_m) - f(\hat{y})]^2 \tag{55}$$

Here, $f$ is a function designed to extract key features from input signal. During the identification process, $f$ was designed to

a. Identify $D_n$ by matching the crest-to-trough distance, $\lambda$ of the waveform

b. Identify $\eta$ by matching the amplitude of the waveform

The reason behind identifying $D_n$ by matching $\lambda$ is from the factor that by taking derivative of $y$, one obtains $\frac{dy}{dt} = -V_{bias}R_s\frac{d^2C}{dt^2}$. Therefore, by imposing $\frac{dy}{dt} = 0$ (crest or trough of the waveform) one will get solutions for $\frac{d^2C}{dt^2} = 0$ which contain $\theta$ and $D_n$. During stage

identification, one can substitute the measured $\theta$ value (by LDV) into the solutions to solve for the optimal $D_n$ (numerically) that minimizes the error of $\lambda$ extracted from the predicted signal and measured signal. The advantage of such approach is that $\lambda$ is invariant with respect to the gain of amplifier, therefore it is possible to decouple the tuning of gap and gain. Fig. 3.12 demonstrated that $\lambda$ changes with respect to the gap of the plates.

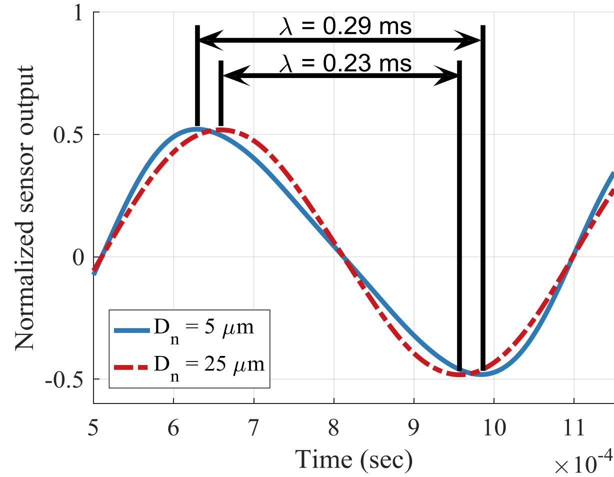


**Fig. 3.12. Due to the nonlinear relation between $C$ and $\theta$, the sensing signal output by the capacitive sensor model shows that the crest-to-trough distance $\lambda$ changes as $D_n$ changes, such a feature is extracted and used to identify optimal $D_n$.The amplitude of the signals are normalized (- 0.5 to 0.5) with respect to their own amplitude for comparison purpose.**

The identified $D_n$ and $\eta$ are also listed in Table 3.3.

**Table 3.3. Identified parameters of model of PE stage and capacitive sensor at room temperature**

| Parameter | Description | Value |
|---|---|---|
| $\omega_n$ | $2^{nd}$ natural frequency | 1714.5 Hz |
| $\zeta$ | Damping ratio | 0.005 |
| $b_c$ | DC gain | 3782.5 rad/s$^2$/V |
| $D_n$ | Neutral distance between plates | 19.2 $\mu m$ |
| $\eta$ | Effective gain of amplification | -2.40752 $\times 10^7$ |

The covariance of measurement noise $R$ is identified by computing the covariance of measurement collected with zero input voltage. The covariance of process noise $Q$ is identified by computing the error of covariance by a-prior estimated states and LDV measured states.

The *a posteriori* state estimates from the EKF is used to compute the error of scale factor and bias of the motion estimator, and they are corrected by compensating the *a posteriori* state estimates as the last step of parameter identification process.

## 3.6 **Results and discussion**

### 3.6.1 Evaluation of off-axis signal rejection by capacitance sensor

To evaluate the performance of the micro-stage, several aspects of performance have been examined. First and foremost, to quantify the off-axis signal rejection of the capacitive sensor, an off-axis signal rejection ratio $R_{off}$ is defined to quantify the percentage of rejected off-axis motion in the capacitive sensor readout by comparing the outputs from single axis sensor model and dual axis sensor model:

$$R_{off} = 1 - \frac{E_y}{\bar{\omega}_{off}/\bar{\omega}_{main}} \quad (56)$$

where $E_y$ is defined as

$$E_y = \sqrt{\frac{1}{N}\sum_{i=1}^{N}\left(y_{single,i} - y_{dual,i}\right)^2} \quad (57)$$

where $y_{single,i}$ is the $i$-th point of signals simulated by single motion capacitive sensor model and $y_{dual,i}$ is the $i$-th point of signals simulated by dual motion capacitive sensor model, and $N$ is the number of sample points used for simulation.

A simulation was performed with the measured tilting angle in the 2$^{nd}$ experiment (Table 3.2) fed into the single and dual axis sensor model respectively. The ranges of the main-axis motion to be $\pm$ 0.003 rad, and the off-axis motion ratio is swept from 1% to 50% by scaling the measured off-axis motion accordingly. The result (Table 3.4) suggests that with the provided range of tilting motion, even the off-axis tilting motion is as large as 50 % of that of the main-axis, the proposed capacitive sensor design is still able to reject as much as 99.90 % of the

disturbance signal. Therefore, we conclude that with the range of tilting motion performed and the amount of the off-axis motion the micro-stage experienced during the experiments, the off-axis motion does not have significant impact on the signal measured by the corresponding capacitive sensors, and therefore is not the major source of error in the motion estimation. This conclusion ensures that using single-axis capacitive sensor model is sufficient for the estimation scheme and simplifies its implementation.

**Table 3.4. Off-axis signal rejection ratio, $R_{off}$ with respect to off-axis motion ratio**

| $\bar{\omega}_{off}/\bar{\omega}_{main}$ | $R_{off}$ |
|---|---|
| 1 % | 99.98 % |
| 10 % | 99.98 % |
| 50 % | 99.90 % |

From Fig. 3.13, we can see that with identified parameters and 10 % of off-axis motion assumed, the difference between the identified capacitance profiles and output signals from single and dual axis sensor models (for main-axis tilting motion) are insignificant.

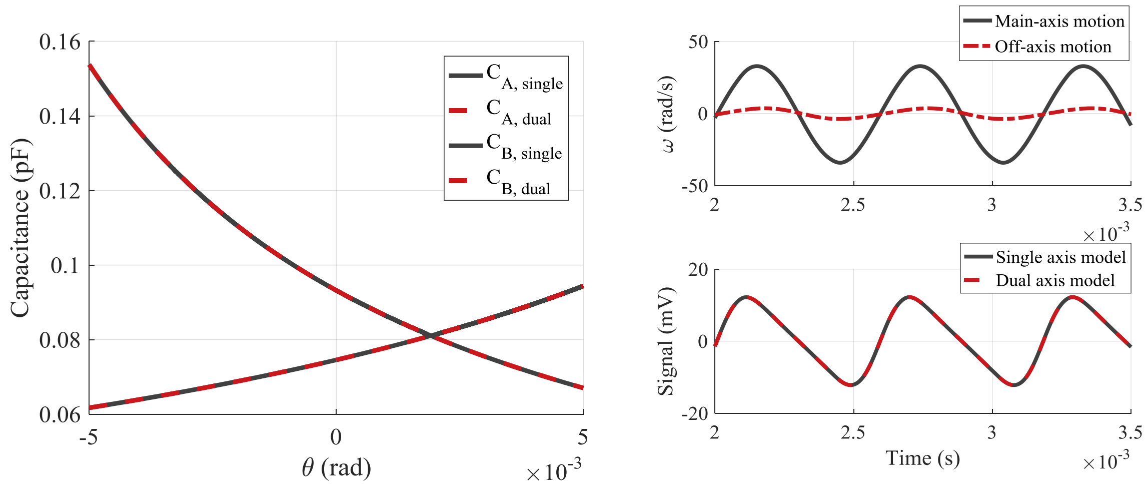


**Fig. 3.13. Identified capacitance profiles for two representative channels from both single and dual axis capacitive sensor models (left), and two simulated time domain signals from the two sensor models (for main-axis tilting motion) respectively (right). The simulation assumes 10 % of off-axis motion for demonstration purpose.**

### 3.6.2 Validation of motion estimation

In this section, performance metric are defined to evaluate the accuracy of *a posteriori* angular velocity estimate and its scale factor and bias. All the results were evaluated using the testing data set which was not used in the parameter identification process, and the LDV measured angular velocity was used as reference measurement. For the purpose of simplicity and clarification, the *a posteriori angular* velocity estimate will be referred as $\omega_{EST}$, and "by the on-chip capacitive sensor and motion estimator" will be referred to as "by stage" in the following sections. To evaluate the estimation accuracy of $\omega$ measured by stage, a root-mean-square error (RMSE) of $\omega$ is defined as

$$\omega_{RMSE} = \sqrt{\frac{1}{N}\sum_{i=1}^{N}\left(\omega_{EST,i} - \omega_{LDV,i}\right)^2} \tag{58}$$

where $N$ is the total number of samples used for evaluation. During the evaluation, the $\omega$ values in time series were averaged into one cycle for noise reduction, and $N$ was the total number of samples in one cycle.

To evaluate how accurately angular velocity of the micro-stage can be measured by stage, the scale factor $\alpha$ and bias $\beta$ of the stage are defined as

$$\omega_{EST} = \alpha\omega_{LDV} + \beta \tag{59}$$

To compute the $\alpha$ and $\beta$, one can take $N$ group of measurements to form

$$\Omega_{EST} = \Omega_{LDV}\Theta \tag{60}$$

where $\Omega_{EST} = \begin{bmatrix}\omega_{EST,1}\\ \vdots \\ \omega_{EST,N}\end{bmatrix}$, $\Omega_{LDV} = \begin{bmatrix}\omega_{LDV,1}\\ \vdots \\ \omega_{LDV,N}\end{bmatrix}$ and $\Theta = \begin{bmatrix}\alpha\\ \beta\end{bmatrix}$, and $\Theta$ can be computed by least square method as

$$\Theta = (\Omega_{LDV}^T\Omega_{LDV})^{-1}\Omega_{LDV}^T\Omega_{EST} \tag{61}$$

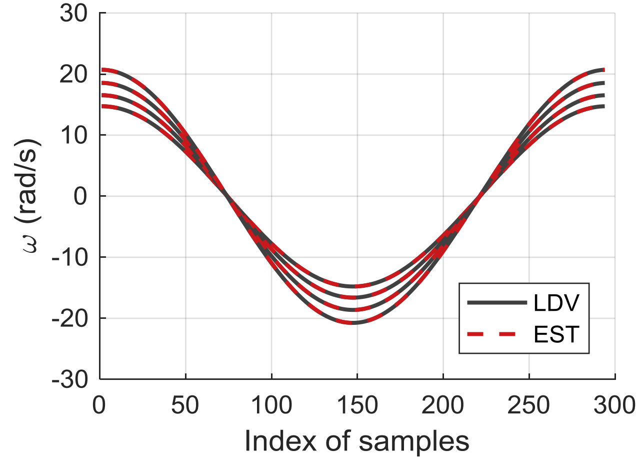


**Fig. 3.14. Comparison of angular velocities, $\omega$, measured by LDV (black) and (red) by stage in the testing data set, the waveforms are averaged into one period for noise reduction and demonstration purpose.**

The results of evaluation at room temperature are shown in Fig. 3.14 and summarized in Table 3.5. Notice that once the parameters were identified with the training data set, the results were evaluated with a separate testing data set, in which the LDV measurements were only used in the comparison of the output of motion estimator. The validation result shows a $\omega_{RMSE}$ of 0.1140 rad/s and a mean $\alpha$ of 1.0008, which mean an error of 0.08 %.

**Table 3.5. Validated RMSE, average scale factor and bias of $\omega_{EST}$ of stage at room temperature**

| $\omega_{RMSE}$ (rad/s) | $\alpha$ (unit less) | $\beta$ (rad/s) |
| --- | --- | --- |
| 0.1140 | 1.0008 | - 0.0207 |

### 3.6.3 Calibration of MEMS IMU

Finally, the scale factor of MEMS gyroscope was evaluated by the on-chip capacitive sensor and motion estimator (referred as stage for simplicity), and compared to the scale factor evaluated by the LDV. When computing scale factor of the gyroscope, only the peak to peak $\omega$ measurements were used, this is due to the instrumentation setting that the IMU readout was asynchronously sampled at about 8 kHz and logged with respect to other measurements in the experiments. To take into account of asynchronously sampling issue, producing the same

expected value, in a statistical sense, from both on-chip sensors and the IMU, the averaged $\omega$ measurement at ±15 sample points around the peak and bottom of the waveform of the estimated $\omega$ are used to compute the peak to peak $\omega$. As shown in Fig. 3.15, $\omega_{pp}$ measured by the IMU, stage and LDV were fetched from time series data (noted as $\omega_{IMU,pp}$, $\omega_{EST,pp}$ and $\omega_{LDV,pp}$ respectively) and used to compute perform least square as:

$$\Theta_{IMU} = (\Omega_{REF}^{T}\Omega_{REF})^{-1}\Omega_{REF}^{T}\Omega_{IMU} \tag{62}$$

where $\Theta_{IMU} = \begin{bmatrix} SF_{IMU} \\ B_{err} \end{bmatrix}$, $SF_{IMU}$ is the scale factor of MEMS gyroscope evaluated with corresponding measured reference motion, $\Omega_{IMU} = \begin{bmatrix} \omega_{IMU,pp,1} \\ \vdots \\ \omega_{IMU,pp,n} \end{bmatrix}$, $\Omega_{REF} = \begin{bmatrix} \omega_{REF,pp,1} \\ \vdots \\ \omega_{REF,pp,n} \end{bmatrix}$ and $\Omega_{REF}$ can be measurement either from motion estimator or LDV respectively. Measurement of $\omega_{IMU,pp}$ recorded under two temperatures were first calibrated against $\omega_{LDV,pp}$ at room temperature to serve as an initial calibration of IMU, as a necessary step for the comparison purpose. The scale factors of the MEMS gyroscope are then evaluated as described in Eq.(35) under the corresponding temperature settings.

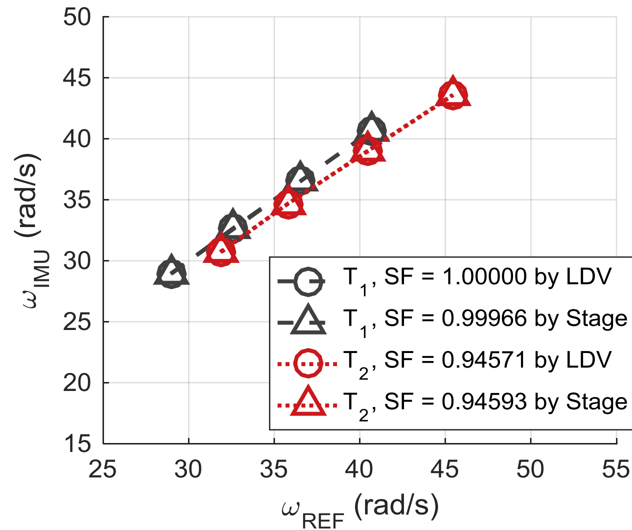


**Fig. 3.15. peak-to-peak $\omega_{IMU}$ vs. $\omega_{REF}$, $\omega_REF$ (measured by LDV and stage respectively) Scale factor of MEMS gyroscope under two temperature settings are computed by least square method and then compared.**

The $SF_{IMU}$ evaluated by two reference measurement under two temperature settings are listed in Table 3.6. At room temperature, the $SF_{IMU}$ measured by LDV and stage differs by –340 ppm. When the surface temperature rises from 22.9 ℃ to 35.7 ℃ (the increase of temperature was limited by instrumentation's capabilities), the $SF_{IMU}$ evaluated by LDV is 0.94571(-5.43 %), while the stage reports it to be 0.94593, which differs from that of LDV by 220 ppm. It should be pointed out the scale factor variation due to temperature reported by the datasheet is $\pm 4\%$, which can be interpreted as a typical MEMS gyro of this kind is expected to experience a variation of ± 4% in scale factor under the temperature range from -40 ℃ to 80 ℃. However, as pointed out by the datasheet itself, this level of variation is not guaranteed in production, nor in a more realistic application. As matter of fact, in this experiment the tested MEMS gyro already shows more than 5% change given a temperature rise of 12.8 ℃. The errors of calibration of scale factor (286 ppm as root mean square) demonstrated in this study are improvement of several orders of magnitude compared to the direct look-up table compensation of scale factor employed in the MEMS gyroscope.

**Table 3.6 Scale factors and biases measured by LDV and stage with two temperature settings**

| Scale factor | $T_1$ = 22.9 ℃ | $T_2$ = 35.7 ℃ |
|---|---|---|
| $SF_{IMU}$ by LDV | 1.00000 | 0.94571 |
| $SF_{IMU}$ by stage | 0.99966 | 0.94593 |
| $SF_{IMU}$ difference | -340 ppm | 220 ppm |

It is worth noting that the calibration error of scale factor of MEMS gyro only uses peak to peak angular velocities, and the scale factor error of the stage reported in Table 3.5 is computed from all the measured angular velocities. The latter is a measure of correlation between the reference motion and the estimates in the full range of tilting rate, which is more prone to distortion of the estimated waveform than just using the peak to peak values. The source

of distortion of the waveform can come from the residual feedthrough, noise, and the mismatch between the capacitance model and the true capacitance in the device, if any. Therefore it is possible for the scale factor error of the stage to be larger than the scale factor error of calibration of the MEMS gyro in this case. With that said, the experimental results demonstrate the methodology is capable of calibrating scale factor of MEMS gyroscope with moderate temperature perturbation from the environment.

### 3.6.4 Benchmarks and source of error

Representative results of in-situ calibration of scale factor of MEMS gyroscope are presented in Table 3.7 for the purpose of comparison.

**Table 3.7 Comparison of representative reported in-situ calibration results of MEMS gyroscope scale factor**

| Method | Best scale factor calibration accuracy | External equipment | Features |
|---|---|---|---|
| Virtual input rate [55] | 350 ppm | None | Apply a known self-generated dither signal into the sense-mode of gyro as virtual input for calibration |
| Virtual input rate [56] | 0.35% (10 – 50 ℃) | None | Virtual electrical rotation mimicked with symmetry of the dual-mode architecture |
| Pseudo-observation by hand [57] | 1200 ppm | None | Introduce pseudo-observations for calibration |
| Micro-stage actuator [58] | 1 % | A micro-stage with piezoelectric actuation and an optical metrology system | Multi axis calibration with on-chip actuation |
| Micro-stage actuator and [29] | 258 ppm | A micro-stage with piezoelectric actuation and sensing with optical | Threshold position sensing provided for high accuracy reference motion |

| | | sensing | estimation |
|---|---|---|---|
| Micro-stage actuator and sensor (our method) [59] | 286 ppm (23 ℃– 36 ℃) | A micro-stage with piezoelectric actuation and capacitive sensing | Multi axis calibration with on-chip actuation and sensing |

The results are categorized by methodology and whether external hardware is involved. The best accuracies reported by the literatures are also tabulated. Among, the method presented in this dissertation distinguishes from all the other methods that involve using external equipment by relying on only on-chip sensing capability.

In order to understand the source of error in the calibration, a sensitivity analysis has been conducted by sweeping the key parameters of sensor model, the induced calibration errors are illustrated in Fig. 3.16 [60].

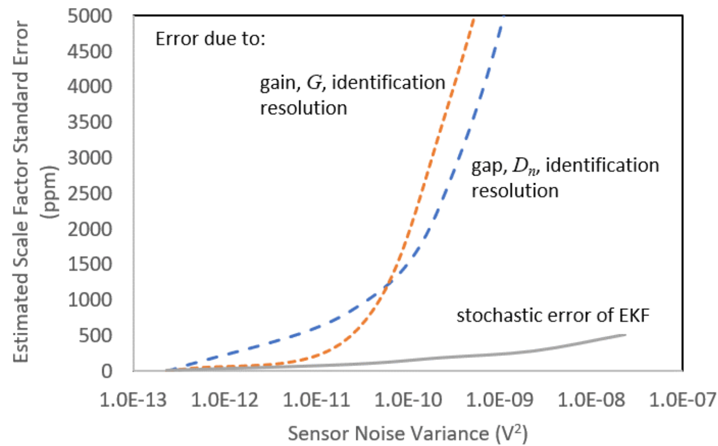


**Fig. 3.16 Estimated standard deviation of scale factor error (in ppm) as a function of sensor noise variance, based on EKF error covariance and Monte Carlo simulation of noise influence on parameter identification accuracy.**

The standard deviation of scale factor calibration error due to the sensor noise via three different contributing mechanisms is illustrated in Fig. 3.16. The noisy sensor measurement is assumed to generate errors in either the parameter identification of $D_n$ and $G$ or estimation error of EKF with a perfectly identified model. The key observation from Fig. 3.16 is that inaccurately identified parameters in the capacitive sensor model caused by noisy measurement is a much

more significant source of error than the direct influence of sensor noise on EKF performance ("stochastic error").

### 3.7 **Chapter Summary**

In this chapter, we introduce a rotational parallel-plate capacitive sensor design and a motion estimation method for measuring multi-axis tilting motion of a micro-stage that is used for *in situ* calibration of an on-stage MEMS IMU. The developed multi-channel capacitive sensor and motion estimator is capable of measuring dual-axis out-of-plane tilting motion of the 6 DOF piezoelectric actuated micro-stage, with high off-axis signal rejection ratio and ability to detect and compensate for effects from environmental perturbations.

To evaluate the off-axis signal rejection capability of the sensor, a dual axis capacitive sensor model is derived and calibrated using its characterized nonlinear relation between capacitance and tilting angle. The dual-axis sensor model is compared with a single axis sensor model in a simulation, and the simulation result shows that the proposed capacitive sensor design rejects substantial off-axis signal (above 99.90 % with provided range of motion).

To measure the tilting motion with the on-chip capacitive sensor, a motion estimator incorporating a PE stage model near resonance, a capacitive sensor model, and an EKF is developed. A series of experiments are conducted to identify the parameters of the motion estimator and evaluate its performance, with an LDV used to serve as ground truth measurement of the reference motion. The experimental results show the motion estimator with the capacitive sensor has a RMSE of 0.1140 rad/s and an error of scale factor of 0.08 %. In another experiment with two ambient temperature settings, the experimental results show that the micro-stage with on-chip capacitive sensor and motion estimator reports an RMS error of scale factor of a MEMS gyroscope to be 286 ppm over 13 ℃ temperature range, improved by several orders of

magnitude compared to the expected scale factor drift of the MEMS gyroscope utilized under the same temperatures change.

# Chapter 4
# Threshold Sensing with Micro-scanner

## 4.1 Chapter overview

From the last chapter, it has been discussed that the capacitive sensor for analog measurement is susceptible to geometry and material property changes caused by temperature and other environmental variation. To overcome this issue, in this chapter we exploit a threshold sensing mechanism and implement a threshold signal detector to improve the state estimation accuracy of an EKF. The approach is validated experimentally with a MEMS electrostatic micro-scanner. A first order derivative of Gaussian (DOG) filter is used to detect and locate rapid changes in voltage signal caused by crossing of a threshold angle determined by maximum overlap of capacitive electrodes. The event-triggered measurement is used in the update step of the EKF to provide intermittent but more accurate angle measurements than those of the capacitive sensor's continuous output. Experiments on the electrostatic micro-scanner show that with the threshold signal detector incorporated, the average position estimation accuracy of the EKF is improved by 15.1%, with largest improvement (30.3%) seen in low signal-to-noise ratio (SNR) conditions. A parametric study is conducted to examine sampling frequency and capacitance profile, among other factors that may affect detection error and EKF accuracy.

This chapter is structured as follows: Chapter 4.2 introduces background on the DOG filter, and the EKF; Chapter 4.3 presents the process model, sensor model and EKF implementation; Chapter 4.4 presents the experimental setup; Chapter 4.5 presents the results of

parametric studies of factors that can impact estimator performance; Chapter 4.6 presents experimental results; Chapter 4.7 provides a summary.

## 4.2 **Background and Motivation**

### 4.2.1 Impact of temperature on capacitive sensing and prior studies

As was encountered in Chapter 3, a major drawback of capacitive sensing is that its accuracy may be reduced by temperature and other environmental effects, which can cause undesired changes in geometric relations between electrodes [42] [61]. One potential solution is to find features of the sensing signal that correspond to specific positions that are both detectable and constant in the presence of unwanted geometric perturbations [32]. Such signal features can be used for measurement of threshold positions with high accuracy to "reset" position estimates and improve overall motion tracking accuracy. Design of capacitive sensors that generate threshold features can be intentional or a natural consequence of electrode geometry for a given application.

This chapter introduces novel threshold signal detector realized with a derivative of Gaussian (DOG) function in the loop of an EKF. It is intended to enhance angular position and velocity estimation for MEMS micro-scanners. The study explores factors impacting the performance of the estimation scheme, such as noise level, capacitance profile of the sensor, sampling rate, etc.

Among prior research works, the idea of using threshold sensing to improve motion tracking can be found in Henningsson and Astrom's work [30], in which a sensor provided a measurement of the center mass of a MEMS accelerometer exceeding a threshold location; however, that literature did not discuss the realization of such a sensing mechanism. In [51], a design of an out-of-plane capacitive sensor using imbalanced capacitance to indicate threshold

location was proposed; however, extraction of the signal was susceptible to drift of its capacitive signal. In [29], a Kalman filter estimation scheme with an asynchronized sensing scheme was proposed, in which a less accurate but frequently-measured analog signal and a highly accurate but infrequent (twice per period of a waveform) threshold signal were used in a Kalman filter estimator. That work, however, again did not address the issue of how to extract the threshold signal and assumed perfect detection. [32] proposed using a DOG filter to detect threshold crossing signals and embedded its output as a more accurate source of measurement updates within a Kalman filter estimator. However, experimental results were not presented, and issues such as sampling rate and how to fully incorporate a non-linear capacitive sensor model were not addressed.

Given the limitations of previous works, it is desirable to study factors that can affect the usage of threshold sensing in an EKF: how is the detection error distributed and can it be well-modelled by normal distributions? What is the relationship between the variance of error and factors including sensor design (capacitance profile) and operating conditions (sampling rate, noise)? How should one pick suitable parameters for the DOG filter to optimize EKF performance?

### 4.2.2 Electrostatic micro-scanner and threshold sensing

The sample device studied in this chapter, shown in Fig. 4.1(a), is an electrostatically-driven dual-axis micro-scanner. It includes two reflective mirror surfaces for dual axes confocal imaging and multiple groups of comb-fingers. Each group of comb-fingers consists of a moveable comb and a fixed comb (Fig. 4.1 (b)). By applying driving voltage with a carefully selected frequency, the comb-finger can generate electrostatic torque that produces parametric resonance in the form of tilting motion with a frequency half that of the driving voltage [62].

This class of micro-scanner is designed to deflect light for imaging purposes [63]. While the comb-fingers are designed to serve as actuators, they can also serve as capacitive sensors to measure the tilting angles of the mirror. The capacitance of the comb-finger as a function of tilting angle [64], is

$$C_s(\theta) = \frac{\epsilon_0 \epsilon_r n A(\theta)}{D} \tag{63}$$

where $\varepsilon_r$ is the relative static permittivity (1 for air), $\varepsilon_0$ is the dielectric constant (8.8542 ×10-12 F m$^{-1}$), $A$ is the overlap area of electrodes, $D$ is the distance between the electrodes, $C_s(\theta)$ is sensing capacitance, $A(\theta)$ is the total area of overlap between the comb-fingers as a function of tilting angle $\theta$, and $n$ is the number of pairs of comb-fingers. The capacitance reaches its maximum when the overlapped area is maximized.

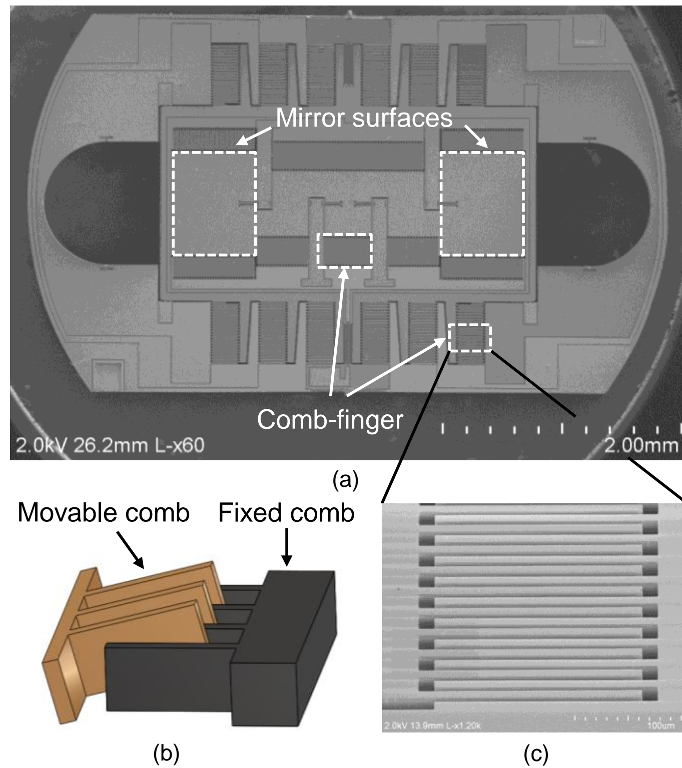


**Fig. 4.1. (a) Scanning electron microscope image of a parametrically-resonant micro-scanner tested in this study. (a) Illustration of comb-finger electrodes used as actuators and capacitive sensors. (b) Zoomed in image of a representative comb-finger structure.**

To transduce the capacitance change into measurable voltage signal, we employ a sensing circuit that applies constant bias voltage, $V_{bias}$ at the sensing electrodes. The change of capacitance can be converted to a sensing current that is amplified by a feedback resistance, $R_s$, and trans-impedance amplifier into an analog voltage signal, $y_{cap}$, by

$$y_{cap} = -R_s V_{bias} \frac{dC_s(\theta)}{dt} \tag{64}$$

It is worth noting that other types of sensing circuits can be applied [34]. Amplitude modulation and demodulation is commonly used to separate and suppress any feedthrough disturbance introduced by parasitic capacitance in the sensing electrodes coupling them to the device's driving voltage. However, modulation/demodulation also generates other effects including delays and skew in the filtered signal, which will can accuracy of a threshold measurement. In this study, since the focus is on validating the concept of generating and extracting threshold angle measurements and evaluating their effectiveness in an EKF framework, the transimpedance approach is used. This realization is also beneficial for implementation using very few electrical interconnects in a compact space, such as an endomicroscope. To compensate for feedthrough, later experiments were performed with a power cut-off strategy, discussed in section IV.

For this device, capacitance reaches its maximum value when the movable comb-fingers cross the mirror's central position and fully overlap the fixed comb-fingers. With the trans-impedance circuit, a rapid change in sign and magnitude

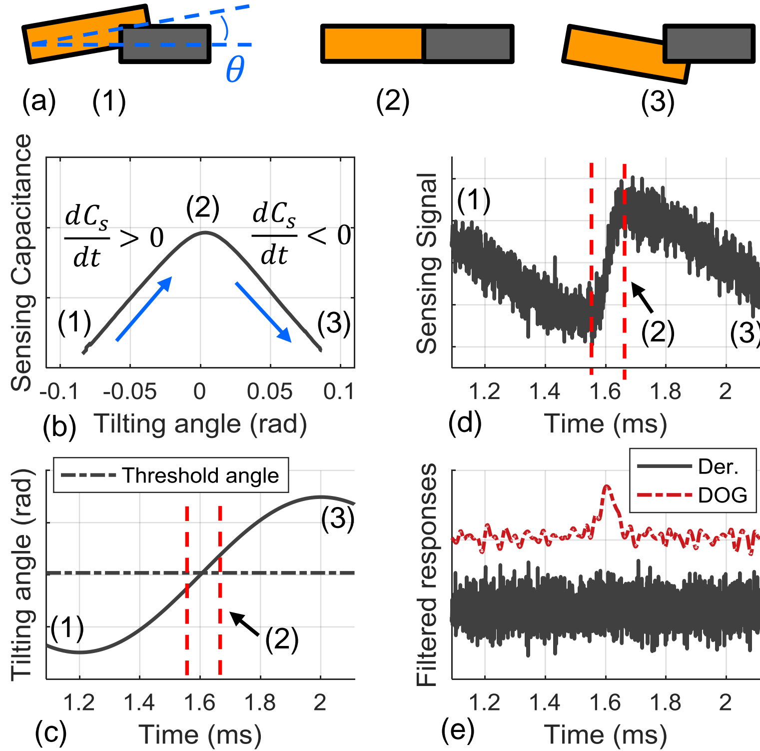


**Fig. 4.2. An illustration of threshold angle crossing and mechanism of threshold angle sensing and detection. (a) Configurations of comb-finger (1), (2) and (3) correspond to before, at, and after threshold angle crossing. (b) Sensing capacitance vs. tilting angle $\boldsymbol{\theta}$. (c) Tilting angle vs. time. (d) Noisy sensing signal vs. time; the crossing event generates rapid change of signal around (2). (e) Comparison of filtered signal by a derivative operator and a DOG operator. DOG operator is effective in detecting the timing of rapid signal change.**

of the output sensing signal occurs, as illustrated in Fig. 4.2 (a-d). This is referred to as the threshold angle for this system.

Knowing the exact timing of the threshold angle crossing is beneficial in high accuracy estimation of the angular position at that time. However, in practice it can be challenging to determine the threshold crossing time from the measured signal due to noise and bias. Since the threshold position crossing corresponds to a locally maximum rate of change of voltage, it might be obvious to adopt a derivative operator as a first attempt to retrieve crossing information. However, as illustrated in Fig. 4.2(e), taking the derivative of a noisy signal does not necessarily provide a reliable outcome. To resolve this issue, a first order derivative of Gaussian (DOG) filter is proposed to extract the timing of the threshold position crossing [32]. A DOG filter is used as an approximated optimal filter for edge detection in the field of computer vision [65] and

has merits of good detection (low probability of false detection), good localization (low variance of detection error), and one response to a single edge (one maxima or minima corresponds to one crossing) [66].

While the introduction of a DOG filter provides an efficient and convenient realization for detecting threshold crossing timing, detection accuracy is still not perfect. In the presence of noise, the detected timing can deviate from the true timing. According to Canny [66], for the detection error in timing for a 1D step edge, $e_{t,th}$, its variance $R_{t,th}$ is expressed as

$$R_{t,th} = E\left[e_{t,th}^2\right] = \frac{\sigma_n^2 \int_{-w}^{w} \dot{f}(\tau)^2 d\tau}{\left[\int_{-w}^{w} \dot{f}(\tau)\dot{y}(-\tau) d\tau\right]^2} \tag{65}$$

where $f(\tau)$ is the filter for edge detection, $y(\tau)$ is the signal including the edge, $\tau$ is a dummy variable, and $\sigma_n$is the standard deviation of the normally distributed, zero mean additive noise to the sensing signal. This expression reveals that $R_{t,th}$ is proportional to the variance of noise (the noisier the signal, the less accurate the detection) and inversely proportional to the edge's slope (the sharper the slope, the more accurate the detection). $R_{t,th}$ is a key factor in threshold sensing performance and can be used to derive the error covariance matrix needed in to obtain optimal state estimates with an EKF.

### 4.2.3 Challenges

To carry out the EKF algorithm using threshold sensing information, a value for $R_{t,th}$ is needed. Although (65) gives a theoretical derivation, in operation, it is difficult to obtain a signal $y(t)$ containing an edge that is uncorrupted by noise. Hence it is desirable to estimate $R_{t,th}$ off-line, which leads to several issues. First, the EKF assumes the process is subject to normally distributed noise. We will investigate the distribution of the $e_{t,th}$, and more importantly, the distribution of detection error of threshold angle, $e_{\theta,th}$, to ensure that the EKF can be

appropriately applied. Second, the expression of $R_{t,th}$ in (65) is derived in continuous time and does not take sampling effects into account. Since the EKF is implemented in discrete time, choice of sampling rate can impact on estimation performance.

4.3 **System modelling**

In this section, the process model, sensor model, and EKF incorporated with threshold sensing are described.

### 4.3.1 Process and sensor model

The dynamics of the tilting motion of the micro-scanner are modeled as a 2nd order, non-linear time invariant system.

$$J\ddot{\theta} + b_v\dot{\theta} + k_s\theta = \tau(\theta, V_{dr}) \tag{66}$$

where $J$ is the moment of inertia of the micro-scanner, $b_v$ is the damping coefficient, and $k_s$ is the spring constant of a torsional spring. The torsional load generated by the comb-finger, $\tau_L$ is:

$$\tau_L(\theta, U) = \frac{1}{2}\frac{dC_{dr}}{d\theta}{V_{dr}}^2 \tag{67}$$

where $V_{dr}$ is the driving voltage, and $C_{dr}$ is the driving capacitance formed by the comb-fingers that generate tilting motion. Let $\boldsymbol{X} = [x_1\ x_2]^T$ to be state vector, where $x_1 = \theta$ and $x_2 = \dot{\theta} = \omega$ is the tilting angular velocity. Letting $\omega_n = \sqrt{k_s/J}$, $\zeta = \frac{b_v}{2\sqrt{Jk_s}}$, where $\omega_n$ is the natural frequency of the tilting mode and $\zeta$ is the damping ratio. (66) becomes:

$$\dot{\boldsymbol{X}} = \begin{bmatrix} 0 & 1 \\ -\omega_n^2 & -2\zeta\omega_n \end{bmatrix}\boldsymbol{X} + \frac{1}{2}\frac{dC_{dr}}{dx_1}{V_{dr}}^2 \tag{68}$$

Denoting the sampling interval to be $T_s$, and assuming that the process is subject to zero-mean, normally distributed process noise, the discretized process model for the EKF becomes

$$\boldsymbol{X}_k = g(\boldsymbol{X_{k-1}}, V_{dr,k}) + \boldsymbol{v_k} \tag{69}$$

where $g(\cdot)$ is defined as:

$$g(\boldsymbol{X_{k-1}}, V_{dr,k}) = \begin{bmatrix} 1 & T_s \\ -\frac{k_s}{J}T_s & 1-\frac{b_v}{J}T_s \end{bmatrix} \boldsymbol{X_{k-1}} + \begin{bmatrix} 0 \\ \frac{T_s}{2J} \end{bmatrix} \frac{dC_{dr}}{dx_1}(k) {V_{dr,k}}^2 \qquad (70)$$

For the sensor model, equation (64) shows that the signal from a capacitive sensor with current-based readout (Fig. 4.4(c)) is proportional to the rate of change of capacitance, $dC_s/dt$. Since $\frac{dC_s}{dt} = \frac{dC_s}{d\theta}\frac{d\theta}{dt}$, where $\frac{dC_s}{d\theta}$ is the rate change of capacitance with respect to tilting angle $\theta$. Denoting $\frac{d\theta}{dt} = \omega$, we have a measurement used by the EKF, $y_{cap}$, of:

$$y_{cap} = \left[-R_s V_{bias}\frac{dC_s}{d\theta}\right]\omega = h_{cap}(\theta)\omega \qquad (71)$$

where $h_{cap}(\theta) = -R_s V_{bias}\frac{dC_s}{d\theta}$ is $\theta$-dependent sensor gain, $R_s$ is a constant resistance, and $V_{bias}$ is a constant bias voltage.

### 4.3.2 Extended Kalman filter with threshold sensing

The proposed EKF includes a hybrid sensing scheme where the signal of the capacitive sensor is regarded as a normal analog measurement, and the detection of threshold crossing is applied intermittently. The procedure for applying the EKF with the fusion of the two types of measurements is illustrated in Fig. 4.3 and described below:

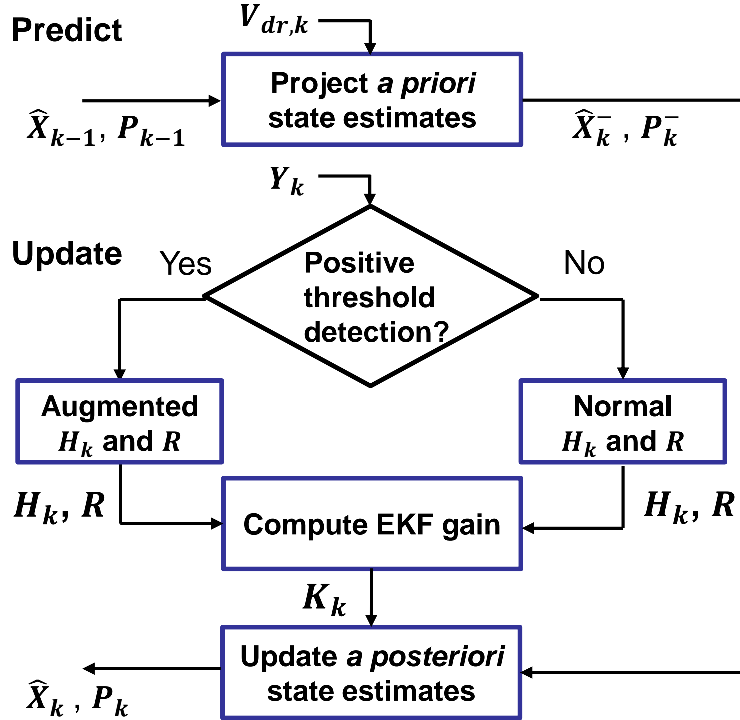


**Fig. 4.3. Schematic depiction of extended Kalman filter synthesizing capacitive sensing and threshold angle measurement.**

The algorithm for applying the EKF with the fusion of the two types of measurements is provided in Table 4.1. In Table 4.1, $\hat{\boldsymbol{X}}_k^-$ is the *a priori* state estimates at the k-th step, $\boldsymbol{P}_k^-$ is the *a priori* error covariance matrix at the $k$-th step, $\boldsymbol{P}_{k-1}$ is the *a posteriori* error covariance matrix at the $(k-1)$-th step, $\boldsymbol{Q}$ is the covariance matrix of process noise, and $\boldsymbol{G}_k = \frac{\partial g}{\partial X_{k-1}}$ is the Jacobian of the process model.

Depending on whether a threshold detection is positive, the form of the matrix of observation, $\boldsymbol{H}_k$, the estimated sensing signal, $\hat{Y}_k$ and the covariance matrix of measurement noise, $\boldsymbol{R}$, will vary. $R_{cap}$ is the measurement noise variance for the analog capacitance signal and $R_{\theta,th}$ is the variance of $e_{\theta,th}$. The Kalman gain $\boldsymbol{K}_k$ is then computed and *a posteriori* state estimates $\hat{\boldsymbol{X}}_k$ and *a posteriori* estimate error covariance matrix $P_k$ are finally updated with the measurement at the $k$-th step, $Y_k$. Measurement $\boldsymbol{Y}_k = [\theta_{th} \quad y_{cap,k}]^T$ for positive detection and $\boldsymbol{Y}_k = y_{cap,k}$ for negative detection.

**Table 4.1 Algorithm, EKF with Hybrid Sensing Scheme**

1. Project *a priori* state estimates

$$\widehat{\boldsymbol{X}}_k^- = g(\widehat{\boldsymbol{X}}_{k-1}, V_{dr,k}); \quad \boldsymbol{P_k^-} = \boldsymbol{G_k P_{k-1} G_k^T} + \boldsymbol{Q}$$

2. Update matrix of observation

If threshold detection is negative

$$\widehat{\boldsymbol{Y}}_{\boldsymbol{k}} = [0 \; h_{cap}(\hat{\theta}_k^-)]\widehat{\boldsymbol{X}}_k^- = \boldsymbol{H_k}\widehat{\boldsymbol{X}}_k^-; \quad \boldsymbol{R} = R_{cap}$$

If threshold detection is positive

$$\widehat{\boldsymbol{Y}}_k = \begin{bmatrix} 1 & 0 \\ 0 & h_{cap}(\hat{\theta}_k^-) \end{bmatrix} \widehat{\boldsymbol{X}}_k^- = \boldsymbol{H_k}\widehat{\boldsymbol{X}}_k^-; \quad \boldsymbol{R} = \begin{bmatrix} R_{\theta,th} & 0 \\ 0 & R_{cap} \end{bmatrix}$$

3. Compute EKF gain with threshold sensing

$$\mathrm{K_k} = \mathbf{P_k^- H_k^T}\left(\mathbf{H_k P_k^- H_k^T} + \mathbf{R}\right)^{-1}$$

4. Update *a posteriori* state estimates

$$\widehat{\boldsymbol{X}}_{\boldsymbol{k}} = \widehat{\boldsymbol{X}}_{\boldsymbol{k}}^- + \boldsymbol{K_k}\left(\boldsymbol{Y_k} - \widehat{\boldsymbol{Y}}_{\boldsymbol{k}}\right); \quad \boldsymbol{P_k} = \boldsymbol{P_k^-} - \boldsymbol{K_k H_k^T P_k^-}$$

## 4.4 **Experiments and model identification**

An experimental testbed was prepared and used to identify parameters of the process and sensor models, and to verify the effectiveness of the DOG filter in threshold crossing detection and the EKF using the hybrid sensing scheme.

### 4.4.1 Experimental set-up and methods

As depicted in Fig. 4.4(a), computer-generated voltage commands were transmitted to an NI PCIe 6251 DAQ with sampling rate of 500 kHz. The voltage command was amplified by a TEGAM 2340 amplifier with 20 times amplification, and the amplified driving voltage fed to the MEMS scanner to generate tilting motions. Tilting motion was measured by two means: reflection of a laser by the scanner and conversion of the capacitive sensing current as described in (71).

Laser tracking is treated as the ground truth of tilting motion. Fig. 4.4(b) shows the geometric relation between the MEMS scanner mounted on a dual inline package, a JDSU 1500 helium-neon laser source, and an On-Trak 1L10 position sensing detector (PSD). The laser beam is emitted by the source, reflected by the scanner's mirror surface, and received by the PSD, amplified by an On-Trak-301SL sensing amplifier.

On-chip sensing is used by the EKF. Fig. 4.4(c) depicts the schematic of integrated driving and sensing circuitry. An AC driving voltage is fed into comb-fingers used for driving, and a DC bias voltage provided by a source meter, $V_{bias}$, is fed into comb-fingers used for sensing. The generated current flow through the shared grounding terminal is fed into a sensing circuit, which consists of a TI OPA2140 amplifier with a feedback resistance of 10 Mohm.

Since the objective of the study is to validate the method of using a DOG filter for threshold angle crossing detection and EKF integration, it is useful to eliminate potential disturbances introduced by feedthrough of the driving voltage. Therefore, during experiments, a power cut-off method was applied.

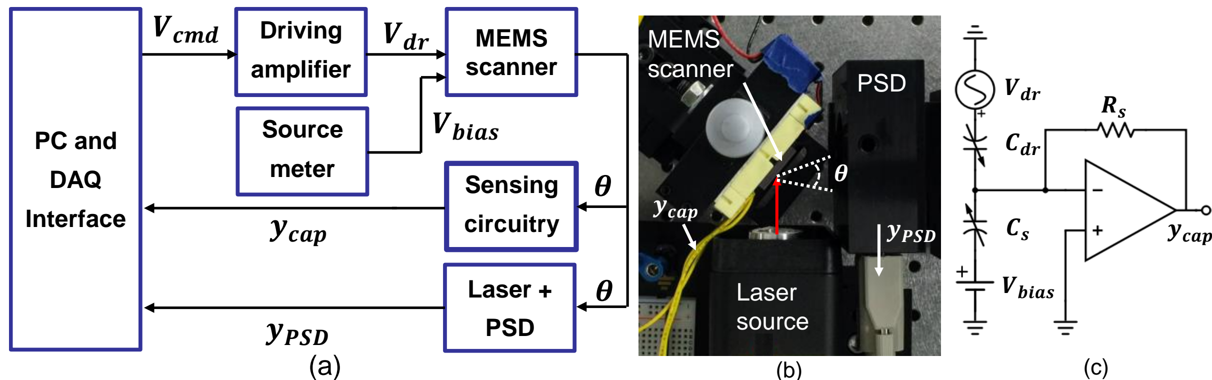


**Fig. 4.4. Experimental set-up: (a) Schematic of major experimental modules and signal flow. (b) Top view of set-up and illustration of geometric relationship between the laser source, MEMS scanner and PSD. (c) Schematic sensing and driving circuitry for the MEMS scanner.**

A zero to 60 volt periodic $V_{dr}$ was applied to the MEMS scanner, and the frequency was swept from 1600 Hz to 1220 Hz to reach a maximized amplitude of tilting motion given electrostatic

spring softening [21]. Once the tilting motion was stabilized, $V_{dr}$was set to zero, while $V_{bias}$ was maintained at a constant 10 volts. Such a sequence of voltage commands allows the micro-scanner to freely oscillate briefly after the power cut-off, and the sensing current induced by the oscillation can be amplified and recorded without feedthrough disturbance.

A total 10 trials of power cut-off experiments were performed and the $V_{dr}$, $y_{cap}$ and $y_{PSD}$were recorded at 500 kHz rate. The data was post-processed as follows for consistency: Each time series was truncated at the power cut-off and 80 ms afterwards (approximately 50 periods of free oscillation). The delay between PSD measurement and sensing circuit measurement was experimentally calibrated to be 0.114 ms.

To detect a threshold crossing, a DOG filter is applied to the sensing signal using the *nlfilter* function in MATLAB, which is a general sliding-neighborhood operation. The filtered signal is then processed with non-maximum suppression to suppress the filtered response except the local maxima, and these local maxima are then extracted to indicate the detected threshold crossing. In this study, the threshold detections are extracted in a post-processing fashion. To achieve a near real-time threshold detection, a buffer can be used to store measurements from past to present, and DOG filter can be applied to the signal in the buffer to generate a local maximum for threshold detection.

### 4.4.2 Identification of process and sensor models

The tilting angle measured by the PSD, $\theta_{PSD}$ is computed as

$$\theta_{PSD} = \arctan(\frac{y_{PSD}G_{PSD}}{L_m}) \tag{72}$$

where $G_{PSD}$(0.5 mm/V) is the gain of the PSD sensing amplifier and $L_m$ is the distance from the scanner surface to PSD surface

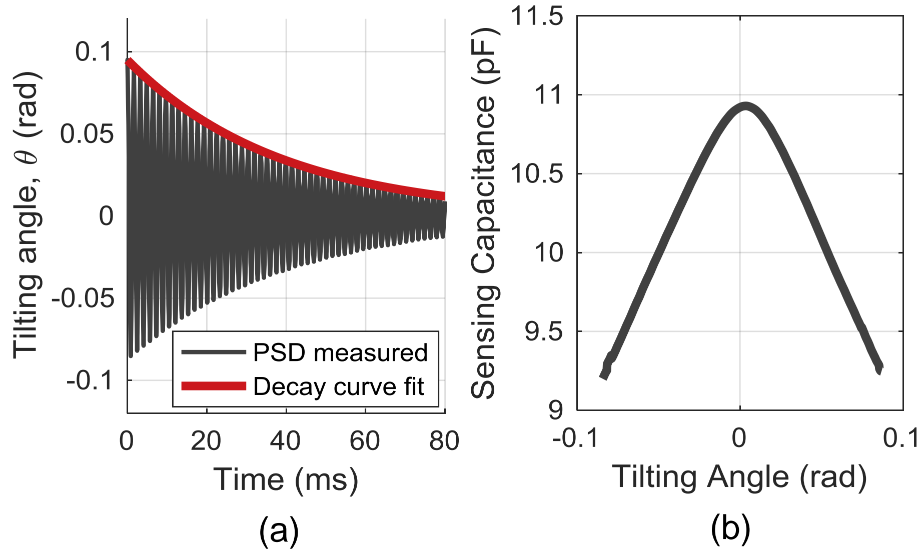


**Fig. 4.5. (a) Experimentally measured free oscillations vs. simulated decay curve of free oscillations with identified natural frequency and damping ratio of the MEMS scanner. (b) Experimentally identified sensing capacitance with respect to tilting angle.**

**Table 4.2 Baseline setting for parametric Study**

| Symbol | Description | Value |
|---|---|---|
| $f_s$ | Sampling frequency | 500 kHz |
| $\theta_{amp}$ | Amplitude of $\theta$ | 0.15 rad |
| $f_m$ | Motion frequency | 625 Hz |
| $\sigma_n$ | Standard deviation of noise | 0.0435 V |
| $R_s$ | Feedback resistance | 10 MΩ |
| $V_{bias}$ | Bias voltage | 10 V |
| $w_{DOG}$ | Width of DOG filter | 400 |
| $\sigma_{DOG}$ | Standard deviation of DOG filter | 15 |

and is measured to be 32.7 mm. A representative trajectory of the system is shown Fig. 4.5 (a); by fitting the decay curve using linear viscous damping [67], $\omega_n$ and $\zeta$ were identified to be 624.6 Hz and 0.0066, respectively.

The sensor model is the sensing capacitance as a non-linear function of angle, $C_s(\theta)$, which can be experimentally identified by mapping the trajectory $C_s(t)$ versus $\theta_{PSD}(t)$ in various experiments. First, $C_s(t)$ is obtained by integrating $y_{cap}$ with respect to time, from (64):

$$C_s(t) = \int_{t_0}^{t_f} -R_s V_{bias} y_{cap} dt \tag{73}$$

Using the corresponding $\theta_{PSD}(t)$ one can establish a mapping of $C_s(\theta)$ and $\frac{dC_s}{d\theta}(\theta)$ and therefore compute $h_{cap}(\theta)$as suggested in (71). Fig. 4.5 (b) shows the identified sensor gain function $h_{cap}(\theta)$. The capacitance profile can be approximated by a Gaussian model [64].

The threshold location, $\theta_{th}$ is identified by computing the average angular displacement at which the peak capacitance is reached among the experimental measurements. Nominally, $\theta_{th}$ should be zero for the planar micro-scanner geometry, but in practice a non-zero value may occur due to finite fabrication tolerance of electrodes and residual stresses. In this device $\theta_{th}$ was calibrated to be 0.0037 rad.

## 4.5 **Parametric study of factors impacting threshold detection**

In this section, parametric studies investigate the properties of the error of threshold detection and some contributing factors, including the sensor map and sampling rate. A sinusoidal tilting motion is simulated within the capacitive sensor model described by (71), with additive, zero-mean normally distributed measurement noise. The signal generated by the capacitive sensing model is passed into a DOG filter to compute the detection error in timing $e_{t,th}$ and detection error in threshold angle $e_{\theta,th}$. Baseline settings from experimental device identification are summarized in Table 4.2.

### 4.5.1 Sampling rate effects

In (3), sampling rate is not singled out as a factor that affects the detection of threshold signal. However, this is not the case during digital implementation, as a low sampling rate introduces quantization error and a high sampling rate may allow excessive sensor noise into the filtering process. Therefore a series of simulations was conducted, from the baseline in Table 4.2,

and the sampling rate was swept from 50 kHz to 5 MHz. The filter size was adjusted proportionally to maintain a fixed ratio between the filter size and the period of the waveform. The signal-to-noise ratio (SNR) was also varied by multiplying $\sigma_n$ by factors of 0.1 and 10.

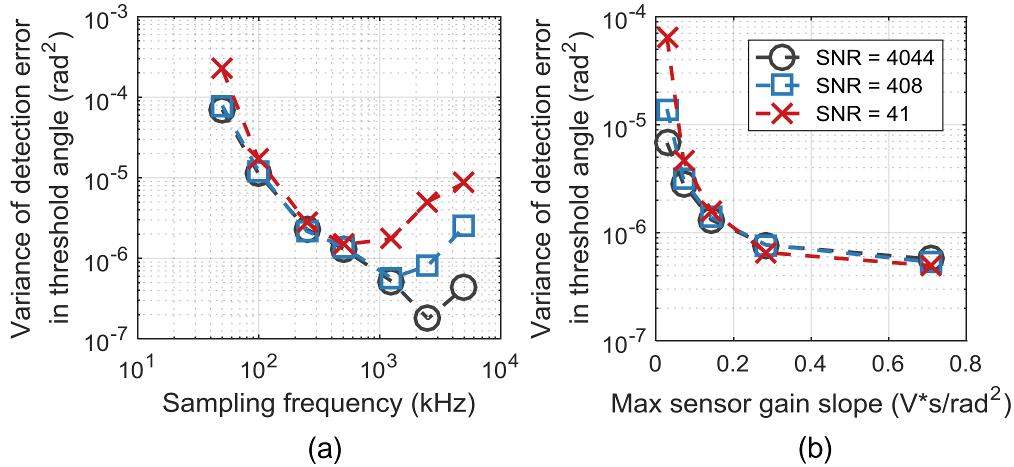


**Fig. 4.6. (a) Variance of detection error in threshold angle vs. sampling frequency. (b) Variance of detection error in threshold angle vs. maximum sensor gain slope.**

The simulation result is shown in Fig. 4.6(a). The result shows that $R_{t,th}$ increases as sampling rate is slower than 1250 kHz, mainly due to quantization noise. As the sampling rate increases, $R_{t,th}$ increases, attributed to noisier samples being taken into the filtering process. This suggest that an optimal selection for sampling frequency for a given threshold sensor exists, and one can properly size the data acquisition system to achieve the lowest variance of detection timing error without overreaching for fast sampling capability.

### 4.5.2 Sensor map effects

Equation ( 65 ) suggests that the variance of detection timing error is inversely proportional to the rate of change of the signal $\dot{y}(t)$, meaning that a sharper and more abrupt change of signal amplitude can be more accurately located in a statistical sense. To test the significance of the change, one way is to change of the capacitance profile formed by the electrodes. More specifically, we are interested in $dC_s/d\theta$ around threshold location, as higher

values will prompt higher $\dot{y}_{cap}(t)$ as suggested in (71). In this study, a modified logistic function is used to generate a modelled sensor gain, $\hat{h}_{cap}$ as:

$$\hat{h}_{cap}(\theta) = N_g(\frac{1}{1+e^{-N_\theta \theta}} - 0.5) \quad (74)$$

where $N_g$ is the normalization factor for gain, and $N_\theta$ is the normalization factor for angle.

The modelled sensing capacitance simply takes the integration of $\hat{h}_{cap}(\theta)$ with respect to tilting angle:

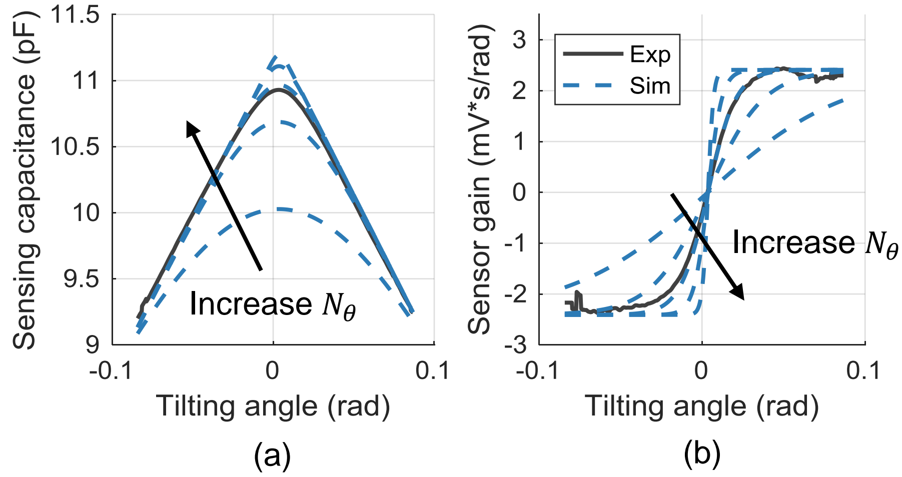


**Fig. 4.7. Sweep of maximum sensor gain slope. (a) Sensing capacitance becomes sharper around threshold angle as $N_\theta$ increase. (b) Sensor gain slope becomes steeper around threshold angle as $N_\theta$ increases.**

$$\hat{C}_s(\theta) = -\frac{1}{R_s V_{bias}} \int_{\theta_{min}}^{\theta_{max}} \hat{h}_{cap}(\theta)\, d\theta \quad (75)$$

By sweeping $N_\theta$ one can vary the maximum sensor gain at the vicinity of threshold location, with larger $N_\theta$ corresponding to steeper slop and more drastic change of capacitance at $\theta_{th}$, as depicted depicted in Fig. 4.7. The experimentally identified sensor gain was used as a baseline to generate a series of sensor model with $N_\theta$ swept from 0.2 to 5. Fig. 4.6 (b) shows corresponding simulation results. We find that $R_{t,th}$ decreases as expected as the maximum sensor gain slope increases. The significance of this change is comparable at various sensor noise densities.

## 4.6 **Experimental results and discussion**

In this section, experimental results are presented to evaluate the effect of different DOG filters on threshold detection and EKF performance. The decaying tilting motion of the micro-scanner after power cut-off provides an opportunity to vary SNR by segmenting trajectories. Therefore, for each trial the measurements and estimated states are divided into 4 segments, with SNR ranging from 85 to 1. For conciseness, the EKF using the hybrid sensing scheme of capacitive analog sensing and threshold sensing is abbreviated as HYB.

### 4.6.1 Effect of DOG filter on threshold detection

The EKF implementation assumes that process noise and measurement noise are normally distributed. Therefore, it is helpful to verify the distribution of measurement noise of the threshold sensor. Threshold angle measurement noise is defined as the error between the threshold angle and the ground truth angle at the instant of detection, denoted as $e_{\theta,th}$. Here, $e_{t,th}$ and $e_{\theta,th}$ are computed by taking the differences between the timing and angle at the detected threshold crossing and their ground truth values, respectively.

Fig. 4.8 shows a representative distribution of $e_{\theta,th}$ with sampling condition of 2.5 MHz. These results suggest that with noisy sensor measurements, varying sampling rate only affects the mean and variance of the error of threshold angle

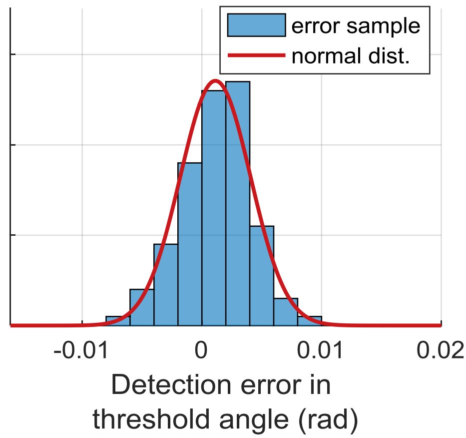


**Fig. 4.8. Comparison between the sampled error of threshold angle detections and normal distribution with corresponding mean and variance.**

The distribution of $e_{t,th}$ and $e_{\theta,th}$ computed from experimental measurements was analyzed using the Kolmogorov-Smirnov test [68]. Results indicate that the error distribution can be well-modeled by normal distributions at the tested conditions, shown in Fig. 4.9.

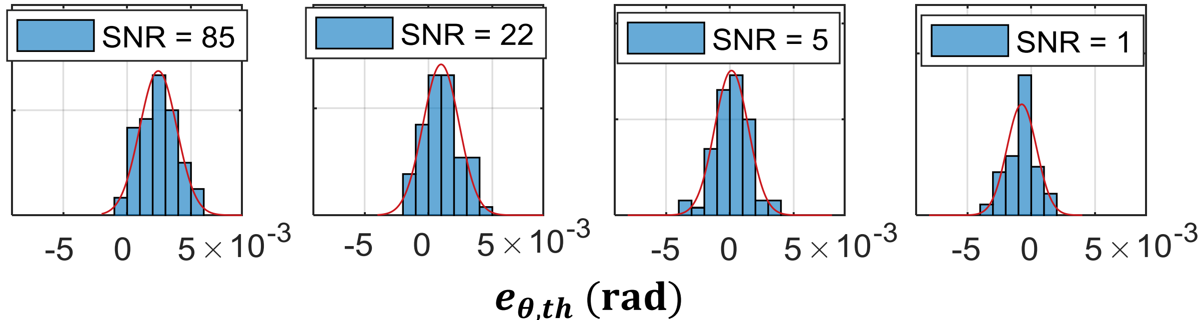


**Fig. 4.9. Distribution of detection errors in threshold angle from experimental measurements at different signal-to-noise ratios can be well modeled by normal distributions.**

Different settings for the DOG filter were also applied to $y_{cap}$ and the EKF to evaluate itheir impact on the variance of $e_{\theta,th}$and accuracy of state estimation. The filter size $w_{DOG}$ was swept from 80 sample points to 400 sample points and $\sigma_{DOG}$ was swept from 1.5 to 45. No significant performance variation was found in varying $w_{DOG}$ while keeping $\sigma_{DOG}$ the same. However, as shown in Fig. 4.11, the variance of $e_{\theta,th}$ varies as $\sigma_{DOG}$ varies for all four cases, which suggests a large $\sigma_{DOG}$ is beneficial in reducing overall error variance.

### 4.6.2 Effect of threshold sensing on EKF

A representative estimation result is depicted in Fig. 4.10. The ground truth (EXP) and estimated tilting motion (EKF and HYB) are shown. Fig. 4.10 (a) shows the change in estimator output with introduction of threshold crossing detection: $\hat{\theta}$ by HYB is corrected at the instant of threshold crossing detection and therefore is closer to the ground truth value. Fig. 4.10 (d) shows that the local maxima of the DOG filter response corresponds to the vicinity of the maximal rate of change of $y_{cap}$ and serves as a detection of threshold angle crossing. The four snapshots demonstrate that the detection method is robust under various SNR conditions.

Root mean square error (RMSE) of tilting angle $\theta_{RMSE}$ is defined as a performance metric:

$$\theta_{RMSE} = \sqrt{\frac{1}{N}\sum_{i=1}^{N}\left(\hat{\theta}_i - \theta_{PSD,i}\right)^2} \tag{76}$$

where $\hat{\theta_i}$ is *a posteriori* estimate of tilting angle and $\theta_{PSD,i}$ is the tilting angle measured by the PSD at the $i$-th sampling instance, and $N$ is the number of sampling instants. A normalized root mean square error (NRMSE) of tilting angle, $\theta_{NRMSE}$ is also defined and examined:

$$\theta_{NRMSE} = \frac{\theta_{RMSE}}{\bar{\theta}_{amp}} \tag{77}$$

where $\bar{\theta}_{amp}$ is the average amplitude of the corresponding waveforms. $\theta_{RMSE}$ and $\theta_{NRMSE}$ are evaluated for the overall trajectories as well as each segment.

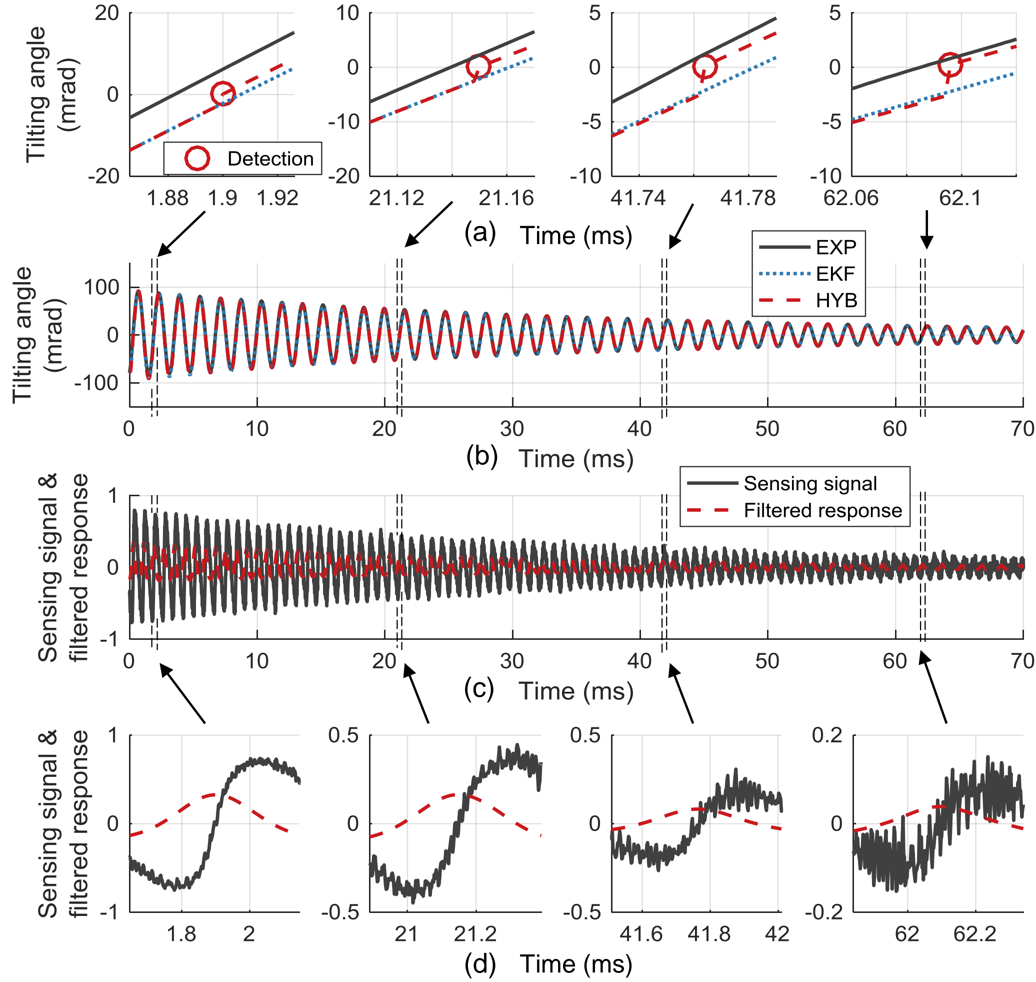


**Fig. 4.10. A representative experimental measurement and estimation result in time domain. (a) Four snapshots of threshold angle crossing detection improving tilting angle estimation. (b) Overall trajectories of tilting angle measurement and estimations. (c);Overall trajectories of sensing signal and response of DOG filter. (d) Corresponding snapshots of sensing signal, where local maxima of filtered response detects threshold angle crossing.**

To evaluate the improvement made by introducing threshold sensing to the EKF, the $\theta_{RMSE}$ within each segment of estimation trajectory generated by the two estimators are computed. Here $\theta_{RMSE,th}$ denotes the RMSE computed using 50 sample points after each threshold detection occurred. The results are listed in Table 4.3.

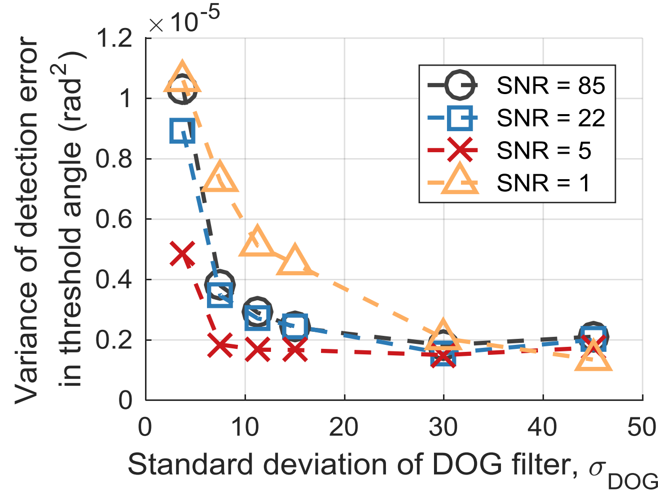


**Fig. 4.11. Variance of detection error in threshold angle during experiments with respect to the standard deviation of DOG filter.**

**Table 4.3 Summary of RMSE of estimated tilting angle**

| | **SNR 85** | **SNR 22** | **SNR 5** | **SNR 1** | **Overall** |
|---|---|---|---|---|---|
| EKF $\theta_{RMSE}$ | 0.0050 | 0.0029 | 0.0026 | 0.0025 | 0.0034 |
| HYB $\theta_{RMSE}$ | 0.0047 | 0.0023 | 0.0019 | 0.0018 | 0.0029 |
| $\boldsymbol{\theta_{RMSE}}$ **reduce** | **6.9%** | **21.4%** | **27.6%** | **30.3%** | **15.1%** |
| EKF $\theta_{RMSE,th}$ | 0.0055 | 0.0051 | 0.0050 | 0.0049 | 0.0051 |
| HYB $\theta_{RMSE,th}$ | 0.0041 | 0.0045 | 0.0049 | 0.0045 | 0.0045 |
| $\boldsymbol{\theta_{RME,th}}$ **reduce** | **26.0%** | **11.6%** | **2.6%** | **8.1%** | **12.3%** |

From Table 4.3, we can see that the largest percentage improvement of total RMSE happens with SNR = 1. The largest improvement of RMSE after threshold detection location happens with SNR = 85. The result shows that the threshold sensing adds the greatest local accuracy in high SNR conditions, but is more beneficial for overall EKF performance when SNR is low.

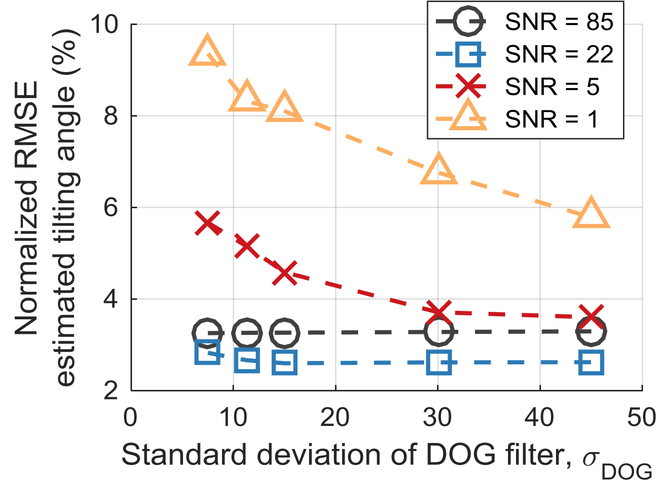


**Fig. 4.12. Normalized RMSE with different signal-to-noise ratios and various $\sigma_{DOG}$settings. Under noisy condition (low SNR), increasing $\sigma_{DoG}$ effectively increases threshold detection accuracy and therefore increases state estimation accuracy of the EKF.**

The trend of $\theta_{NRMSE}$ of each segment with respect to different $\sigma_{DOG}$is shown in Fig. 4.12. For segments with high SNR (85 and 22), the change of $\sigma_{DOG}$ does not significantly change $\theta_{NRMSE}$. However, for segments with low SNR (5 and 1), the analysis shows increasing $\sigma_{DOG}$ significantly reduces $\theta_{NRMSE}$, which suggests that the performance of EKF with threshold sensing is sensitive to selection of $\sigma_{DOG}$.

## 4.7 **Chapter summary**

In this chapter, we presented a principle of threshold position sensing to indicate crossing of pre-determined threshold position that is relatively robust to geometric perturbations in non-monotonic capacitance profile, which can be used to improve its measurement accuracy for the associated threshold positions or angles, and therefore improve the overall performance of the sensor or estimator using such sensor.

We introduce a method for utilizing a first order derivative of Gaussian (DOG) operator to detect threshold crossing from noisy signal and integrated this detection mechanism into an EKF to estimate states from a non-linear process. To verify the effectiveness of the method,

experimental and simulation studies have been conducted to estimate the tilting angle of an electrostatic micro-scanner and quantify various factors that might affect the error of threshold detection and EKF performance. Simulation shows: (1) an optimal sampling frequency exists for a minimal variance of detection timing error; (2) increasing $G_{cap}(\theta)$ around threshold angle reduces variance of detection error in timing and angle, beneficial for improving EKF accuracy.

Experimental results show that use of the threshold sensing mechanism improved EKF performance across SNR conditions on a MEMS micro-scanner, with best improvement of a 30.3% reduction in RMSE of tilting angle estimation. On average, using threshold sensing improves the RMSE by 15.1% across a range of SNR scenarios. A sweep of width $\sigma_{DOG}$ of the DOG filter also shows that for low SNR, threshold detection accuracy is more sensitive to DOG filter parameter such as $\sigma_{DOG}$ and therefore needs to be selected carefully to so that EKF can maximize the performance improvement of using the DOG filter.

# Chapter 5
## Motion Estimation with Shared Electrodes for Driving and Sensing

### 5.1 Chapter overview

In this last case study in this dissertation, a method to estimate tilting motion of an electrostatic micro-scanner used for laser scanning in endomicroscopy is presented, with size constraints requiring use of the same electrodes for both actuation and sensing. The estimated amplitude and phase shift will be the focus of evaluating estimator performance, as these can be helpful to reduce the blur and distortion of image reconstruction given perturbations to scanning mirror dynamics over time. To overcome the limitation that no dedicated sensing electrodes are available, the method adopts an amplitude modulation-demodulation (AMDM) circuit design customized for the mirror to separate feedthrough generated by the high driving voltage. A process model based on non-linear parametric resonant dynamics of the micro-scanner and a sensor model including a large angle Gaussian based capacitance model and a sensing circuit model are derived and parameters are identified with experimental measurements. An extended Kalman filter (EKF) and an unscented Kalman filter (UKF) are implemented to incorporate the process model and sensor model to provide high-accuracy motion estimation. Experimental results show that the UKF achieved 0.39 degree root-mean-square error (RMSE) in estimated mirror phase delay, significantly improving on EKF performance.

The chapter is organized as following: Chapter 5.3 describes the method, including process modeling, sensor modeling and circuit analysis, Chapter 5.4 describes the experiments

setup and procedures, Chapter 5.5 presents results including the identified process and sensor model, and performance evaluation of EKF and UKF. Finally, a summary is provided in Chapter 5.6.

## 5.2 **Background and motivation**

To elaborate on optical imaging applications first introduced in Chapter 4, with the continuing development of micro-electro-mechanical system (MEMS) technology, MEMS scanners have been used in an array of applications involving laser scanning and displays [21]. One interesting application is to use MEMS scanners in endomicroscope devices [69], such as a confocal endomicroscopes [70] or multiphoton endomicroscopes [71]. Conventional confocal and multiphoton microscopes are based on laser scanning with galvanometers, which consist of a motor and mirror with position feedback to provide high speed laser scanning [72]. However, the size of galvanometers (on the scale of centimeters) limits their usefulness in endoscopic instruments, and MEMS scanners are instead proposed as miniature actuators with reflective mirror surfaces to perform laser scanning.

MEMS scanners can be classified by their actuation principles into four main categories: electrostatic, electromagnetic, piezoelectric and electrothermal. Among these categories, the electrostatic micro-scanner uses the attractive forces generated by two oppositely charged plates or electrodes as the actuation force to rotate a mirror for directional laser scanning. Electrostatic actuators have advantages of comparatively straightforward fabrication and integration into microscopy systems, and therefore comprise the majority of endomicroscope scanners in the literature [21]. For large field-of-view with high resolution, these scanners must achieve large deflection angles, and therefore are usually designed to have high quality factor and be operated at or near their resonant frequencies [73]. As a result, this type of scanner suffers from resonance

shift due to material property variation (density, thermal expansion, Poisson's ratio and elastic constants) and thermal expansion mismatch (due to usage of multilayer structures consisting of different materials) caused by temperature perturbation [28]. In the absence of feedback, resonance shift will introduce error in phase and amplitude information to be used in the image reconstruction process. Incorrect phase information will lead to blurred images due to misplaced pixels while incorrect amplitude information will lead to distorted images. One solution is to provide state estimation for accurate phase and amplitude measurement from the motion of the scanner during operation using on-chip sensing. Image reconstruction can then be adapted accordingly. Knowing dynamic state trajectories during scanner motion can also be helpful for device health monitoring and fault detection.

Previous works have combined electrostatic actuation with on-chip sensors, in some cases by other sensing mechanisms including piezoresistive sensing [74] and piezoelectric sensing [19] [75]. More commonly, capacitive sensing is used with electrostatic actuation, given its advantages for ease of design, fabrication, and integration alongside electrostatic driving electrodes. For example, Hofmann et al. presented a high-Q electrostatic resonator device using dedicated capacitive sensing comb electrodes to provide phase feedback [73]. However, all of these designs require extra space on-chip and increase the number of electric interconnects needed between the instrument and control circuitry, both of which are difficult to accommodate in small endomicroscopy instruments (2.4 – 5 mm) [69]. Meanwhile, compact chips experience significant feedthrough disturbance between driving voltage inputs and sensor outputs due to parasitic capacitances in all of the above sensing schemes. Therefore, it is desirable to use the same capacitors for both actuation and sensing purpose, but this further increases feedthrough effects.

Hung et al. [76] have recently presented a bi-axial micro-scanner with electrostatic actuation and sensing using the same capacitor. The sensing signal was used in a phase-locked loop to ensure that the device would consistently be operated at resonance of its fast axis. A closed-loop controller for the scanner's slow axis was demonstrated subsequently [77]. However, those works did not provide continuous fast axis motion tracking, and did not integrate knowledge of actuator dynamics, capacitance profile with respect to position, and sensing circuit behavior to permit state estimation across the full range of tilting motion.

More advanced filtering and estimation techniques to account for some of the above phenomena have been demonstrated in certain similar prior applications. A parallel plate configuration for a capacitive sensor was designed to provide on-chip sensing for out-of-plane tilting motion of a MEMS device, with feedthrough in the signal eliminated by taking the difference of sensing signals from repetitive measurements with and without bias voltages [51, 59]. In [29] [78], a sensing scheme with an extended Kalman filter (EKF) that used unique nonlinear features of electrodes to detect threshold events for improved angular position was demonstrated, but with feedthrough eliminated by purposely interrupting the device's driving voltage during sensor use. Those methods either require that driving commands be strictly repeated or intermittently set to zero, and therefore are difficult be applied with closed-loop feedback control.

This study aims to provide high-accuracy motion tracking from an endoscopic micro-scanner with shared sensing and driving electrodes by introducing several new elements to state estimator models and design for MEMS scanners. The method is based on a dedicated amplitude modulate and demodulation (AMDM) circuit designed to extract meaningful sensing signal in the presence of feedthrough generated by the scanner's input voltage. Extending upon existing

frequency separation assumptions for AMDM capacitive sensing schemes, frequency separation analysis is conducted in the presence of nonlinear mirror and sensor dynamics, such as large deflection capacitance and envelope detection effects. A process model is incorporated based on parametrically resonant scanner dynamics. The effectiveness of feedthrough rejection is then analyzed based on these nonlinear effects. An extended Kalman filter and an unscented Kalman filter are used to incorporate the non-linear actuation and measurement models into state estimation, and their performance is compared. The resulting estimation scheme provides the most complete solution for electrostatic micro-scanner motion tracking in endomicroscopic laser-scanning applications yet reported.

## 5.3 **Methods**

### 5.3.1 Target accuracy of phase shift estimation

A target for estimation accuracy of phase shift tracking has been developed and is described below. Since the goal of the motion estimation for a scanner is to improve image registration, the resolution of the timing of a pixel is determined by the sampling frequency of the imaging system. Let $f_s$ denote the sampling rate of image registration; the resolution of timing information, $\delta t$ can then be expressed as:

$$\delta t = \frac{\alpha}{f_s} \tag{78}$$

where $\alpha$ is a integer number used to control resolution of timing as multiples of sampling interval. Let $f_{res}$ to be the mechanical resonant frequency of the scanner, then the phase shift error, $\delta\phi$, can be converted to

$$\delta\phi = \frac{\delta t}{1/f_{res}} = \alpha \frac{f_{res}}{f_s} \tag{79}$$

In this study, we chose $\alpha$ to be 2 to represent the resolution of 2 sampling instants, and $f_s$ to be 10 MHz based on the DAQ sampling capability and $f_{res}$ to be 15.5 kHz for the selected device. Therefore, the target phase shift estimation accuracy is computed to be 0.18 degrees of phase angle.

### 5.3.2 System dynamics and process model

The electrostatic micro-scanner studied in this study is a dual axis micro-scanner, shown in Fig. 5.1. The multiple groups of comb-fingers are incorporated to generate electrostatic force and rotate the scanner with external voltage excitation. To minimize voltage requirements and external connections, all stator comb fingers are connected to the same voltage source, and all rotor (mirror) fingers are connected to ground. As a planar structure, out-of-plane motion (whether translation or rotation) is not generated at all frequencies, but only near integer multiples of the natural frequency of free vibration, via parametric resonance.

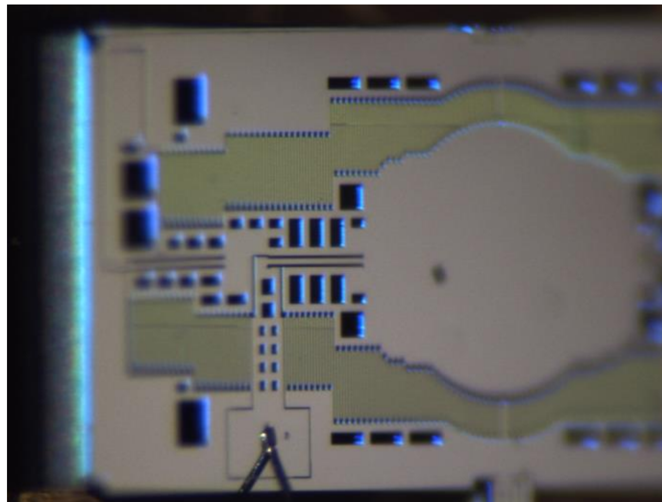

**Fig. 5.1. Dual axis electrostatic micro-scanner studied in this chapter. The electrodes are shared for both driving and sensing purpose.**

The governing equation of the torsional force acting on the mirror structure is characterized as:

$$T(t) = \frac{1}{2}\frac{dC_s(t)}{d\theta}V(t)^2 \tag{80}$$

where $C_s$ is the total capacitance formed by the comb-fingers, $\theta$ is the tilting angle of the micro-scanner and $V$ is the driving voltage. The equation of motion is described as:

$$J\ddot{\theta} + b\dot{\theta} + k\theta = \frac{1}{2}\frac{dC_s(t)}{d\theta}V(t)^2 \tag{81}$$

where $J$ is the moment of inertia of rotation, $b$ is damping coefficient, and $k$ is the torsional spring constant of the device. Defining states $x_1 = \theta$ and $x_2 = \dot{\theta}$, defining $C_s' = \frac{dC_s}{d\theta}$, and denoting the sampling interval as $T_s$, (79) then can be discretized with a first order Taylor expansion as:

$$\begin{bmatrix} x_{1,k} \\ x_{2,k} \end{bmatrix} = \begin{bmatrix} x_{1,k-1} + T_s x_{2,k-1} \\ -\frac{T_s k^2}{J^2} x_{1,k-1} + \left(1 - \frac{T_s b}{J}\right) x_{2,k-1} + \frac{T_s C_k'}{2J} V_k^2 \end{bmatrix} \tag{82}$$

where the subscript $k$ stands for $k$-th sampling instance in the discretized time domain. Assuming the process is corrupted by additive zero mean, normally distributed process noise $\boldsymbol{w_k}$, and $\boldsymbol{X_k} = [x_{1,k} \quad x_{2,k}]^T$, (82) can be represented as

$$\boldsymbol{X_k} = g(\boldsymbol{X_{k-1}}, V_k) + \boldsymbol{w_k} \tag{83}$$

The covariance matrix of $w_k$ is denoted as $\boldsymbol{Q}$, and $\boldsymbol{Q}$ is computed as

$$\boldsymbol{Q} = Q_\theta \begin{bmatrix} \frac{1}{4}T_s^4 & \frac{1}{2}T_s^3 \\ \frac{1}{2}T_s^3 & T_s^2 \end{bmatrix} \tag{84}$$

where $Q_\theta$ is the noise variance of angular position.

### 5.3.3 Sensing principle and measurement model

Since $C_s$ is a function of $\theta$, the same comb-fingers used to produce electrostatic force for actuation can be used as position sensors. In this study, we use an AMDM circuit to provide amplitude modulated voltage to both drive the electrostatic mirror at its resonant frequency and

to demodulate the sensing current to measure the tilting motion of the device. Use of AMDM techniques to implement capacitive sensing is common, and has been applied to use of a single driving/sensing channel in the past. However, several aspects of the micro-scanner application here present particular challenges. These include a nonlinear capacitance function, relatively close spacing of driving and sensing frequencies due to the fast mirror response, limited transmission bandwidth to the scanner at the end of a long endoscopy instrument, and need to effectively model the demodulation process to avoid distortion of the sensor output.

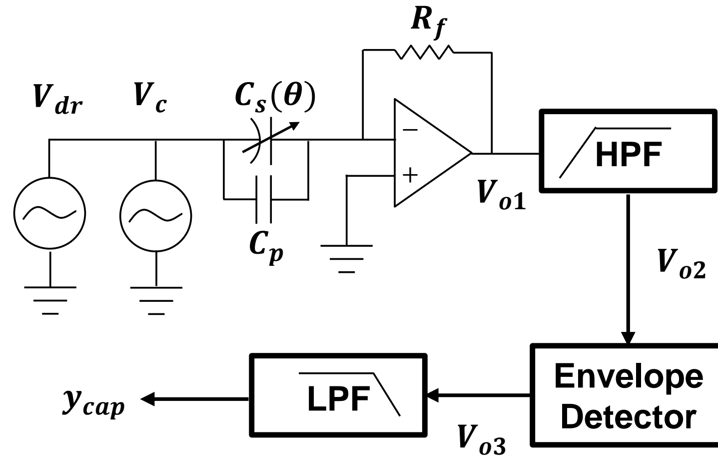


**Fig. 5.2. Schematic of driving and sensing circuit (1), place holder for frequency domain analysis**

As shown in Fig. 5.2, the circuit applied in this work consists of an amplification stage (a transimpedance amplifier with a feedback resistor), a high pass filter, a low pass filter and an envelope detector. An analysis is conducted to study the distribution of the frequency spectrum of the sensing signal. In this analysis, the parasitic capacitance is modeled as an additive capacitor $C_p$ connected in parallel with $C_s$, and the voltage outputs after the amplification stage, high pass filter, low pass filter, and the envelope detector are noted as $V_{o1}$, $V_{o2}$, $V_{o3}$, $y_{cap}$, respectively.

In order to obtain the relationship between the circuit output and the position of tilting motion over large angles, a model for $C_s(\theta)$is necessary for further derivation. In the analysis of frequency components of circuit outputs, $C_s$ is assumed to be a quadratic function of $\theta$.

$$C_s(t) = a_s\theta(t)^2 + b_s \tag{85}$$

where $a_s$is the scale factor of the capacitance model and $b_s$ is the static capacitance of the capacitance model. While the model in (83) is simpler than the true capacitance function, this model is used based on the observation the capacitance profile of a comb-finger is symmetric about $\theta$ and thus can be modeled by even number of order of polynomials [79], and the polynomial is simpler to analyze with respect to frequency content compared to other type of nonlinear functions during derivation.

Frequency analysis proceeds as follows: First, since the operating frequency of the electrostatic scanner is almost always around its resonance, the phase shifts introduced by the amplifiers are assumed to be constant, and such phase shifts can be calibrated during experimental methods. Then, $\theta$ can be modeled by a sinusoidal function, as

$$\theta = \theta_0 \sin(\frac{\omega_{dr}}{2}t + \phi) \tag{86}$$

where $\theta_0$ is amplitude of tilting motion, and $\phi$ is the phase of the tilting motion generated by the scanner's dynamic response. By substitution of (84) into (83), we have

$$C_s(t) = a_C\theta_0^2 \sin^2\left(\frac{\omega_{dr}}{2}t + \phi\right) + b_C \tag{87}$$

By applying trigonometric identity $\sin^2\left(\frac{\alpha}{2}\right) = \frac{1}{2}[1 - \cos(\alpha)]$, we have

$$C_s(t) = -\frac{a_C}{2}\theta_0^2\cos(\omega_{dr}t + 2\phi) + (\frac{a_C}{2}\theta_0^2 + b_C) \tag{88}$$

Therefore, $C_s$ is a sinusoidal function with frequency of $\omega_{dr}$, and the total capacitance $C_t(t)$ can be expressed

$$C_t(t) = -\frac{a_c}{2}\theta_0^2\cos(\omega_{dr}t + 2\phi) + \left(\frac{a_c}{2}\theta_0^2 + b_c + C_p\right) \quad (89)$$

Let $a_t = -\frac{a_C}{2}\theta_0^2$ and $b_t = \frac{a_C}{2}\theta_0^2 + b_C + C_p$. We have

$$C_t(t) = a_t cos(\omega_{dr}t + 2\phi) + b_t \quad (90)$$

The derivative of $C_s(t)$ with respect to time is

$$\frac{dC_s(t)}{dt} = \frac{a_t}{2}\theta_0^2\omega_{dr}\sin(\omega_{dr}t + 2\phi) \quad (91)$$

At the amplification stage, the sensing current generated by the all the capacitance in the circuit under external voltage $V$ can be amplified as:

$$V_{o1} = R_f\frac{d(V(t)(C_s(t)+C_p))}{dt} \quad (92)$$

where $R_f$ is the feedback resistance, and $V_{o1}$ can be further expressed as

$$V_{o1} = VR_f\frac{dC_s(t)}{dt} + C_sR_f\frac{dV(t)}{dt} + C_pR_f\frac{dV(t)}{dt} \quad (93)$$

By using a summing amplifier, input $V$ to the scanner's comb finger electrodes is implemented as

$$V(t) = V_{dr}(t) + V_c(t) \quad (94)$$

where $V_{dr}$ is the driving voltage,

$$V_{dr}(t) = V_{dr0}\sin(\omega_{dr}t) \quad (95)$$

and $V_c$ is the carrier voltage,

$$V_c(t) = V_{c0}\sin(\omega_c t) \quad (96)$$

where $V_{dr0}$ is the amplitude of driving voltage, $\omega_{dr}$ is the frequency of driving voltage, $V_{c0}$ is the amplitude of carrier voltage and $\omega_c$ is the carrier frequency.

Substituting the expression for $V$ into (91), and applying the chain rule, we have

$$V_{o1} = \frac{dC_s(t)}{dt} V_{dr0} R_f \sin(\omega_{dr} t) + \frac{dC_s(t)}{dt} V_{c0} R_f \sin(\omega_c t) + \omega_{dr} C_s(t) V_{dr0} R_f \sin(\omega_{dr} t) + \omega_c C_s(t) V_{c0} R_f \sin(\omega_c t) + \omega_{dr} C_p V_{dr0} R_f \sin(\omega_{dr} t) + \omega_c C_p V_{c0} R_f \sin(\omega_c t) \quad (97)$$

We denote each component in $V_{o1}$ (x) by $V_n$ subsequently:

$$V_{o1} = V_1 + V_2 + V_3 + V_4 + V_5 + V_6 \quad (98)$$

From the trigonometry identities, it can be shown that $V_1$, $V_3$ and $V_5$ are at the frequency band of $2\omega_{dr}$, and $V_2$, $V_4$ and $V_6$ are at frequency bands of $\omega_c + \omega_{dr}$ and $\omega_c - \omega_{dr}$. As illustrated in Fig. 5.3, the voltage components with frequency above $2\omega_{dr}$ are selected by the high pass filter ($V_2$, $V_4$, $V_6$). By selecting $\omega_c \gg \omega_{dr}$, the magnitude of $V_2$ can be neglected compared to $V_4$ and $V_6$. Therefore $V_{o2}$ can be approximated as

$$V_{o2} \approx a_{HPF}(V_4 + V_6) = a_{HPF} \omega_c V_{c0} R_f \sin(\omega_c t) C_t(t) \quad (99)$$

where $a_{HPF}$is the gain of the high pass filter.

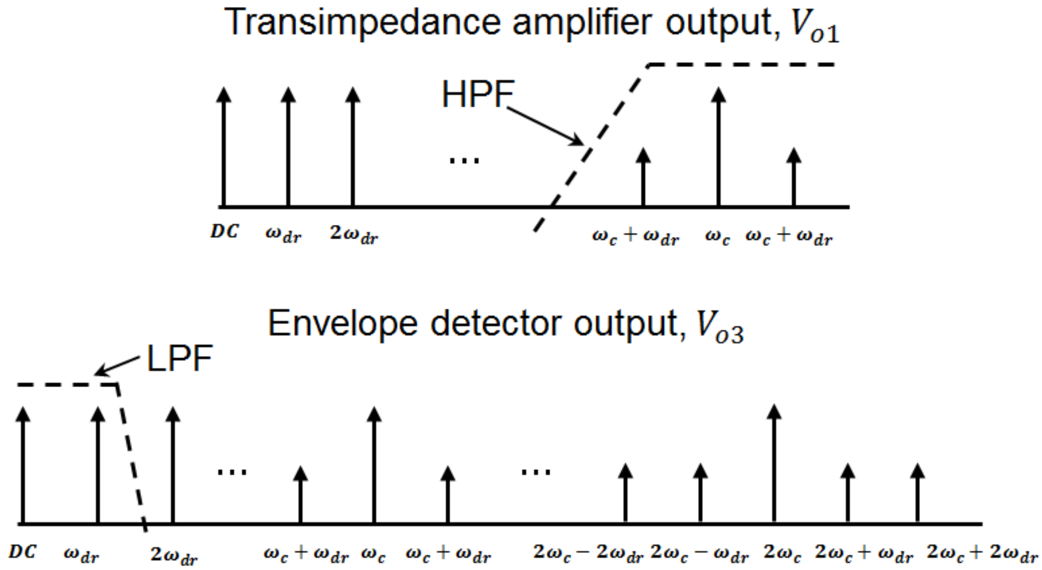


**Fig. 5.3. Frequency spectra illustration of sensing circuits**

The capacitive sensing signal $y_{cap}$ can be recovered using an envelope detector and a low pass filter. The envelope detector consists of a diode, a resistor as load and a low pass filter. The

output current of diode can be modeled using a square-law function [80], therefore voltage response of the envelope detector, $V_{o3}$ is modeled as

$$V_{o3} = a_d V_{o2} + b_d V_{o2}^2 \tag{100}$$

where $a_d$ is the scale factor of envelope detector model, and $b_d$ is the bias of the envelope detector model. Substituting $V_{o2}$ and let $a_{o3} = a_{HPF} a_d \omega_c V_{c0}$, $b_{o3} = b_d a_{HPF} \omega_c^2 V_{c0}^2$, we have

$$V_{o3} = a_{o3} cos(\omega_c t) C_t(t) + b_{o3} cos^2(\omega_c t) C_t(t)^2 \tag{101}$$

Expanding the quadratic term and applying trigonometry identities in (99), we have

$$V_{o3} = a_{o3} a_t cos(\omega_c t) \cos(\omega_{dr} t + 2\phi) + a_t b_t cos(\omega_c t) + \frac{1}{4} b_{o3} a_t^2 \cos(2\omega_{dr} t + 4\phi) +$$
$$b_{o3} a_t b_t cos(\omega_{dr} t + 2\phi) + \frac{1}{4} b_{o3} a_t^2 \cos(2\omega_c t) \cos(2\omega_{dr} t + 4\phi) +$$
$$b_{o3} a_t b_t cos(2\omega_c t) \cos(\omega_{dr} t + 2\phi) + \frac{1}{2} b_{o3} \left(\frac{1}{2} a_t^2 + b_t^2\right) \cos(2\omega_c t) + \frac{1}{2} b_{o3} \left(\frac{1}{2} a_t^2 + b_t^2\right) \tag{102}$$

The corresponding frequency bands for each component of $V_{o3}$ are illustrated in Fig. 5.3, and a low pass filter with cut-off frequency slightly above $\omega_{dr}$ is applied to $V_{o3}$.Therefore for output response of low pass filter, $y_{cap}$ can be expressed as

$$y_{cap} = a_{LPH} b_{o3} a_t b_t cos(\omega_{dr} t + 2\phi) + \frac{1}{2} a_{LPF} b_{o3} \left(\frac{1}{2} a_t^2 + b_t^2\right) \tag{103}$$

where $a_{LPF}$ is the gain of the low pass filter. By eliminating the term of $cos(\omega_{dr} t + 2\phi)$ using (86), and lumping all coefficients together, we have

$$y_{cap}(t) = a_{cir} C_s(\theta(t)) + b_{cir} \tag{104}$$

where $a_{cir}$ is gain of sensing circuit, and $b_{cir}$ is bias of sensing circuit. The above analysis shows that the $y_{cap}$ is a linear function of $C_s$, and the coefficients $a_{cir}$, $b_{cir}$ of can be identified using experimental methods once the circuit components is finalized. By modelling the nonlinear function $C_s$ of $\theta$ and identifying the relevant parameters, one can establish the overall measurement model $y_{cap}(\theta)$.

During estimator implementation, the capacitance model $C_s(\theta)$ was modeled with a Gaussian function instead of a quadratic function used in the sensing circuit modeling [64]:

$$C_s(\theta) = C_0 e^{-\left(\frac{\theta}{\theta_0}\right)^2} + C_b \tag{105}$$

where $C_0$ is the nominal capacitance, $C_b$is the capacitance bias and $\theta_0$ is the nominal angular displacement. The reason for choosing the Gaussian function for implementation is that it gives a bounded asymptotic value for $C_s$ when $\theta$ approaches its maximum or minimum value, and therefore can effectively prevent $C_s'$ to overflow in the recursive updating in EKF or UKF. A drawback is that frequency component analysis above does not exactly represent the real system, though the Gaussian function can also be reduced to a quadratic in Taylor expansion by excluding higher-order terms.

As a final sensor model for estimator design, replacing $C_s(\theta)$ as defined in (105) into (104) and assuming that an additive zero mean normally distributed noise, $v_k$ corrupts the measurment, we have a nonlinear discretized measurement model

$$y_{cap,k} = a_{cir}\left[C_0 e^{-\left(\frac{x_{1,k}}{\theta_0}\right)^2} + C_b\right] + b_{cir} + v_k \tag{106}$$

or

$$y_{cap,k} = h(x_{1,k}) + v_k \tag{107}$$

The parameters of $a_{cir}$, $b_{cir}$, $\theta_0$, $C_0$ and $C_b$ remain to be identified in experimentally and/or from component specifications..

### 5.3.4 EKF and UKF description

In order to estimate tilting motion, an EKF and an UKF were implemented. Both filters assume the state distribution can be represented by Gaussian Random Variables, and the process and / or the measurement model are non-linear. The difference between the two lies in the

methods used to estimate the mean and covariance of the states after propagation by the non-linear models. The details of the algorithms are described below, and their performance are evaluated and presented in Chapter 5.5. The superscript – stands for *a priori*, and subscript $k$ or $k-1$ stands for $k$-th sampling instance.

**Algorithm 1: EKF**

1. Project *a priori* state estimates

$$\widehat{\boldsymbol{X}}_k^- = g(\widehat{\boldsymbol{X}}_{k-1}, V_k), \quad \boldsymbol{P}_{\boldsymbol{k}}^- = \boldsymbol{G}_{\boldsymbol{k}} \boldsymbol{P}_{\boldsymbol{k-1}} \boldsymbol{G}_{\boldsymbol{k}}^{\boldsymbol{T}} + \boldsymbol{Q}$$

2. Propagating measurement model

$$\hat{y}_{cap,k} = h(\hat{x}_{1,k}^-)$$

3. Project *a posteriori* state estimates

$$\boldsymbol{K}_k = \boldsymbol{P}_{\boldsymbol{k}}^- \boldsymbol{H}_{\boldsymbol{k}}^{\boldsymbol{T}} \left( \boldsymbol{H}_{\boldsymbol{k}} \boldsymbol{P}_{\boldsymbol{k}}^- \boldsymbol{H}_{\boldsymbol{k}}^{\boldsymbol{T}} + R \right)^{-1}$$

$$\widehat{\boldsymbol{X}}_{\boldsymbol{k}} = \widehat{\boldsymbol{X}}_{\boldsymbol{k}}^- + \boldsymbol{K}_{\boldsymbol{k}} \left( y_{cap,k} - \hat{y}_{cap,k} \right), \quad \boldsymbol{P}_{\boldsymbol{k}} = \boldsymbol{P}_{\boldsymbol{k}}^- - \boldsymbol{K}_{\boldsymbol{k}} \boldsymbol{H}_{\boldsymbol{k}}^{\boldsymbol{T}} \boldsymbol{P}_{\boldsymbol{k}}^-$$

where $\widehat{\boldsymbol{X}}_k^-$ is the *a priori* states estimation, $\boldsymbol{P}_{\boldsymbol{k}}^-$ is the *a priori* error covariance matrix, $G_k$ is the Jacobian matrix of process model, $\boldsymbol{Q}$ is the covariance matrix of process noise, $\hat{y}_{cap,k}$ is the estimated measurement, $H_k$ is the Jacobian matrix of measurement model, $\boldsymbol{K}_{\boldsymbol{k}}$ is the Kalman gain, $R$ is covariance matrix of measurement noise, $\widehat{\boldsymbol{X}}_{\boldsymbol{k}}$ is the *a posteriori* states estimation and $P_k$ is the *a posteriori* error covariance matrix.

Compared to performing first order Taylor expansion to linearize the non-linear models (aka Jacobian matrix) in the EKF algorithm, the UKF selects a minimal number of sigma points to estimate the *a priori* and *a posteriori* mean and covariance of states, and therefore have more accurate estimation [81]. The UKF algorithm is described below.

**Algorithm 2: UKF**

1. Set sigma points

$$\boldsymbol{X}_{\boldsymbol{k-1}}^{\boldsymbol{sig}} = \left\{ \left( \widehat{\boldsymbol{X}}_{k-1}^{i}, W^{i} \right) \middle| i = 0 \ldots 2n_{aug} \right\}$$

2. Project *a priori* state estimates

$$\widehat{\boldsymbol{X}}_{\boldsymbol{k}}^{\boldsymbol{i,-}} = g(\widehat{\boldsymbol{X}}_{\boldsymbol{k-1}}^{\boldsymbol{i}}), \quad \widehat{\boldsymbol{X}}_{\boldsymbol{k}}^{-} = \sum_{i=0}^{2n_{aug}} W^{i}\, \widehat{\boldsymbol{X}}_{\boldsymbol{k}}^{\boldsymbol{i,-}}$$

$$\boldsymbol{P}_{\boldsymbol{x,k}}^{-} = \sum_{i=0}^{2n_{aug}} W^{i} \left[ \widehat{\boldsymbol{X}}_{\boldsymbol{k}}^{\boldsymbol{i,-}} - \widehat{\boldsymbol{X}}_{\boldsymbol{k}}^{-} \right] \left[ \widehat{\boldsymbol{X}}_{\boldsymbol{k}}^{\boldsymbol{i,-}} - \widehat{\boldsymbol{X}}_{\boldsymbol{k}}^{-} \right]^{T} + \boldsymbol{Q}$$

3. Propagating measurement model

$$\hat{y}_{cap,k}^{i} = h(\hat{x}_{1,k}^{i,-}), \quad \hat{y}_{cap,k} = \sum_{i=0}^{2n_{aug}} W^{i} \hat{y}_{k}^{i}$$

$$P_{y,k} = \sum_{i=0}^{2n_{aug}} W^{i} \left[ \hat{y}_{cap,k}^{i} - \hat{y}_{cap,k} \right] \left[ \hat{y}_{cap,k}^{i} - \hat{y}_{cap,k} \right]^{T} + R$$

4. Project *a posteriori* state estimates

$$\boldsymbol{P}_{\boldsymbol{xy,k}} = \sum_{i=0}^{2n_{aug}} W^{i} \left[ \widehat{\boldsymbol{X}}_{\boldsymbol{k}}^{\boldsymbol{i,-}} - \widehat{\boldsymbol{X}}_{\boldsymbol{k}}^{-} \right] \left[ \hat{y}_{cap,k}^{i} - \hat{y}_{cap,k} \right]^{T} + R$$

$$K_{k} = P_{xy,k} P_{y,k}^{-1}$$

$$\widehat{\boldsymbol{X}}_{\boldsymbol{k}}^{\boldsymbol{i}} = \widehat{\boldsymbol{X}}_{\boldsymbol{k}}^{\boldsymbol{i,-}} + K_{k}(y_{cap,k}^{i} - \hat{y}_{cap,k}^{i}), \quad \boldsymbol{P}_{\boldsymbol{x,k}} = \boldsymbol{P}_{\boldsymbol{x,k}}^{-} + K_{k} P_{y,k} K_{k}^{T}$$

where $\boldsymbol{X}_{\boldsymbol{k-1}}^{\boldsymbol{sig}}$ is a set of sigma vectors and their associated weights, $\widehat{\boldsymbol{X}}_{k-1}^{i}$ is a sigma vector and $W^{i}$ is its associated weight. $\widehat{\boldsymbol{X}}_{\boldsymbol{k}}^{\boldsymbol{i,-}}$ is sigma vector transformed by the process model, $\widehat{\boldsymbol{X}}_{\boldsymbol{k}}^{-}$ is the mean of *a priori* states estimation, $\boldsymbol{P}_{\boldsymbol{x,k}}^{-}$ is the a priori error covariance matrix, $\boldsymbol{Q}$ is the covariance matrix of process noise, $\hat{y}_{cap,k}^{i}$ is the estimated measurement with ith sigma vector, $\hat{y}_{cap,k}$ is the estimated measurement, $P_{y,k}$ is the covariance of measurement estimation, $\boldsymbol{P}_{\boldsymbol{xy,k}}$ is the cross covariance between estimated states and measurement, *R* is the covariance matrix of measurement noise, $\widehat{\boldsymbol{X}}_{\boldsymbol{k}}^{\boldsymbol{i}}$ is the mean of *a posteriori* states estimates and $\boldsymbol{P}_{\boldsymbol{x,k}}$ is the *a posteriori* error covariance matrix.

## 5.4 **Experiments**

This section describes the experimental set-up and the procedure of experiments for model identification and estimation validation and evaluation. Necessary post-analysis is also described.

### 5.4.1 Description of set-up

The experimental set up is depicted in Fig. 5.4. The two command voltages were added using a summing amplifier and then amplified by a TEGAM 2340 amplifier with 20 times amplification. The amplified amplitude modulated driving voltage was fed into a dual axis electrostatic micro-scanner (Fig. 5.1). Experiments were conducted during both continuous operation (for estimator evaluation) and ring-down (for parameter identification).

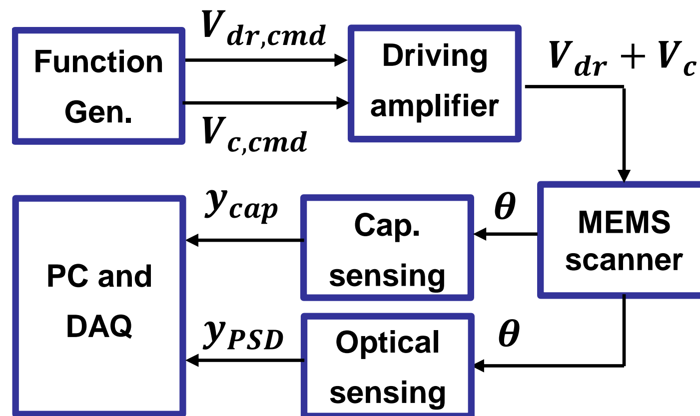


**Fig. 5.4. Schematic of experimental set-up. A optical sensing system is used to provide ground truth measurement of the tilting motion.**

The tilting motion of the micro-scanner was transduced into the sensing signal $y_{cap}$ by the sensing circuit described in section 5.3-B (Fig. 5.2) and recorded by the DAQ system.

As shown in Fig. 5.5, an optical sensing stage with an ON-TRAK PSM 2-10 position sensing detector (PSD) was also used to measure the tilting angle as shown in Fig. 5.5. A laser beam was directed to a BS004 Thorlabs beam splitter, and half of the laser is reflected and

directed to the mirror surface of the MEMS scanner at a 0 °incidence angle. With the MEMS scanner driven by external voltage stimulus, the mirror surface rotates around its axis and reflects the incoming beam to the same beam splitter, and half of the reflected beam will be received by the PSD and converted into a voltage signal $y_{PSD}$. $y_{PSD}$ was converted into angular displacement and then treated as ground truth, which is used to identify parameters of actuator and sensor model and to evaluate the performance of EKF and UKF.

**Table 5.1 Experimental settings for electrostatic micro-scanner**

| Symbol | Description | Value |
|---|---|---|
| $V_{dr0}$ | Amplitude of driving voltage | 30 V |
| $V_{c0}$ | Amplitude of carrier voltage | 6 V |
| $f_{dr}$ | Frequency of driving voltage | 31.10 to 31.15 kHz |
| $f_c$ | Frequency of carrier voltage | 500 kHz |
| $R_f$ | Feedback resistors | 17.86 kohm |
| $V_{bias}$ | Bias voltage | 23.76 V |

During ring-down tests, the capacitive sensing signal, PSD readout are recorded using a NI PCIe 6251 DAQ with 16 bit resolution and 1 MHz sampling rate. A customized LabVIEW program was developed to send command voltage and log data. During steady state frequency sweeps, a dual channel function generator was used to provide command carrier voltage and provide voltage to the driving circuit, while an Agilent InfinitiVision DSO-X 2024A oscilloscope was used to record the driving voltage, capacitive sensing signal, PSD readout.

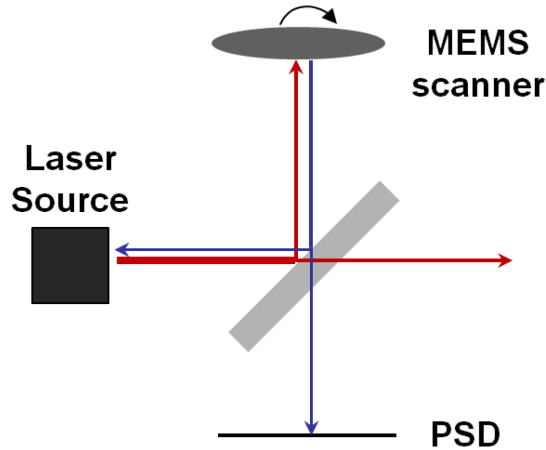


**Fig. 5.5. Schematic of optical sensing device. A beam splitter is used to deflect the laser beams from the source and from the MEMS scanner in order to reduce the distortion generated.**

### 5.4.2 Experimental procedures

Two types of experiments were performed in order to identify the actuator and sensor models and to evaluate estimators' performance.

The first type of experiments is to identify the actuator model and capacitance profile using ringdown tests [75]. The driving voltage was swept in frequency from high to low at 31.10 kHz to reach the scanner's maximum tilting amplitude. After the tilting motion stabilized, the driving voltage was changed from AC to DC to allow the scanner to free oscillate with a constant bias voltage. The sensing voltage created by the ringdown motion under constant bias was then recorded.

The second type of experiments is steady state frequency sweeps. During these experiments, the scanner was excited with amplitude modulated driving voltages, and the sensing signal, PSD measurement and driving voltages were recorded to train and evaluate the estimators. The driving voltage, $V_{dr}$ was set to be 0 to 60 V amplitude and swept in frequency from 31.10 kHz to 31.15 kHz. The carrier voltage, $V_c$ was set to be 500 kHz in and 12 V amplitude. The experimental settings are summarized in Table 5.1.

### 5.4.3 Post-process

The data were post-processed to identify the parameters in process model, sensor model, and estimators. The data set obtained in the steady state frequency sweeps was also split into a training set and testing set to allow training and test of parameter values with separate measurements.

## 5.5 **Results and discussion**

This section presents results of motion tracking tests. The identified parameters for the process model and sensor model are presented. The EKF and UKF estimator are validated against ground truth measurement, and their performances are compared and discussed.

### 5.5.1 Actuator model identification

The actuator model is identified by first calculating the moment of inertia, $J$ using the dimensions of design parameter of micro-scanner, and then fitting the decay curve of the experimentally measured ringdown trajectory using a linear viscous damping and spring constant [75]. The identified parameters are shown in

Table 5.2.

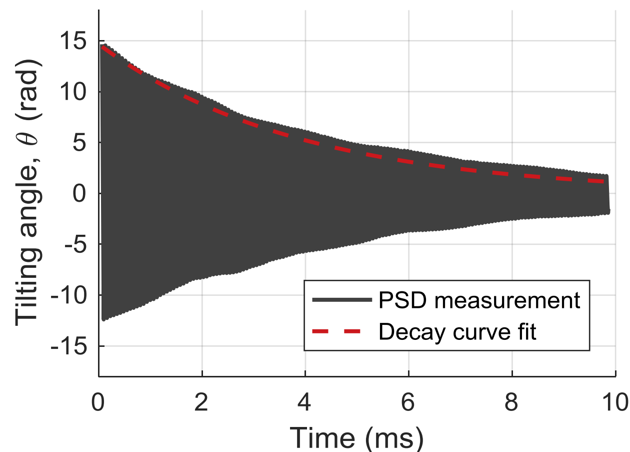


**Fig. 5.6. Measurement of ringdown test and fitted decay curve for actuator model parameter identification**

The capacitance model was identified using experimental by mapping the trajectory $C_s(t)$ versus $\theta(t)$measured by PSD in the ringdown tests [51]. First, $C_s(t)$ is obtained by integrating $y_{cap}$ with respect to time.

$$C_s(t) = \int_{t_0}^{t_f} -R_s V_{bias} y_{cap} dt \quad (108)$$

where $V_{bias}$ is the DC bias voltage applied to the capacitance during the ringdown tests. Then $\theta_0$, $C_0$ and $C_b$ are identified by fitting the Gaussian model described in (103). The parameters associated with the circuit $a_{cir}$ and $b_{cir}$ are identified using steady state measurements. The parameters are summarized in

Table 5.2, and the identified capacitance profile is shown in Fig. 5.7.

**Table 5.2 Identified parameters of actuator model, sensor model, EKF and UKF**

| Symbol | Description | Value |
|---|---|---|
| $J$ | Moment of inertia | $1.15 \times 10^{-14}$ kg m$^2$ |
| $k$ | Spring constant | $1.10 \times 10^{-4}$ N m |
| $b_v$ | Viscous damping coefficient | $5.95 \times 10^{-12}$ N m/s |
| $Q_a$ | Covariance of process noise | $10^{11}$ m/s$^2$ |
| $\theta_0$ | Nominal angular displacement | 0.2 rad |
| $C_0$ | Nominal capacitance | 5.71 pF |
| $C_b$ | Parasitic capacitance | 9.79 pF |
| $a_{cir}$ | Circuit scale factor | -0.3574 V/pF |
| $b_{cir}$ | Circuit bias | 6.3945 V |
| $R$ | Covariance of measurement noise | $1.92 \times 10^{-4}$ V$^2$ |

### 5.5.2 Sensor model identification

During testing, frequency content was observed using spectral analysis on the oscilloscope, and locations of significant amplitude at relevant points in the filtering process

were observed to qualitatively agree with the frequency content predicted by the analysis, though full quantitative analysis of the intermediate signals was not performed. The sensing capacitance is identified by building correspondence between the identified capacitance and ground truth angle measurement [78]. A capacitance model is fit to the experimentally identified capacitance profile to extend the mapping between the angle and capacitance, the identified model is described by (103) and shown in Fig. 5.7.

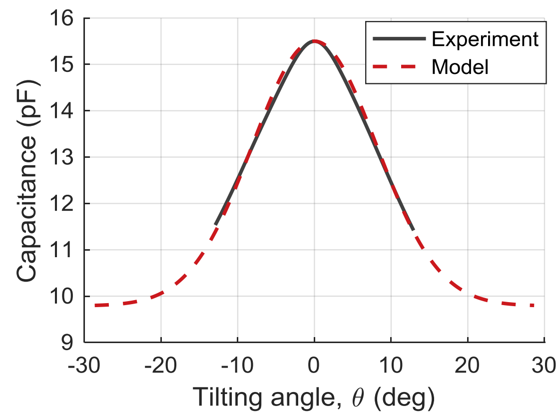


**Fig. 5.7. Experimentally identified capacitance profile and modeled capacitance profile.**

### 5.5.3 Estimators performance comparison

Fig. 5.8 shows the driving voltage, measured and estimated tilting angle and sensor output. The discrepancy between the estimated sensing shows that EKF introduces error during the linearization of process and observation model.

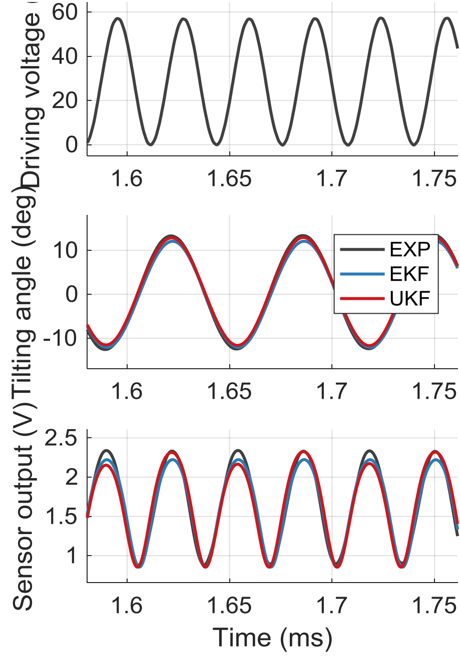


**Fig. 5.8. Experimentally measured driving voltage (top), tilting angle measured by optical sensing (EXP) and estimated by EKF, UKF (mid), measured and estimated sensing output by optical sensing, EKF and UKF respectively (bottom).**

The performance of the estimators is evaluated with two metrics: estimation accuracy of tilting angle and phase shift. The phase shift of the micro-scanner is defined as the difference of the timing between the peak value of an angular displacement and the prior peak value of the driving voltage. The estimation accuracy of phase shift is computed by the root-mean-square error (RMSE) between the estimated phase shift and the phase shift computed using ground truth measurement:

$$\phi_{RMSE} = \sqrt{\frac{1}{N}\sum_{i=0}^{N}(\phi_{est,i} - \phi_{meas,i})} \qquad (109)$$

where $\phi_{RMSE}$ is RMSE of phase shift estimation, $\phi_{est,i}$ is the phase shift for ith period of estimated tilting motion, $\phi_{meas,i}$ is the phase shift for ith period of ground truth tilting motion and $N$ is the total number of period of tilting motion. Similarly, the RMSE of tilting angle is defined as:

$$\theta_{RMSE} = \sqrt{\frac{1}{N}\sum_{i=0}^{N}(\theta_{est,i} - \theta_{meas,i})} \tag{110}$$

where $\theta_{RMSE}$ is RMSE of tilting angle estimation, $\theta_{est,i}$ is the estimated tilting angle at ith sampling instance, $\phi_{meas,i}$ is the ground truth tilting angle at the $i$-th sampling instanc and $N$ is the total number of sampling instances.

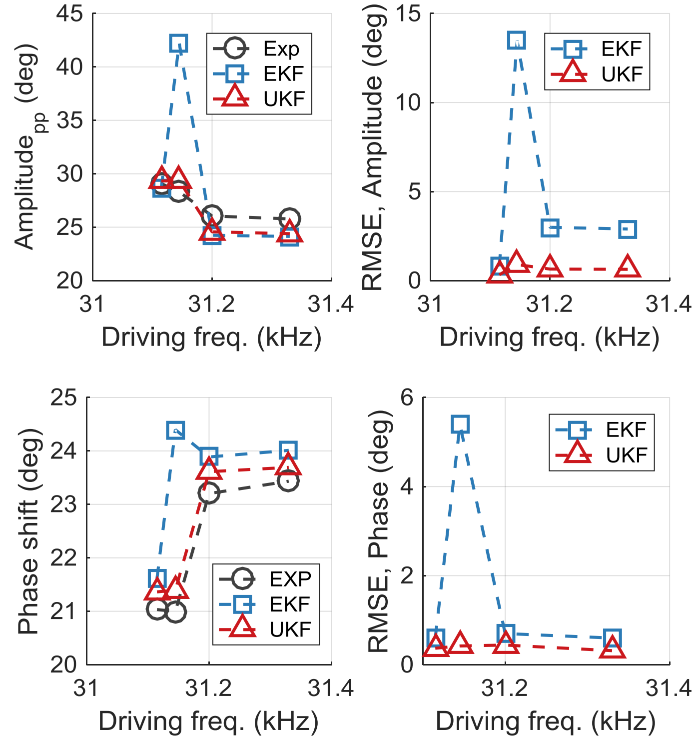


**Fig. 5.9. Measured and Estimated tilting angles and phase shift, and RMSE of tilting angle and phase shift.**

Fig. 5.9 shows the peak to peak amplitude and phase shift by measurement and estimation, and corresponding RMSEs. From the comparison, the UKF gives better estimation accuracy than the EKF. The RMSE in all the testing data set is summarized in Table 5.3.

**Table 5.3 RMSE of estimated phase shift and amplitude by implemented estimators**

| Estimator | RMSE amplitude (deg) | RMSE phase shift (deg) |
|---|---|---|
| EKF | 5.04 | 1.82 |
| UKF | 0.63 | 0.39 |

## 5.6 **Chapter summary**

We present a method to estimate tilting motion of electrostatic micro-scanner used for scanning purpose in an endoscopy. The estimated amplitude and phase shift can be helpful to reduce the blur and distortion of the image reconstructed. The challenge of the present

application is to fetch meaningful sensing signal related to the tilting motion of the scanner without adding structures dedicated for sensing due to the restriction imposed on the size of the device. Therefore we propose a method to implement high-accuracy state estimation using same comb-fingers for both driving and sensing purpose.

The method includes an AMDM circuit design to separate feedthrough generated by the high driving voltage. Novelties of the proposed sensor and estimator implementation include a process model based on non-linear parametric dynamics of micro-scanner and a non-linear sensor model including a Gaussian based capacitance model and a nonlinear circuit model. Model parameters are identified with experimental measurements. Both EKF and UKF estimators are used to incorporate the models into phase angle and tilt angle measurement, and estimation performance are examined and compared.

The results show that the UKF achieved 0.39 degree RMSE in phase estimation and 0.63 degree RMSE in amplitude estimation, while the EKF achieved 1.82 degree RMSE in phase estimation and 5.04 degree RMSE in amplitude estimation. The higher estimation accuracy of the UKF over EKF is likely due to the UKF being more accurate in estimating mean and covariance of states propagated by non-linear models than the EKF.

# Chapter 6
# Concluding Remarks

## 6.1 **Summary**

The main objective of this dissertation has been to present a framework for performing high accuracy motion estimation for a selection of MEMS devices with capacitive sensors and integrated actuation capability. In Chapter 2, conventional electrode configurations for position sensing with commonly used sensing circuitries and the standard extended Kalman filter (EKF) for nonlinear process estimation were introduced. The dissertation then presented three applications and formulations of the motion estimation problems for their specific actuation schemes, nonlinear capacitive sensing configurations, and associated signal processing techniques, to achieve high-accuracy motion estimation in each application.

In Chapter 3, an EKF motion estimator for a MEMS micro-stage with 6-DOF piezoelectric actuation and a rotational parallel-plate capacitive sensor design was introduced. The estimated motion is used as reference motion for *in-situ* calibration of an on-stage MEMS inertial measurement unit (IMU). In order to provide highly accurate motion estimation, the capacitive sensors are designed to reduce off-axis motion sensitivity, and repetitive measurements with different bias voltage are made to reduce feedthrough. A nonlinear sensor model is derived to map the rotational motion into capacitance and is experimentally identified. Experiments show that the calibrated scale factor accuracy of a test MEMS gyroscope improves two orders of magnitude compared to operation without the micro-stage calibration.

In Chapter 4, a concept for threshold position sensing based on non-monotonic capacitance profiles was examined, analyzed and experimentally validated with a dual axis electrostatic micro-scanner. The threshold position sensing provides sensitive and highly accurate indication of certain position information from the electrodes, and it is largely insensitive to environmental perturbations such as temperature. In order to extract the threshold signal from noises and bias, a derivative of Gaussian (DOG) filter is designed to detect the rapid change of signal due to threshold position crossings. An EKF based motion estimator with augmented sensor model for threshold detection is presented and implemented. Experimental results show that use of threshold sensing on average improves EKF estimation accuracy by 15.1% across all tested SNR conditions.

In Chapter 5, EKF and unscented Kalman filter (UKF) motion estimation schemes were presented for an electrostatic micro-scanner used for scanning purposes in endoscopic microscopy. The estimated amplitude and phase shift can be helpful to reduce the blur and distortion of the image reconstructed. Due to stringent space limitations, the sensing signal has to be obtained with the same comb-fingers used for both driving and sensing. The implemented method includes an amplitude modulation-demodulation (AMDM) circuit design to separate feedthrough generated by the high driving voltage.  A sensor model incorporating a Gaussian capacitance profile and circuit principle frequency analysis are presented. Model parameters are identified with experimental measurements. Both EKF and UKF estimators are used to incorporate the models into phase angle and tilt angle measurement, and estimation performance is examined and compared.

The pros and cons of the methods associated with capacitive sensors that have been discussed in this dissertation are summarized in Table 6.1.

**Table 6.1 Summary of pros and cons for discussed methods associated with capacitive sensors**

| Methods | Pros | Cons |
|---|---|---|
| Capacitive sensor for analog measurement | • Plenty of existing designs | • Prone to temperature change |
| Capacitive sensor for threshold measurement | • High accuracy measurement of threshold location<br>• Robust to temperature change. | • Requires special structure<br>• Need DC circuit and prone to feedthrough |
| AMDM circuit | • Separate feedthrough in frequency domain | • Complicated circuit design<br>• More delays and undesired dynamics |
| DC circuit | • Easier to design and implement<br>• Easier to derive sensor model<br>• Less delay and undesired dynamics | • Does not separate feedthrough in frequency domain |
| EKF | • Easier to implement<br>• Lower computational complexity<br>• Plenty of examples in literature | • Low accuracy (~1$^{st}$ order Taylor) |
| UKF | • Higher accuracy (~3$^{rd}$ order Taylor) | • Higher computational complexity<br>• Selection of sigma points requires a lot of tuning |

It is worth noting that even though the estimation schemes of EKF and UKF in this study are performed in off-line computation, the EKF still shows advantages over UKF in terms of computational complexity. The main reason for fast computation is that the EKF does not involve a sigma point sampling process therefore has fewer tates to update in each recursive steps.

## 6.2 **Research contributions**

The contributions of the dissertation include:

1. Design of a rotational parallel-plate capacitive sensor configurations with derivation and identification of corresponding nonlinear sensor models to use nonlinear features to improve system performance.
2. Development of signal processing technique to reliably and efficiently detect threshold position signals formed by the unique capacitive sensor configurations, and integration of these detection techniques into estimation schemes and experimental validation of effectiveness in terms of estimation accuracy improvement.
3. Development of a nonlinear sensor model for electrostatic micro-scanners using shared electrodes for sensing and driving. The sensor model is important to analyze the principle frequency bands of sensing single and serve as a design guideline for band pass filter selection for the separation of feedthrough. It also provides a framework for designing and analyzing the sensing circuit to retrieve sensing signals during multi-DOF actuation using shared electrodes.
4. Description of a framework for integrating the proposed nonlinear capacitive sensor models and dynamic models of actuators for the MEMS devices into nonlinear filters such as the EKF and UKF.

## 6.3 **Recommendations for future works**

### 6.3.1 Non-orthogonality calibration

The *in-situ* MEMS IMU calibration method discussed in Chapter 3 has limitations of lack of rate table testing and possible presence of misalignment errors. Future work would require compact circuit integration for full rate table calibration and validation, especially over a larger temperature range in an environmentally controlled setting. Meanwhile, the current method does

not separate the error of $SF_{IMU}$ from any errors of non-orthogonality that may be introduced by misalignment of triads of the gyroscope within the IMU [45], misalignment between the IMU and the micro-stage, and any mismatch between the center of rotation and the center of the IMU. Potential future works to improve the calibration method include investigating how to make use of multi-axis excitation to improve calibration performance and how to calibrate non-orthogonal error terms caused by possible misalignment between the micro-stage and MEMS IMU and the mismatch between the center of rotation and the center of the MEMS IMU. To identify those deterministic error terms to add to the current method will be a beneficial supplement to the presented calibration method.

### 6.3.2 Threshold sensing without complete power cut-off

The experimental validation of threshold position sensing shows it is effectiveness in improving estimation accuracy in the absence of inference from any feedthrough signal. Future studies in this topic are suggested to focus on investigating methods of using threshold sensing based motion estimation without complete power cut-off. One potential path is to have periodic and brief AC power cut-off periods to avoid feedthrough and switch to a DC bias voltage supply for threshold sensing based estimation during these periods.  Effects of transient dynamic effects during these brief cut-off periods would have to be evaluated.

### 6.3.3 Multi-axis motion estimation with shared electrodes

In this dissertation, single axis motion estimation using shared electrodes for driving and sensing is shown. For micro-scanners used for endomicroscope applications, multi-degree-of-freedom actuation is required to achieve designated scanning patterns. Therefore, a higher order motion estimator using shared electrodes can be more helpful to improve imaging quality. In order to achieve that goal, a more sophisticated sensing circuit is required to incorporate

bandpass filtering for motion signals carried at two or more resonant frequencies, and an expanded analysis and modeling effort for the sensor model including the circuit will be very helpful in terms of understanding the frequency bands of the signal and providing design guidelines for bandpass filter selections. An accurate multi-DOF process modeling effort would also be necessary in nonlinear filter implementation to compensate for potential sensor signal degradation due to multiple motion signals mixing.

### 6.3.4 Optimization for on-line estimation

Future works regarding optimization of the estimation scheme is also recommended to implement online estimation schemes for near real-time feedback control, image registration and in-situ sensor calibration purposes. Potential paths include reducing sampling rate while maintaining acceptable estimation accuracy, only performing sensor measurement updates in an EKF / UKF when needed and optimizing Jacobian matrix computation in the EKF, etc.

## Appendix

Table A.1 lists the upper and lower limits of the integration to evaluate each sensing capacitance shown in Fig. A.1 with dual axis capacitive sensor model.

**Table A.1. Upper and lower limits of integration for each sensing capacitor**

| | $w_1$ | $w_2$ | $w_3$ | $w_4$ |
|---|---|---|---|---|
| 1A | $-0.5W$ | $-0.5W + W_{SA}$ | $-0.5W_{SA}$ | $0.5W_{SA}$ |
| 1B | $0.5W - W_{SA} - D_W - W_{SB}$ | $0.5W - W_{SA} - D_W$ | $-0.5W_{SA}$ | $0.5W_{SA}$ |
| 2A | $0.5W - W_{SA}$ | $0.5W - W_{SA} - W_{SB}$ | $-0.5W_{SA}$ | $0.5W_{SA}$ |
| 2B | $-0.5W + W_{SA} + D_W$ | $-0.5W + W_{SA} + D_W + W_{SB}$ | $-0.5W_{SA}$ | $0.5W_{SA}$ |

Fig. A.1 illustrates the geometric relation of the rotors and stators with more detailed dimensional variables. $D_W$ is the distance between the inner and outer stator, and $W$ is the total distance across the rotors.

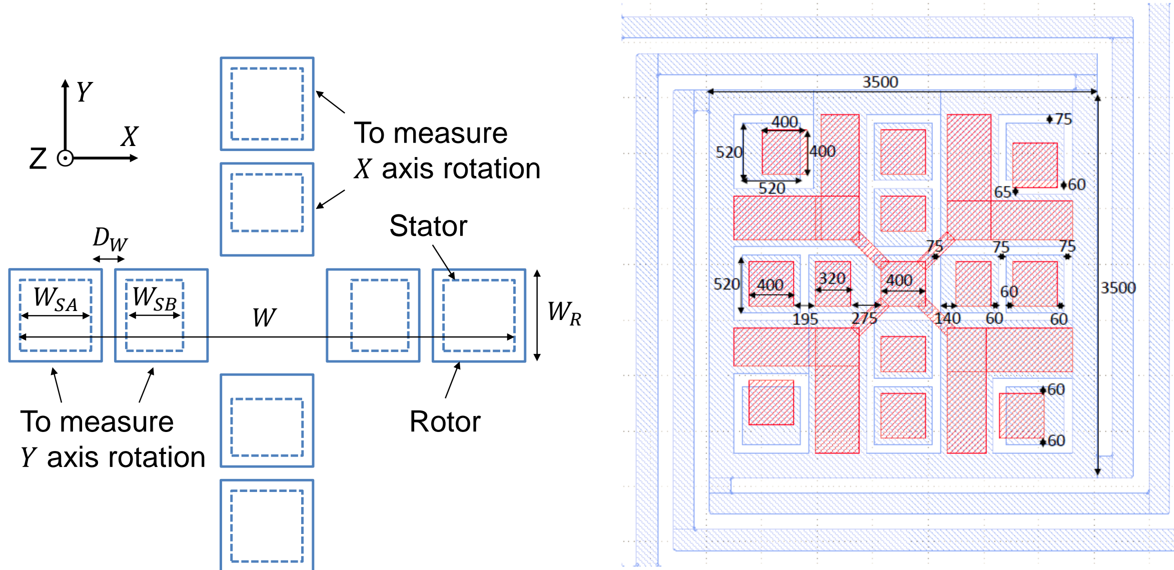


**Fig. A.1. Design of capacitive sensor for *X* and *Y* rotational motion (top view) with key dimensions labels (left); CAD drawing (top view) of all electrodes layout for sensing *X* and *Y* rotational and translation motions (right)**

Table A.2 tabulates key dimensions of capacitive sensors presented in Chapter 3 and Fig. A.1. With these dimensions, the capacitance model described by Eq.(41) and Eq.(42) can be evaluated.

**Table A.2 Dimension of capacitive sensors with rotational parallel-plate configuration**

| Symbol | Design Parameter | Value ($\mu m$) |
|---|---|---|
| $W_{SA}$ | Width of large stator electrode | 400 |
| $W_{SB}$ | Width of small stator electrode | 320 |
| $W_R$ | Width of each rotor electrode | 520 |
| $W$ | Width of sensing stage | 2780 |
| $D_W$ | Distance between stators | 195 |

# Bibliography


[1] A. J. Fleming, "A review of nanometer resolution position sensors: Operation and performance," *Sensors and Actuators A: Physical,* vol. 190, no. 1, pp. 106 - 126, 2013.

[2] L. K. Baxter, Capacitive Sensors: Design and Applications, Wiley-IEEE Press, 1996.

[3] Z. Rittersma, "Recent achievements in miniaturised humidity sensors—a review of transduction techniques," *Sensors and Actuators A: Physical,* vol. 96, no. 2-3, pp. 196-210, 2002.

[4] N. Yazdi, H. Kulah and K. Najafi, "Precision readout circuits for capacitive microaccelerometers," in *IEEE Sensors*, Vienna, 2004.

[5] D. K. Shaeffer, "MEMS inertial sensors: a tutorial overview," *IEEE Communications Magazine,* pp. 100 - 109, 11 April 2013.

[6] N. Yazdi, F. Ayazi and K. Najafi, "Micromachined inertial sensors," *Proceedings of the IEEE,* pp. 1640 - 1659, 1998.

[7] F. N. Toth and G. C. Meijer, "A low-cost, smart capacitive position sensor," *IEEE Transactions on Instrumentation and Measurement,* vol. 41, no. 6, pp. 1041-1044, 1992.

[8] M. Kim, W. Moon, E. Yoon and K.-R. Lee, "A new capacitive displacement sensor with high accuracy and long-range," *Sensors and Actuators A: Physical,* vol. 130, pp. 135-141, 2006.

[9] W. P. Eaton and J. H. Smith, "Micromachined pressure sensors: review and recent developments," *Smart Materials and Structures,* vol. 6, no. 5, p. 530, 1997.

[10] Y. Sun, B. J. Nelson, D. Potasek and E. Enikov, "A bulk microfabricated multi-axis capacitive cellular force sensor using transverse comb drives," *Journal of Micromechanics and Microengineering,* vol. 12, no. 6, 2002.

[11] P. R. V. d. D. A. G. H. O. W. &. B. P. Scheeper, "A review of silicon microphones," *Sensors and actuators A: Physical,* vol. 44, no. 1, pp. 1 - 11, 1994.

[12] U. Kang and K. D. Wise, "A high-speed capacitive humidity sensor with on-chip thermal reset," *IEEE Transactions on Electron Devices,* vol. 47, no. 4, pp. 702-710, 2000.

[13] Z. Chen and R. C. Luo, "Design and implementation of capacitive proximity sensor using microelectromechanical systems technology," *IEEE Transactions on Industrial Electronics,* vol. 45, no. 6, pp. 886 - 894, 1998.

[14] J. Rekimoto, "SmartSkin: an infrastructure for freehand manipulation on interactive surfaces," in *Proceedings of the SIGCHI Conference on Human Factors in Computing Systems*, Minneapolis, 2002.

[15] H.-K. Kim, S. Lee and K.-S. Yun, "Capacitive tactile sensor array for touch screen application," *Sensors and Actuators A: Physical,* vol. 165, no. 1, pp. 2-7, 2011.

[16] D. Titterton and J. Weston, Strapdown Inertial Navigation Technology, London: The Institution of Engineering and Technology, The American Institute of Aeronautics, 2004.

[17] E. E. Aktakka and K. Najafi, "A six-axis micro platform for in situ calibration of MEMS inertial sensors," in *29th IEEE International Conference on Micro Electro Mechanical Systems (MEMS'16)*, Shanghai, 2016.

[18] Y. Zhu, S. O. Moheimani and M. R. Yuce, "Simultaneous capacitive and electrothermal position sensing in a micromachined nanopositioner," *EEE Electron Device Letters,* vol. 32, no. 8, pp. 1146 - 1148, 2011.

[19] U. Baran, D. Brown, S. Holmstrom, D. Balma, W. O. Davis, P. Muralt and H. Urey, "Resonant PZT MEMS scanner for high-resolution displays," *Journal of Microelectromechanical Systems,* vol. 21, no. 6, pp. 1303 - 1310, 2012.

[20] R. Schroedter, M. Schwarzenberg, A. Dreyhaupt, R. Barth, T. Sandner and K. Janschek, "Microcontroller based closed-loop control of a 2D quasi-static/resonant microscanner with on-chip piezo-resistive sensor feedback," in *Proc. SPIE 10116, MOEMS and Miniaturized Systems XVI*, San Francisco, 2017.

[21] S. T. Holmstrom, U. Baran and H. Urey, "MEMS Laser Scanners: A Review," *Journal of Microelectromechanical Systems,* vol. 23, no. 2, pp. 259 - 275, 2014.

[22] L. Clark and B. Shirinzadeh, "Modeling of two-plate capacitive position sensing systems for high precision planar three DOF measurement," *Precision Engineering,* vol. 46, pp. 383-392, 2016.

[23] D.-H. Jeong, S.-S. Yun, B.-G. Lee, M.-L. Lee, C.-A. Choi and J.-H. Lee, "High-resolution capacitive microinclinometer with oblique comb electrodes using (110) silicon," *Journal of Microelectromechanical Systems,* vol. 20, no. 6, pp. 1269-1276, 2011.

[24] A. C.-L. Hung, H. Y.-H. Lai, T.-W. Lin, S.-G. Fu and M. S.-C. Lu, "An electrostatically driven 2D micro-scanning mirror with capacitive sensing for projection display," *Sensors and Actuators A: Physical,* vol. 222, no. 1, pp. 122 - 129, 2014.

[25] A. A. Trusov and A. M. Shkel, "Capacitive detection in resonant MEMS with arbitrary amplitude of motion," *Journal of micromechanics and microengineering,* vol. 17, no. 8, p. 1583, 2007.

[26] S. I. Moore and S. O. R. Moheimani, "Vibration control with MEMS electrostatic drives: a self-sensing approach," *IEEE Transactions on Control Systems Technology,* vol. 23, no. 3, pp. 1237-1244, 2015.

[27] P. G. Corro, M. Imboden, D. J. Pérez, D. J. Bishop and H. Pastoriza, "Single ended capacitive self-sensing system for comb drives driven XY nanopositioners," *Sensors and Actuators A: Physical,* vol. 271, pp. 409-417, 2018.

[28] G. Stemme, "Resonant silicon sensors," *Journal of Micromechanics and Microengineering,* vol. 1, no. 2, p. 113, 1991.

[29] B. Edamana, Y. Chen, D. Slavin, E. E. Akatakka and K. R. Oldham, "Estimation with threshold sensing for gyroscope calibration using a piezoelectric microstage," *IEEE Transactions on Control Systems Technology,* vol. 23, no. 5, pp. 1943 - 1951, 2015.

[30] T. Henningsson and K. J. Åström, "Log-concave observers," in *Proc. of Mathematical Theory of Networks and Systems*, Kyoto, 2006.

[31] K. J. Aström, "Event based control," in *Analysis and design of nonlinear control systems*, Berlin, Springer, 2008, pp. 127 - 147.

[32] Y. Chen and K. R. Oldham, "Kalman filter estimation with edge detection-based hybrid

sensing," in *American control Conference*, Boston, 2016.

[33] J. Qu and K. R. Oldham, "Position estimation for a capacitively-sensed magnetoelastic rotary microstage using an extended Kalman smoother," in *American Control Conference*, Portland, 2014.

[34] N. Yazdi, H. Kulah and K. Najafi, "Precision readout circuits for capacitive microaccelerometers," in *Proceedings of IEEE Sensors 2004*, Vienna, 2004.

[35] B. Cagdaser, A. Jog, M. Last, B. S. Leibowitz, L. Zhou, E. Shelton, K. S. Pister and B. E. Boser, "Capacitive sense feedback control for MEMS beam steering mirrors," in *Solid-state Sensor, Actuator and Microsystems Workshop*, Hilton Head Island, 2004.

[36] F. Daum, "Nonlinear filters: beyond the Kalman filter," *IEEE Aerospace and Electronic Systems Magazine,* vol. 20, no. 8, pp. 57-69, 2005.

[37] G. Welch and G. Bishop, "An introduction to the Kalman filter," in *SIGGRAPH, Course*, Chapel Hill, 2001.

[38] R. E. Kalman and R. S. Bucy, "New results in linear filtering and prediction theory," *Journal of Basic Engineering,* vol. 83, no. 1, pp. 95-108, 1961.

[39] S. Thrun, W. Burgard and F. Dieter, Probabilistic robotics, London: The MIT Press, 2005.

[40] S. Godha and M. E. Cannon, "Integration of DGPS with a low cost MEMS-based inertial measurement unit (IMU) for land vehicle navigation application," in *18th International Technical Meeting of the Satellite Division of the Institute of Navigation (ION GNSS05)*, Long Beach, 2005.

[41] J. Wendel, O. Meister, C. Schlaile and G. F. Trommer, "An integrated GPS/MEMS-IMU navigation system for an autonomous helicopter," *Aerospace Science and Technology,* vol. 10, no. 6, pp. 527 - 533, 2006.

[42] C. Acar and A. Shkel, MEMS vibratory gyroscopes: structural approaches to improve robustness, Springer Science & Business Media, 2008.

[43] H. G. Wang and T. C. Williams, "Strategic inertial navigation systems - high-accuracy inertially stabilized platforms for hostile environments," *IEEE Control Systems,* vol. 28, no. 1, pp. 65-85, 2008.

[44] I. Skog and P. Händel, "Calibration of a MEMS inertial measurement unit," in *XVII IMEKO World Congress*, Rio de Janeiro, 2006.

[45] Z. F. Syed, P. Aggarwal, C. Goodall, X. Niu and N. El-Sheimy, "A new multi-position calibration method for MEMS inertial navigation systems," *Measurement Science and Technology,* vol. 18, no. 7, p. 1897, 2007.

[46] J. Lötters, J. Schipper, P. H. Veltink, W. Olthuis and P. Bergveld, "Procedure for in-use calibration of triaxial accelerometers in medical applications," *Sensors and Actuators A: Physical,* vol. 68, no. 1-3, pp. 221-228, 1998.

[47] W. T. Fong, S. K. Ong and A. Y. C. Nee, "Methods for in-field user calibration of an inertial measurement unit without external equipment," *Measurement Science and technology,* vol. 19, no. 8, p. 085202, 2008.

[48] G. Casinovi, W. K. Sung, M. Dalal, A. N. Shirazi and F. Ayazi, "Electrostatic self-calibration of vibratory gyroscopes," in *2012 IEEE 25th International Conference on Micro Electro Mechanical Systems (MEMS)*, Paris, 2012.

[49] E. E. Aktakka, J. K. Woo, D. Egert, R. Gordenker and K. Najafi, "A micro vibratory stage

for on chip physical stimulation and calibration of MEMS gyroscopes," in *2014 International Symposium on Inertial Sensors and Systems (ISISS)*, Laguna Beach, CA, 2014.

[50] S. Nadig, V. Pinrod, S. Ardanuç and A. Lal, "In-run scale factor and drift calibration of MEMS gyroscopes with rejection of acceleration sensitivities," in *IEEE International Symposium on Inertial Sensors and Systems*, Laguna Beach, 2016.

[51] Y. Chen, E. E. Aktakka, J.-K. Woo and K. Oldham, "Threshold sensing signal construction from a capacitive sensor for MEMS gyroscope calibration," in *IEEE International Conference on Advanced Intelligent Mechatronics (AIM)*, Banff, 2016.

[52] J.-K. Woo, C. Boyd, J. Cho and K. Najafi, "Ultra-Low noise transimpedance amplifier for high performance MEMS resonant gyroscopes," in *Transducers*, Kaohsiung, 2017.

[53] InvenSense, "MPU-6500 Product Specification Revision 1.0," 18 09 2013. [Online]. Available: https://store.invensense.com/datasheets/invensense/MPU_6500_Rev1.0.pdf. [Accessed 18 04 2017].

[54] D. J. Ewins, Modal testing: theory and practice, Research Studies Press LTD. and John Wiley & Sons INC., 1984, p. 158.

[55] A. Trusov, I. Prikhodko, D. Rozelle, A. Meyer and A. Shkel, "1 PPM precision self-calibration of scale factor in MEMS Coriolis vibratory gyroscopes," in *The 17th International Conference on Solid-State Sensors, Actuators and Microsystems*, Barcelona, 2013.

[56] A. Norouzpour-Shirazi and F. Ayazi, "A Dual-Mode Actuation and Sensing Scheme for In-Run Calibration of Bias and Scale Factor Errors in Axisymmetric Resonant Gyroscopes," *IEEE Sensors Journal,* vol. 18, no. 5, pp. 1993 - 2005, 2017.

[57] Y. Li, X. Niu, Q. Zhang, H. Zhang and C. Shi, "An in situ hand calibration method using a pseudo-observation scheme for low-end inertial measurement units," *Measurement Science and Technology,* vol. 23, no. 10, 2012.

[58] S. Nadig and A. Lal, "In-situ calibration of MEMS inertial sensors for long-term reliability," in *2018 IEEE International Reliability Physics Symposium (IRPS)*, Burlingame, 2018.

[59] Y. Chen, E. E. Aktakka, J.-K. Woo, K. Najafi and K. R. Oldham, "On-chip capacitive sensing and tilting motion estimation of a micro-stage for in situ MEMS gyroscope calibration," *Mechatronics,* 2018.

[60] Y. Chen, E. E. Aktakka, J.-K. Woo, K. Najafi and K. R. Oldham, "Error Contributions During MEMS Gyroscope Calibration by Chip-Scale Micro-Stage with Capacitive Motion Sensor," in *IEEE/ASME International Conference on Advanced Intelligent Mechatronics*, Auckland, 2018.

[61] P. R. Scheeper, A. v. d. Donk, W. Olthuis and P. Bergveld, "A review of silicon microphones," *Sensors and actuators A: Physical,* vol. 44, no. 1, pp. 1 - 11, 1994.

[62] G. Stemme, "Resonant silicon sensors," *Journal of Micromechanics and Microengineering,* vol. 1, no. 2, p. 113, 1991.

[63] H. Schenk, P. Dürr, T. Haase, D. Kunze, U. Sobe, H. Lakner and H. Kück, "Large deflection micromechanical scanning mirrors for linear scans and pattern generation," *IEEE Journal of Selected Topics in Quantum Electronics,* vol. 6, no. 5, pp. 715 - 722,

2000.

[64] H. Li, X. Duan, Z. Qiu, Q. Zhou, K. Kurabayashi, K. R. Oldham and T. D. Wang, "Integrated monolithic 3D MEMS scanner for switchable real time vertical/horizontal cross-sectional imaging," *Optics Express,* vol. 24, no. 3, pp. 2145-2155, 2016.

[65] W. Shahid, Z. Qiu, X. Duan, L. Haijun, T. D. Wang and R. K. Oldham, "Modeling and Simulation of a Parametrically Resonant Micromirror With Duty-Cycled Excitation," *Journal of Microelectromechanical Systems,* pp. 1440 - 1453, 2014.

[66] M. Basu, "Gaussian-based edge-detection methods-a survey," *IEEE Transactions on Systems, Man, and Cybernetics, Part C (Applications and Reviews),* vol. 32, no. 3, pp. 252 - 260, 2002.

[67] J. Canny, "A computational approach to edge detection," *IEEE Transactions on pattern analysis and machine intelligence 6,* pp. 679 - 698, 1986.

[68] M. R. K. J. T. S. Richard Schroedter, "Flatness-based open-loop and closed-loop control for electrostatic quasi-static microscanners using jerk-limited trajectory design," *Mechatronics,* 2017.

[69] H. W. Lilliefors, "On the Kolmogorov-Smirnov Test for Normality with Mean and Variance Unknown," *Journal of the American statistical Association,* vol. 62, no. 318, pp. 399-402, 1967.

[70] Z. Qiu and W. Piyawattanametha, "MEMS-Based Medical Endomicroscopes," *IEEE Journal of Selected Topics in Quantum Electronics,* vol. 21, no. 4, 2015.

[71] X. Duan, H. Li, J. Zhou, Q. Zhou, O. R. Kenn and T. D. Wang, "Visualizing epithelial expression of EGFR in vivo with distal scanning side-viewing confocal endomicroscope," *Scientific reports,* p. 37315, 2016.

[72] X. Duan, H. Li, Z. Qiu, B. P. Joshi, A. Pant, A. Smith, K. Kurabayashi, K. R. Oldham and T. D. Wang, "MEMS-based multiphoton endomicroscope for repetitive imaging of mouse colon," *Biomedical optics express,* vol. 6, no. 8, pp. 3074-3083, 2015.

[73] O. Trepte and A. Liljeborg, "Computer control for a galvanometer scanner in a confocal scanning laser microscope," *Optical Engineering,* vol. 33, no. 11, pp. 3774-3781, 1994.

[74] U. Hofmann, J. Janes and H.-J. Quenzer, "High-Q MEMS resonators for laser beam scanning displays," *Micromachines,* vol. 3, no. 2, pp. 509 - 528, 2012.

[75] C. Drabe, D. Kallweit, A. Dreyhaupt, J. Grahmann, H. Schenk and W. Davis, "Bi-resonant scanning mirror with piezoresistive position sensor for WVGA laser projection systems," in *SPIE MOEMS-MEMS*, San Francisco, 2012.

[76] R. Schroedter, M. Roth, . K. Janschek and T. Sandner, "Flatness-based open-loop and closed-loop control for electrostatic quasi-static microscanners using jerk-limited trajectory design," *Mechatronics,* 2017.

[77] A. C.-L. Hung, H. Y.-H. Lai, T.-W. Lin, S.-G. Fu and M. S.-C. Lu, "An electrostatically driven 2D micro-scanning mirror with capacitivesensing for projection display," *Sensors and Actuators A: Physical,* vol. 222, no. 1, pp. 122-129, 2015.

[78] H. Lin, T.-W. Lin, A. C.-L. Hung and M. S.-C. Lu, "A bi-axial capacitive scanning mirror with closed-loop control," in *IEEE Micro Electro Mechanical Systems (MEMS)*, Belfast, 2018.

[79] Y. Chen, H. Li, Z. Qiu, T. D. Wang and K. R. Oldham, "Improved Extended Kalman

Filter Estimation using Threshold Signal Detection with a MEMS Electrostatic Micro-Scanner," *IEEE Transactions on Industrial Electronics,* 2018.

[80] C. Ataman and U. Hakan, "Modeling and characterization of comb-actuated resonant microscanners," *Journal of Micromechanics and Microengineering,* vol. 16, no. 1, 2005.

[81] L. E. Frenzel, Principles of electronic communication systems, New York: McGraw-Hill Education, 2007.

[82] E. A. Wan and R. v. d. Merwe, "The unscented Kalman filter for nonlinear estimation," in *Adaptive Systems for Signal Processing, Communications, and Control Symposium*, Lake Louise, 2000.